LIBRARY OF THE UNIVERSITY OF ADELAIDE
9-9-66

ATMOSPHERIC ABSORPTION OF SOLAR ULTRA-VIOLET RADIATION

by

Peter Mitchell B.Sc.(Hons.)
Department of Physics

A thesis
presented for the degree of
Doctor of Philosophy
in the
University of Adelaide
February, 1966

CONTENTS

Summary (v)

Preface (viii)

Acknowledgements (ix)

Chapter 1. The Solar Spectrum between 1000 and 1700Å

1.1 A review of Previous Measurements of the Solar Ultra-Violet Spectrum. 1

1.1.1 Dispersive Measurements. 1

1.1.2 Non-dispersive Measurements. 11

1.2 The Nature of the Solar Spectrum between 1000 and 1700Å. 14

Chapter 2. The Absorption of Solar Ultra-Violet Radiation in the Earth's Atmosphere.

2.1 The Absorption Cross-sections of the Principal Atmospheric Constituents. 18

2.2 Absorption Processes taking place in the Atmosphere. 23

2.3 The Determination of Atmospheric Composition from Ultra-Violet Absorption Measurements. 25

2.3.1 The Absorption Law. 25

2.3.2 Atmospheric Absorption. 27

2.3.3 Absorption of Solar Radiation in the Range 1000 to 1700Å. 31

2.3.4 The Shape of an Atmospheric Absorption Curve. 34

2.4 The Determination of Temperature Profiles from Density Profiles. 37

2.5 Previous Measurements of Molecular Oxygen Densities. 41

Chapter 3. Ion Chambers for the Detection of Vacuum Ultra-Violet Radiation.

3.1 Introduction. 51

3.2 Construction of the Ion Chambers. 55

3.3 Filling the Ion Chambers. 57

D133919

	3.3.1 The Vacuum System.	57
	3.3.2 Filling Procedure.	59
	3.3.3 Filling Gases.	60
3.4	Monochromators and Light Sources used in testing the Ion Chambers.	61
	3.4.1 Monochromators.	61
	3.4.2 Light Sources.	62
3.5	The Portable Light Source.	64
3.6	Determination of the Spectral Response and Absolute Efficiency of the Ion Chambers.	65
	3.6.1 Introduction.	66
	3.6.2 Spectral Response.	69
	3.6.3 Absolute Efficiency.	71
3.7	Spectral Response Curves.	74
3.8	Angular Response and Effective Aperture of the Ion Chambers.	77
	3.8.1 Angular Response.	77
	3.8.2 Effective Aperture.	78
3.9	Temperature Effects.	79
3.10	Gas Gain.	83
3.11	Effect of Intense Ultra-Violet Radiation on the Ion Chambers.	85
3.12	Conclusions.	88
Chapter 4.	Design of the Rocket Experiment to Measure Solar Lyman-α Radiation.	
4.1	The HAD Rocket.	91
4.2	Design of the Rocket Head.	92
4.3	Electrical Circuitry.	94
4.4	Aspect Sensing.	95
	4.4.1 The Different Methods of obtaining Solar Aspect.	95
	4.4.2 The Double Amplitude-Modulation Sensor.	101
	4.4.3 Conclusion.	104

Chapter 5. The Results of Two Experiments to Measure Solar Lyman-α Radiation.

Introduction. 106

(A) HAD 301

5.1 Rocket Performance. 106

5.2 Results from HAD 301 107

(B) HAD 304

5.3 Rocket Performance. 110

5.4 Analysis of the Height Data. 112

5.5 Analysis of the Aspect Data. 116

5.6 The Lyman-α Flux Data. 118

5.7 Oxygen Densities. 120

5.8 Absorption of Lyman-α by Gases other than Oxygen. 121

5.9 Temperature Profile. 127

5.10 Discussion. 128

5.10.1 Oxygen Densities. 128

5.10.2 Temperatures. 130

5.10.3 Lyman-α Intensities. 130

Chapter 6. Statistics of Electron Multiplication in Proportional Counters.

6.1 Introduction. 132

6.2 Notation. 133

6.3 Previous Investigations of Avalanche Statistics. 134

6.4 Apparatus. 139

6.5 The Measurements. 142

6.6 Analysis of the Pulse Spectra. 144

6.6.1 Introduction. 144

6.6.2 Mathematical Method. 145

6.6.3 The Logarithmic Derivatives. 147

6.7 Discussion. 147

6.8 Conclusion. 148

Chapter 7. Absorption Coefficients of Some Filling Gases.

7.1 Introduction. 154
7.2 Method. 154
7.3 Results. 156
7.4 Discussion. 157

Chapter 8. Conclusion. 158

Appendix - Publications. 161

References. 162

SUMMARY

The aim of the work described in this thesis was to carry out measurements of the absorption of solar vacuum ultra-violet radiation in the earth's atmosphere and to use these measurements to derive atmospheric molecular oxygen densities. Measurements had previously been made by several workers using both dispersive instruments, which require a rocket with a pointing control, and non-dispersive instruments, which can be used with unstabilized rockets, but no molecular oxygen densities derived in this way had been reported for the Southern Hemisphere. The opportunity of using the unstabilized HAD and Long Tom rockets fired from Woomera made it possible to plan a number of flights using simple ion chambers sensitive to various wavelength bands in the range 1000 to 1650Å. These provide a relatively simple means of measuring accurately the absolute fluxes and give absorption profiles with better height resolution than is obtainable using dispersive instruments.

Two HAD rockets were successfully fired carrying ion chambers sensitive to Lyman-α radiation. Oxygen densities were derived for three altitudes from the results of the first flight and at 1 km intervals from the results of the second. The two sets of values are in good agreement and lie closer to those of the U.S. Standard Atmosphere than

those obtained by Northern Hemisphere workers. However it is suggested that the densities deviate significantly below those of the U.S. Standard Atmosphere at heights below 80 km. Temperature profiles derived from these oxygen densities indicate temperatures 5 to 10°C above those of the U.S. Standard Atmosphere. The measurements of the intensity of the solar Lyman-α line, combined with those of other workers, imply that the variation in intensity during one sunspot cycle is not more than ±10%. A Long Tom rocket, which has a maximum altitude of 150 km, was instrumented with a number of different ion chambers covering the range 1000-1650Å but this experiment was unsuccessful owing to a failure in the telemetry equipment.

An investigation has been made of a number of characteristics of the vacuum ultra-violet ion chambers with the aim of improving their reliability as rocket-borne detectors. Five different windows and twelve filling gases have been used in various combinations to produce fourteen chambers sensitive to different wavelength bands in the range 1000-1650Å. The spectral response and absolute efficiency of each chamber has been measured. The effect of temperature changes in the range 0 to 100°C on the spectral responses has been determined, it being found that both the lower and upper limits of the spectral response are moved to higher wavelengths as the temperature

is raised. It has also been shown that carbon disulphide is unsuitable as a filling for ion chambers used in the detection of solar radiation since the decomposition of the carbon disulphide by the ultra-violet radiation leads to a serious reduction in the transmission of the window. The absorption coefficients of some of the filling gases, which were not previously known, have been measured.

As an adjunct to the work on ion chambers an investigation has been made of the statistical properties of the gas multiplication which takes place when these detectors are used as proportional counters. Previous measurements on the statistical fluctuation in the size of avalanches initiated by a single primary electron had been made with only a few filling gases. Pulse spectra were recorded for six different fillings, at a number of counter voltages, and over a wide range of pulse heights. The shapes of the pulse spectra can be related quite satisfactorily to various theoretical distributions but the presence of secondary avalanches in almost all cases indicates that the relative variance of the distributions is greater than previously assumed.

PREFACE

This thesis contains no material which has been accepted for the award of any other degree or diploma in any University. To the best of the author's knowledge and belief it contains no material previously published or written by another person, except when due reference is made in the text.

ACKNOWLEDGEMENTS

The rocket experiments described in this thesis were carried out in co-operation with the Flight Projects Group, Weapons Research Establishment, led by Mr. B. Rofe to whom the author would like to express his thanks for making these experiments possible.

The author would also like to thank Dr. E.L. Murray who carried out most of the work involved in designing the electrical circuitry for the rockets.

Finally the author would like to thank his supervisor Professor J.H. Carver most sincerely for his guidance throughout the course of this work.

This investigation was carried out while the author was holding a Senior Studentship granted by the Commonwealth Scientific and Industrial Research Organization.

LIBRARY OF THE UNIVERSITY OF ADELAIDE

Chapter 1. The Solar Spectrum Between 1000 and 1700Å

1.1 A Review of Previous Measurements of the Solar Ultra-Violet Spectrum

1.1.1 Dispersive Measurements.

Prior to 1946 the nature of the solar spectrum at wavelengths less than 2900Å was unknown owing to the fact that the earth's atmosphere absorbs strongly in this region. The cut-off at 2900Å observed from the ground is due to ozone which, although present in only a very small quantity (the total ozone content of the atmosphere is equivalent to a layer about 2 to 3mm thick at S.T.P.), has such a high absorption coefficient in the region 2200 to 2900Å that it effectively prevents any of this radiation from the sun reaching the ground. Balloons do not attain sufficient altitude to rise above the ozone, which reaches its maximum concentration at about 25 km, and so the exploration of this region of the solar spectrum had to await the advent of rockets capable of rising to heights of 75 km or more. The first to be used were the V2 rockets captured from the Germans during the war and fired in America during the years 1946 to 1949. The history of these and subsequent investigations up to 1963 has been reviewed by Tousey (1963) and Pagel (1963). The latter paper contains a list of the most notable flights most of which have been made from White Sands in America.

The first spectra taken from the V2 rocket (Baum et al. 1946) showed quite clearly the effect of the atmospheric ozone. A series of thirty-five spectra was taken at heights up to 88 km, and as the rocket climbed the limit of the observed spectrum moved from 2900Å down to 2100Å. The instrument used was a normal incidence grating spectrograph with photographic recording of the spectra, the film being recovered after the flight. The spectra were not of good resolution and showed only a continuation of the visible continuum together with the very strong absorption doublet of Mg II at 2803Å and 2796Å. These are the resonance lines of Mg II and correspond to the H and K absorption lines of Ca II observed in the visible. Another flight was made in 1947 using the V2 (Hopfield and Clearman 1948), and spectra were obtained showing that the Fraunhofer absorption lines observed in the visible continued below 2900Å. About thirty absorption lines were identified in the range 2300 to 2900Å.

Extension of the observations to shorter wavelengths was not possible, however, using the technique of these flights in which the rocket was unstabilized and the spectrograph had to have a wide field of view. This is a result of the rapid drop in intensity of the solar spectrum at wavelengths less than 2100Å. To overcome this difficulty a pointing control was developed which could keep an instrument pointed towards the sun irrespective of the motion of the rest of

the rocket. It was built into the Aerobee, a rocket developed for high altitude research and used almost exclusively for solar spectrum observations at high altitudes from 1952 onwards.

In 1952 Rense (1953), using the pointing control and a grazing incidence spectrograph, obtained the first image of Lyman-α, the resonance line of atomic hydrogen, and showed that it was an emission line in contrast to the Balmer lines observed in the visible and near ultra-violet which appear as absorption lines. The estimated intensity of this line was 0.5 erg cm^{-2} sec^{-1}.

Better images of the Lyman-α line were obtained in 1954 by Johnson et al. (1954) using a double spectrograph which was flown a number of times and has been described by Johnson et al. (1958). One spectrograph covered the range 500 to 2500Å, the sun being imaged onto the slit by a concave mirror, while the other covered the range 1500 to 3500Å and employed a lithium fluoride lens to image the sun onto the slit. The altitude reached on that flight was 104 km. In 1955 aflight using the same instrument reached an altitude of 115 km and the spectra showed for the first time emission lines other than Lyman-α (Johnson et al. 1958). About forty lines were identified between 1670Å and the C III line at 977Å. The 500 to 2500Å spectrograph was designed so that the images of the spectral lines were

stigmatic i.e. the intensity distribution along a line corresponded to the intensity distribution along a diameter of the solar disc at that wavelength. Because of this, measurements could be made of the limb brightening or darkening for various wavelengths. The sudden drop in intensity at 2085Å was also recorded on this flight. Intensities of 0.6 and 1.6 erg cm^{-2} sec^{-1} for the Lyman-α line were derived from the 1954 and 1955 flights respectively.

From a flight made in 1957 using a grazing incidence spectrograph Aboud et al. (1959) derived intensities for a number of the emission lines, including a value of 3.4 erg cm^{-2} sec^{-1} for Lyman-α. An improved version of this instrument was flown in 1958 and 1959 by Violett and Rense (1959) who detected for the first time the resonance lines of HeI and HeII at 584 and 304Å respectively. Use of the grazing incidence mounting for the grating enables shorter wavelengths to be detected as the reflectivity of the grating is higher at grazing incidence, and lines down to 84Å were observed.

The best spectra obtained with a single dispersion instrument were taken in 1959 by Purcell et al. (1960) using the normal incidence instrument already mentioned (Johnson et al. 1958), but with a special coating on the grating to reduce the effect of stray light. The spectra were also taken at a higher altitude than previously (198 km).

Fifty-five emission lines above 584Å were identified. Further improvement in the spectra was obtained by the use of a double dispersion instrument first flown in 1960 by Detwiler et al. (1961a). The first grating dispersed the solar radiation along the slit from which the radiation passed to the second grating. In this way the level of stray light inside the spectrograph was very much reduced. The first grating was distorted to make the final images stigmatic as in the single dispersion instrument. From the spectra obtained during this flight an intensity distribution for the region 900 to 1550Å was derived (see Figure 2.) which gave the absolute intensities of all the observed lines and the continuum (Detwiler et al. 1961b). An ion chamber flown together with the spectrograph was used to determine the absolute level of the fluxes.

The most recent photographic spectra covering the range 1000 to 1600Å were obtained in 1962 by Tousey et al. (1964) using two double dispersion instruments covering the ranges 1200 to 2000Å and 800 to 1250Å with resolutions of 0.2Å and 0.1Å respectively. Nearly complete elimination of stray light enabled the continuum to be traced down to a wavelength of about 950Å. Intensity curves from these spectra have not yet been published.

A completely different technique for the measurement of the solar spectrum has been used by Hinteregger and his

colleagues. They have constructed a grazing incidence monochromator in which the spectrum is scanned by a slit in a moving belt and detected by a windowless, magnetically focussed, strip photomultiplier. The output pulses from the photomultiplier are telemetered to the ground so that the spectra are recorded during the flight as the monochromator repeatedly scans through the desired spectral range. A detailed description of this instrument, which was first successfully flown in 1959, has been given by Hinteregger (1961a). The property of the photomultiplier which makes it particularly suitable for this application is the negligible sensitivity of the photocathode to radiation of wavelength longer than about 1500Å. This means that it is insensitive to the long wavelength stray light which is always a problem in spectrographs used for detecting the sun's ultra-violet spectrum since 99.999% of the sun's energy is radiated at wavelengths longer than 1500Å. The scanning monochromator is also very suitable for studying absorption in the earth's atmosphere of radiation of a particular wavelength, about twenty scans being made during a flight.

Two flights during 1960 with this instrument (Hinteregger 1961b, Hinteregger 1961c) gave spectra covering the range 300 to 1300Å. From the results of the second flight values were obtained for the absolute fluxes,

extrapolated to the top of the atmosphere, of all the important lines and the continuum in this range. Estimates were also made of the height h* at which the solar flux had been attenuated to $\frac{1}{e}$ of its value above the atmosphere for the various wavelengths. Absorption rate densities (the number of photons absorbed per unit volume per unit time) were given as a function of height for several strong lines with wavelengths ranging from 304Å to 1207Å. The values for the intensity of Lyman-α derived from the results of these two flights were 6.0 and 3.3 erg cm^{-2} sec^{-1} respectively, the latter value being obtained from an ion chamber flown with the spectrograph.

From a flight in 1961 with the scanning monochromator Hall et al. (1963a) derived further values for absolute fluxes in the range 300 to 1300Å, and photon absorption rate densities for twenty strong lines between 283Å and 1206Å. These and later absorption measurements have been used together with a knowledge of the absorption coefficients of the principal atmospheric constituents to obtain the densities of these constituents above 100 km (see §2.5). Further analysis involving the photoionization efficiencies has enabled Hinteregger and Watanabe (1962) to give a fairly detailed account of the processes leading to the formation of the E and F regions of the ionosphere. These calculations have been revised (Hinteregger et al. 1965) using the results of

several later flights. This paper also contains the most recently compiled list of absolute fluxes. Values in the range 55 to 1300Å are based on the scanning monochromator measurements and include the fluxes for all the important lines. Above 1300Å the values are based on the photographic measurements and are given only as the integrated fluxes in 50Å intervals. The maximum errors in the data are estimated to be 30%.

Photographic spectra covering the range 1000 to 3000Å have also been obtained by workers at the Culham Laboratory of the U.K.A.E.A. using a normal incidence spectrograph and the recently developed pointing control for the Skylark rocket (Black et al. 1965, Burton and Wilson 1965). This pointing control has the advantage over the one used in the Aerobee rocket that it is stabilised along three axes, whereas the Aerobee pointing control is stabilized along two axes only and allows the spectrograph to rotate about a line joining the rocket to the sun. Using this control it has been possible to attain sufficient pointing accuracy to direct the spectrograph at the limb of the sun and photograph the spectrum of the solar chromosphere and corona, rather than photographing the photospheric spectrum obtained when the spectrograph is pointed directly at the sun.

The difficulties associated with absolute flux determination from photographic measurements have been

discussed by Johnson et al. (1958), Detwiler et al. (1961b) and Rense (1961). The sensitivity of the film and the instrument transmission constant must be measured as functions of wavelength. Alternatively the two quantities can be measured simultaneously by placing the whole instrument in a vacuum chamber and exposing it to an absolutely calibrated beam of monochromatic radiation at various wavelengths. Even this does not provide an accurate method of determining the absolute level of the spectrum since the angular divergence of the beam from the laboratory source may not be the same as that from the sun. One of the following additional methods has usually been used.

(a) Spectra which extend above 3000Å can be compared with absolute measurements made from the ground. This method is useful down to about 1800Å but not for shorter wavelengths because the very great difference in intensities between the 3000 to 4000Å region and the region below 1800Å is difficult to accommodate in one exposure.

(b) Measurements made with absolutely calibrated non-dispersive detectors can be used.

The latter method was first employed by Byram et al. (1958) who used measurements made with detectors sensitive to the ranges 1050 to 1350Å and 1225 to 1350Å (see p.13) to correct the absolute fluxes derived from the spectrographic measurements of 1955 by Johnson et al. (1958). It was

pointed out by Byram et al. that while measurements of the total flux in the 1050 to 1350Å range may be used to determine the absolute Lyman-α flux, the 1225 to 1350Å range is better for determining the level of the other lines since the Lyman-α line is usually overexposed on photographic spectra and comparison with other lines is difficult. Ion chambers sensitive to Lyman-α have generally been included in recent rocket flights of photographic spectrographs covering this line (Detwiler et al. 1961b).

Ion chambers have also been included with some of the photoelectric scanning monochromators (Hinteregger 1961c), but recently reliance has been placed on the laboratory calibration of these instruments before flight which is easier than in the case of the photographic instruments. The calibration procedure has been described by Hinteregger (1961a). The monochromators collect radiation from the whole disc of the sun, whereas the photographic instruments, being generally stigmatic, give a spectral line the intensity of which varies along the line corresponding to active regions. This mades it easier to measure the integrated intensity from the whole disc with the monochromators than with the spectrographs.

In assessing the relative merits of the two methods it could perhaps be said that the photographic method provides better resolution and sensitivity, making it more useful for

obtaining data of astrophysical interest (the nature of the solar atmosphere etc.). The photoelectric method, on the other hand, provides better absolute measurements in the region below 1300Å where it is applicable and is also much more suitable for studying the absorption of solar radiation in the earth's atmosphere. Thus it gives better data for use in the investigation of processes taking place in the upper atmosphere (the formation of the ionosphere, the dissociation of oxygen etc.).

1.1.2 Non-dispersive Measurements.

After the first spectrographic measurements, carried out using the V2 rockets, had succeeded in revealing the solar spectrum down to a wavelength of 2100Å attempts were made to extend the measurements to the much weaker short wavelength ultra-violet radiation using non-dispersive techniques. The first method involved the use of the thermoluminescent phosphor $CaSO_4$:Mn. This phosphor is activated when exposed to radiation of wavelength less than 1340Å and phosphoresces when subsequently heated. By placing windows of lithium fluoride and calcium fluoride in front of it the response can be limited to the ranges 1050 to 1340Å and 1220 to 1340Å respectively. These detectors were flown a number of times during the period 1948 to 1950 in V2 rockets (Tousey et al. 1951). As detectors for measuring absolute fluxes they were not very successful, indicating an intensity for the Lyman-α

line of 0.4 erg cm^{-2} sec^{-1}, but they did show that radiation in the ranges 1050 to 1340Å and 1220 to 1340Å was absorbed in the 80 to 90 km and 90 to 125 km regions respectively.

In 1949 Friedman et al. (1951) using a V2 rocket flew three different Geiger counters sensitive to ultra-violet light. The one sensitive to Lyman-α radiation had a lithium fluoride window and a filling of chlorine and neon. It responded over the range 1100 to 1350Å. Interpretation of the results was difficult owing to saturation of the counters, but the Lyman-α intensity was estimated to be in the range 1 to 10 erg cm^{-2} sec^{-1}. Similar counters were flown in several Aerobee flights during 1952 (Byram et al. 1953), yielding values of 0.15 and 0.1 erg cm^{-2} sec^{-1} for the Lyman-α flux. Like the thermoluminescent phosphor these counters were unsuitable for absolute flux determination (see §3.1). However, by analysis of the variation with height of the intensity of the 1100 to 1350Å radiation Byram et al. were able to show that it was absorbed in the atmosphere like monochromatic radiation and concluded that at least 90% of the radiation in this range was Lyman-α.

The ion chambers which have since been used almost exclusively for non-dispersive measurements were first flown in 1955 by Byram et al. (1956), three years after Lyman-α had first been detected spectrographically. A lithium fluoride window and nitric oxide filling were used

for these chambers which responded to the range 1050 to 1350Å. Values for the Lyman-α flux obtained with them were all higher than previous measurements, both spectrographic and non-dispersive, and lay in the range 4.0 to 9.2 erg cm^{-2} sec^{-1}. However these higher values were accepted in preference to the previous ones because, as pointed out by Byram et al. (1958), the sensitivity of the chambers themselves can only decrease as a result of ageing between calibration and flight, so that provided there are no errors from other sources the values obtained using ion chambers must be minimum values. In 1956 an ion chamber was flown during a solar flare by Chubb et al. (1957) in order to detect any change in the Lyman-α flux during the flare, but from the results they concluded that the flux did not vary to any measurable extent. This and other measurements during 1957 gave values for the flux close to 6.0 erg cm^{-2} sec^{-1}. An ion chamber with a calcium fluoride window and nitric oxide filling, sensitive to the range 1220 to 1350Å, was used together with the 1050 to 1350Å chamber by Byram et al. (1958) in two flights made in 1957 and 1958. They used the results to determine the absolute levels of some previous spectrographic measurements (see p. 9). The intensity of the Lyman-α line has also been measured by workers using a lithium fluoride - nitric oxide ion chamber flown in a Skylark rocket at Woomera. The result

obtained (Willmore 1961) was $(3.0 \pm 2.6 - 1.6)$ erg cm^{-2} sec^{-1}, in substantial agreement with earlier ion chamber results. More recently, Smith et al. (1965) have used similar ion chambers to obtain a value of 2.4 ± 0.3 erg cm^{-2} sec^{-1} for the Lyman-α flux.

A lithium fluoride - nitric oxide ion chamber was included in the Solar Radiation I satellite launched in 1960, with the aim of detecting variations in the Lyman-α flux during solar flares (Kreplin et al. 1962). The ion chamber failed after several months but the results obtained during this time agreed with those obtained by Chubb et al. (1957) in suggesting that during a flare there were no variations in the Lyman-α flux received at the earth large enough to cause significant changes in the upper atmosphere (e.g. D region ionization).

1.2 The nature of the Solar Spectrum between 1000 and 1700Å

In the visible region the solar spectrum consists of an emission continuum which follows closely that of a black body at about 6000°K, together with a very large number of absorption lines (the Fraunhofer lines). The spectrum in the ultra-violet and x-ray regions however is quite different as can be seen in Figure 1.

The nature of the solar ultra-violet spectrum as revealed by experiments using rockets has been described in

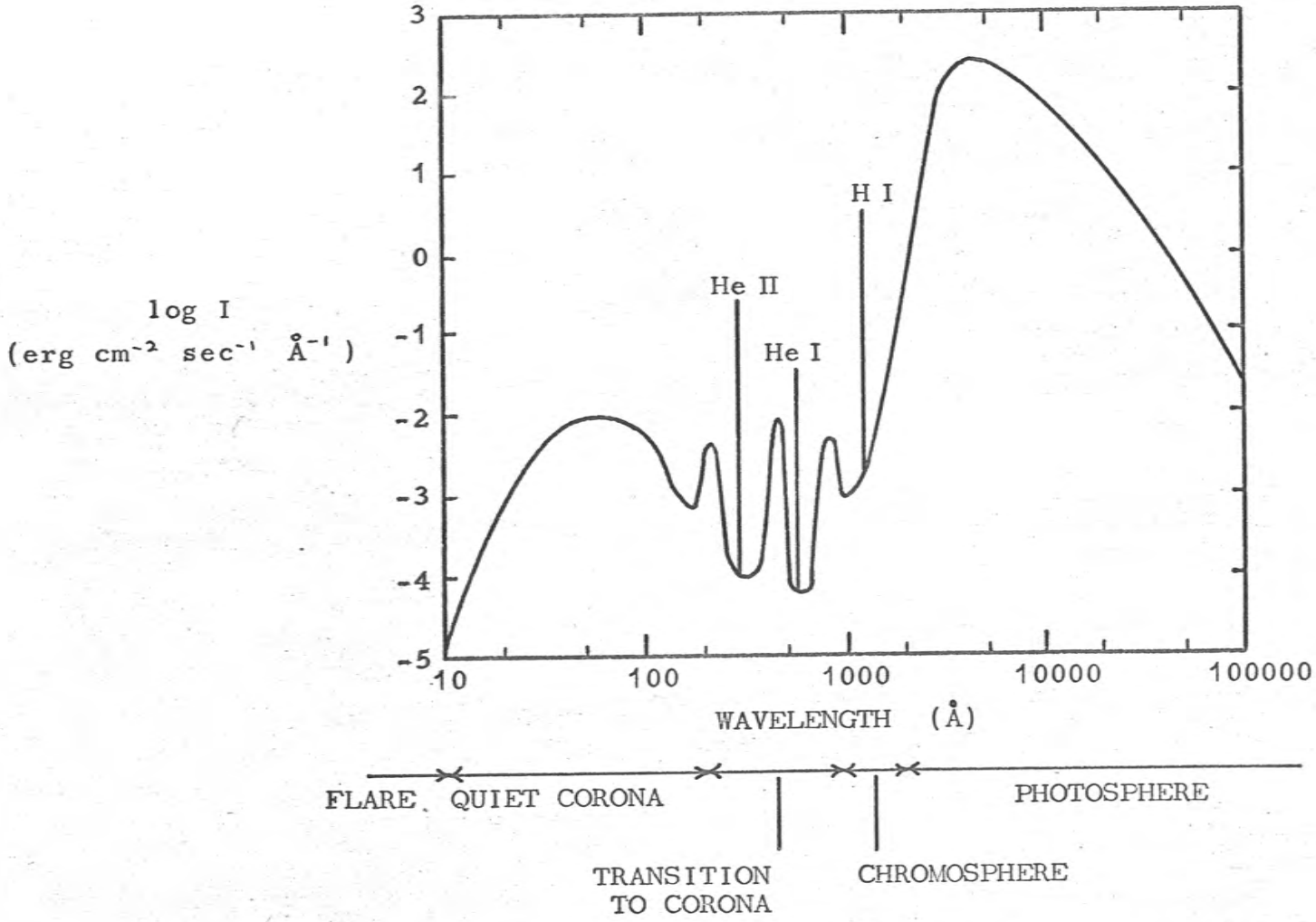

Figure 1. The solar spectrum from 10 to 100,000 Å (after de Jager (1964) and Allen (1963)). The regions where the various sections of the spectrum originate are indicated below the wavelength scale. The X-ray region of the spectrum ($\lambda<100$ Å) shows large variations in intensity; the spectrum shown is for quiet conditions at solar maximum.

detail by Tousey (1963) and Pagel (1963), while its interpretation in terms of the processes occurring in the layers of the sun where it originates has been discussed in these papers and also by Pottasch (1964), de Jager (1964) and Allen (1965). The emitting region of the solar atmosphere can be divided into three layers:

(a) The photosphere. This is the innermost region and is about 100 km thick. The temperature is 6000°K at the base, dropping to about 4000°K at the top.

(b) The chromosphere. This region is 12,000 km thick and has a temperature rising from 4000°K where it adjoins the photosphere to about 40,000°K where it meets the corona.

(c) The corona. This region of extremely low density extends for perhaps 10^6 km and has a temperature of about 10^6 °K.

The visible continuum originates in the photosphere and reflects its temperature of 6000°K. The Fraunhofer lines are produced at the base of the chromosphere where the temperature is lower. As the wavelength decreases, however, the opacity of the chromosphere increases and the observed radiation comes from higher and higher regions. This causes the radiation temperature $T_R(\lambda)$* to decrease as the

* The radiation temperature of the sun at a particular wavelength is the temperature of a black body which would emit as much radiation at that wavelength as the sun.

wavelength λ decreases, and the intensity of the solar continuum lies below that of a 6000°K black body in the ultra-violet region down to 100Å. T_R reaches a minimum of 4700°K at about 1400Å corresponding to a change in the origin of the continuum from the photosphere to the chromosphere. The Fraunhofer lines are not present at wavelengths less than 1550Å and are replaced by emission lines which commence at about 1900Å. These emission lines, including Lyman-α, originate in the high chromosphere. At wavelengths less than 1400Å T_R increases as the origin of the radiation moves up through the chromosphere and into the corona.

Figures 2 and 3 show the most recently published solar intensity curves for the range 1050 to 1550Å, derived from photographic and photoelectric measurements respectively. These spectra cover the wavelength region in which measurements can be made with the ion chambers described in Chapter 3, except for the section 1550 to 1650Å. The emission lines in this range are due to hydrogen, carbon, nitrogen, oxygen, silicon and sulphur atoms, in various stages of ionization. The predominance of the resonance line of atomic hydrogen, Lyman-α, is clearly shown. The photographic curve also shows the presence of the weak continuum.

The profile of Lyman-α was determined in 1959 by

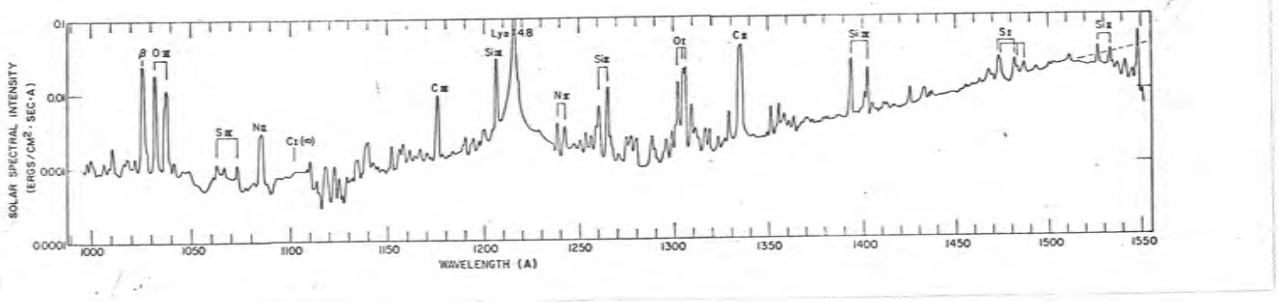

Figure 2. The solar spectrum in the vacuum ultra-violet region measured with a photographic spectrograph (from Detwiler et al. (1961b)).

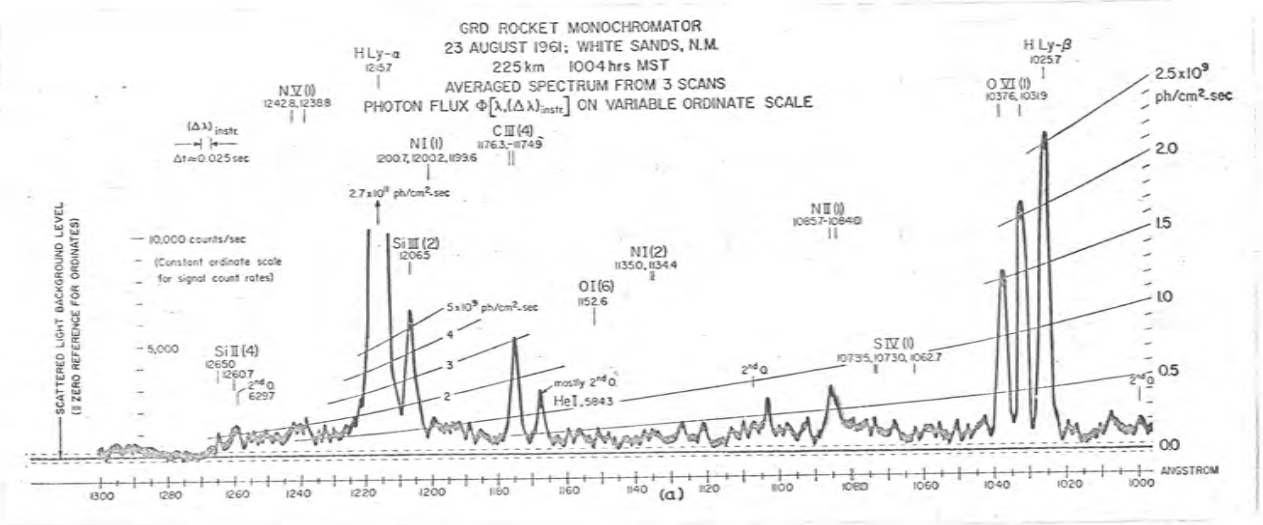

Figure 3. The solar spectrum in the vacuum ultra-violet region measured with a photoelectric monochromator (from Hall et al. (1963a)).

Purcell and Tousey (1960) who flew a grating spectrograph having a resolution of approximately 0.03Å. The line shape is shown in Figure 4. The emission line has a half-width of about 1Å and is self-reversed. Superimposed on this solar line is a very narrow (~ 0.03Å) absorption core due to atomic hydrogen between the sun and the earth.

Figure 4. The shape of the Lyman-α line as measured by Purcell and Tousey (1960) with a resolution of 0.03Å. A microdensitometer tracing is shown below the line.

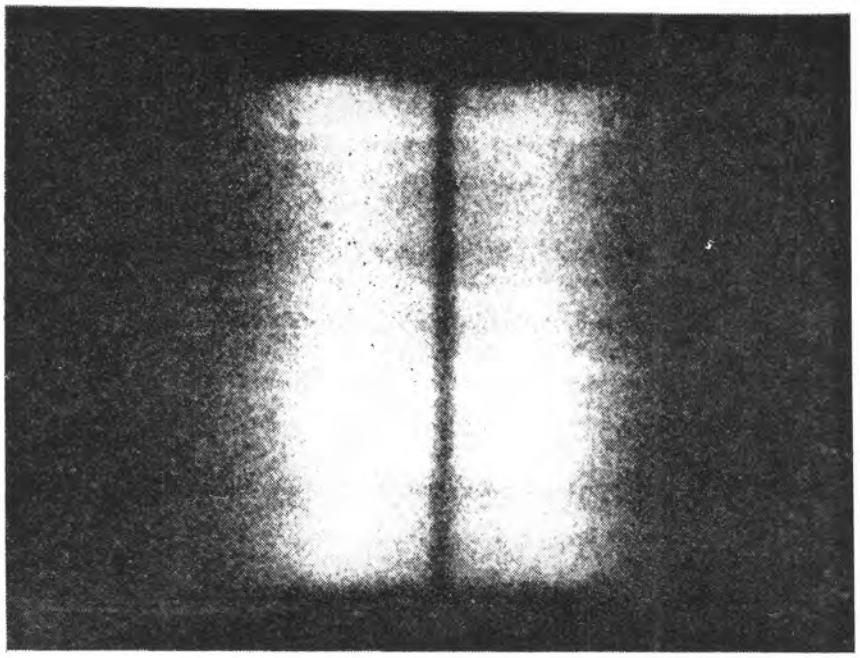

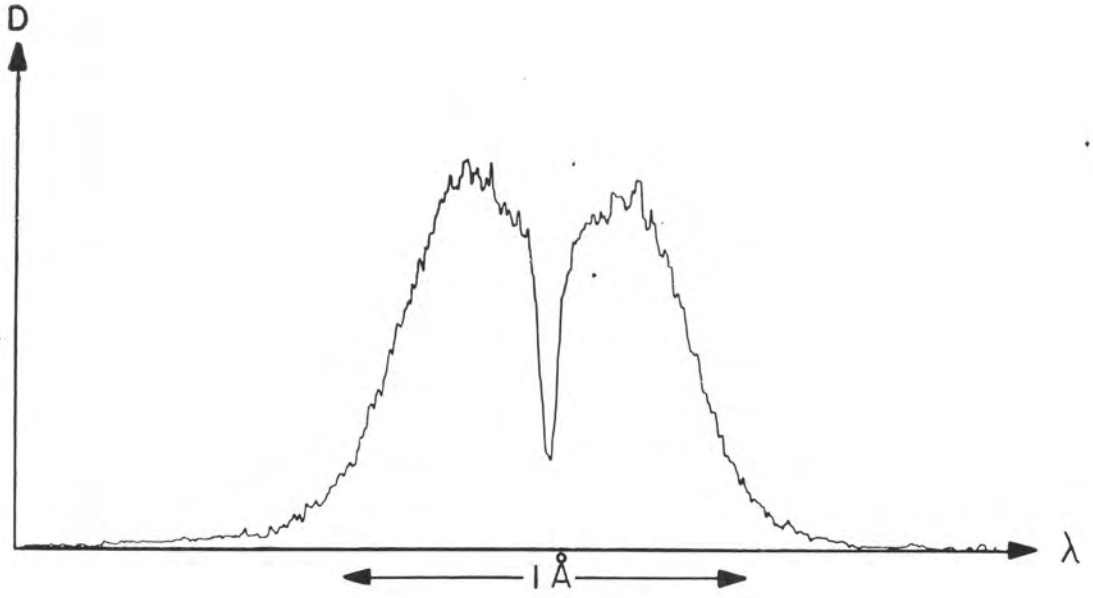
D
λ
1 Å

Chapter 2. The Absorption of Solar Ultra-Violet Radiation in the Earth's Atmosphere.

2.1 The Absorption Cross-Sections of the Principal Atmospheric Constituents.

This section deals with the photo-absorption cross-sections of all the atmospheric constituents which may be of importance in the absorption of solar radiation in the range 1000 to 1700Å. It is in this range that atmospheric absorption measurements can be made using the ion chambers described in Chapter 3. Particular attention will be given to absorption cross-sections at the Lyman-α line.

(a) Molecular Oxygen.

The absorption of molecular oxygen in the vacuum ultra-violet region has been investigated by a number of workers. The most detailed measurements are those of Watanabe et al. (1953a), Metzger and Cook (1964), and Blake et al. (1966). They were all made using photoelectric techniques and are substantially in agreement with one another. The general nature of the absorption spectrum can be seen from Figure 5. It is characterized by very wide variations in absorption cross-section. The Schumann-Runge continuum commences at about 1750Å and extends to 1300Å, the cross-section reaching a maximum of 1.48×10^{-20} cm^2 at 1425Å. It is associated with the dissociation

$$O_2\ (^3\Sigma_g^-) \rightarrow O\ (^3P) + O\ (^1D)$$

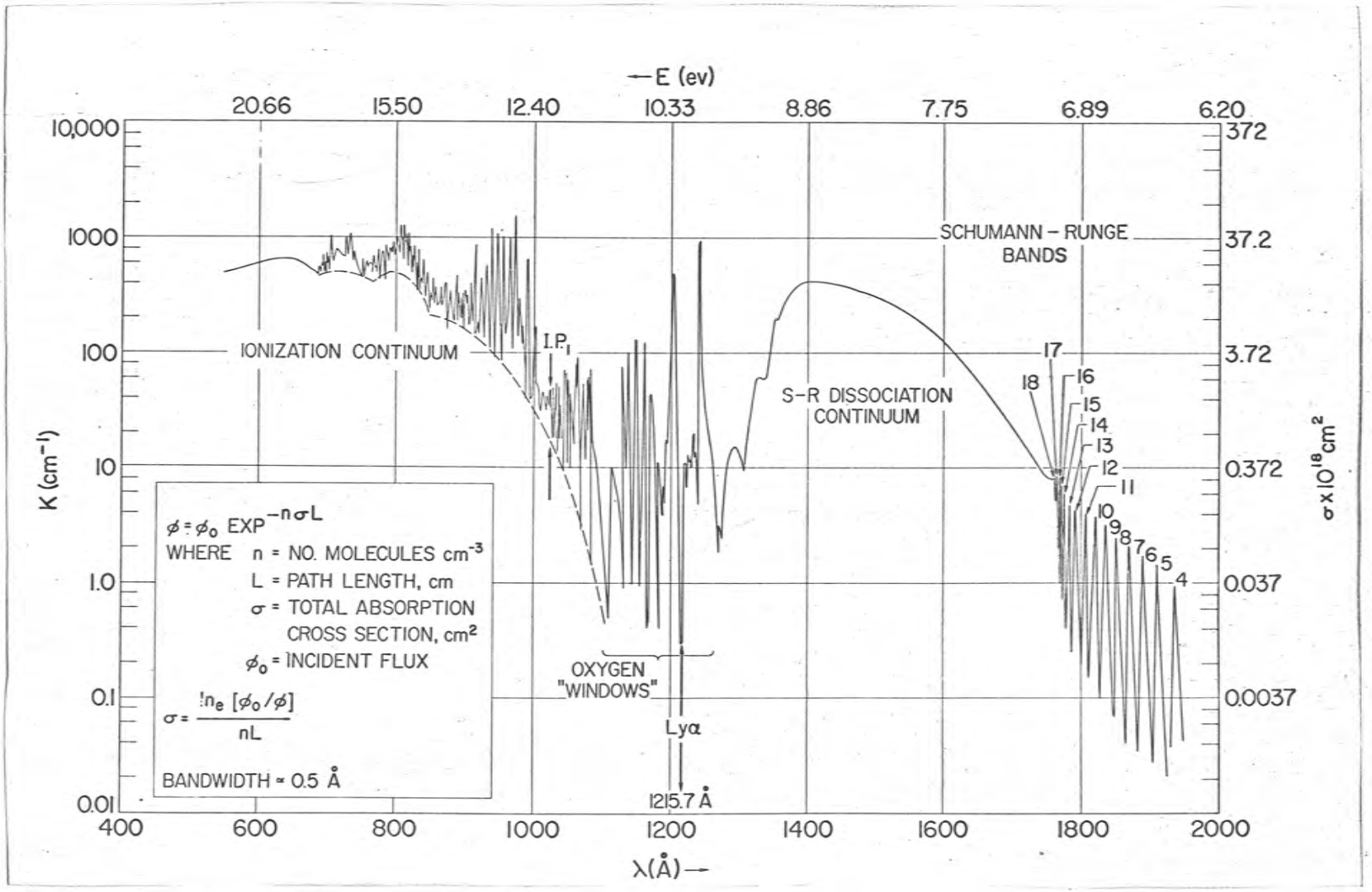

Figure 5. The absorption spectrum of molecular oxygen (from Cook and Ching (1965)).

To longer wavelengths there are the Schumann-Runge bands, the cross-section decreasing as the wavelength increases until they merge into the very weak Hertzberg continuum. At wavelengths shorter than 1300Å the spectrum shows a number of very strong diffuse absorption bands separated by "windows" where the cross-section is much lower. The window which coincides with the Lyman-α line has often been studied. Its shape is shown in Figure 6 (Blake et al. 1965 unpublished), together with a high resolution profile of the solar Lyman-α line. In spite of the narrowness of the window and the width of the Lyman-α line the almost exact coincidence of the centre of the window with the centre of the line means that the cross-section does not vary significantly across the line. The cross-section is pressure dependent at the bottom of the window, increasing linearly as the pressure is increased (Preston 1940, Blake et al. 1966). The rate of increase is about 1.7×10^{-23} cm^2 torr^{-1}. As the cross-section is of the order of 10^{-20} cm^2 the pressure dependence is negligible for the range of pressures encountered in the region of the atmosphere where solar Lyman-α radiation is absorbed (70 to 90 km). The values for the cross-section obtained by different workers are shown in Table 1.

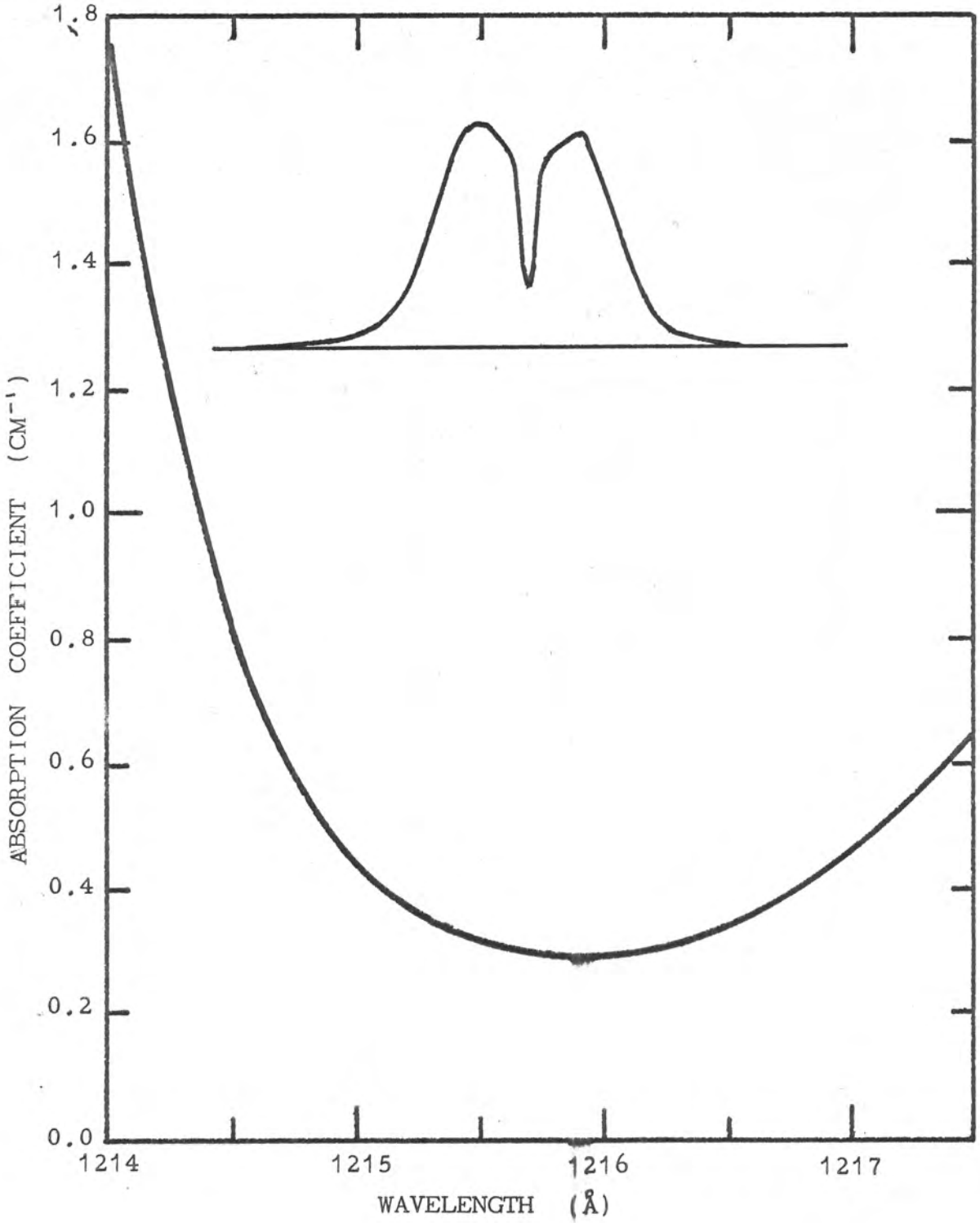

Figure 6. The absorption coefficient of molecular oxygen near the Lyman-α line (Blake et al., 1965 unpublished). Also shown is the shape of the solar line as given by Purcell and Tousey (see Figure 4).

TABLE 1

Investigator	Cross-Section	Pressure	Resolution
Preston (1940)	1.04×10^{-20} cm^2	extrapolated to zero pressure	
Watanabe et al. (1953a)	1.00	extrapolated to zero pressure	0.2Å
Ditchburn et al. (1954)	0.84	no pressure dependence	
Lee (1955)	0.85	no pressure dependence	
Metzger and Cook (1964)	1.04	9.3 torr	0.5Å
Blake et al. (1966)	1.12	extrapolated to zero pressure	1Å

Photographic measurement was used by Ditchburn et al. and Lee, and neither reported any pressure dependence. Photoelectric techniques were used by the other workers. A value of 1.00×10^{-20} cm^2 for the cross-section extrapolated to zero pressure has been used in the present work when calculating atmospheric oxygen densities from Lyman-α absorption measurements. This corresponds to an absorption coefficient of 0.269 cm^{-1}. The absorption coefficient for air, assuming that oxygen is the sole absorbing constituent will then be 0.0566 cm^{-1}.

(b) Molecular Nitrogen.

Molecular nitrogen absorbs strongly at wavelengths less than 1000Å, but above this the absorption spectrum consists

only of the very weak band systems corresponding to several forbidden transitions. The principal ones are the Lyman-Birge-Hopfield bands which start at 1450Å and have been observed down to about 1130Å. They correspond to the transition $a^1\Pi_g \leftarrow X^1\Sigma_g^+$. Because of the very small cross-section in these bands most measurements have provided only upper limits to the cross-section at various wavelengths. Lee (1955) found the cross-section to be less than 2×10^{-21} cm² at all wavelengths above 1040Å. The Lyman-α line lies between the (8,0) and (9,0) bands of the $a^1\Pi_g \leftarrow X^1\Sigma_g^+$ system, which are at wavelengths 1227 and 1206Å respectively (Tanaka 1955), so the cross-section here is particularly low. Upper limits which have been obtained are 2×10^{-22} cm² (Preston 1940), 3×10^{-22} cm² (Watanabe et al. 1953b), and 6×10^{-23} cm² (Ditchburn et al. 1954). None of these results supports the high cross-sections obtained by Weissler et al. (1952) above 1000Å.

(c) Water Vapour.

The absorption spectrum of water vapour is shown in Figure 7 (Watanabe and Zelikoff 1953). There are two continua with maximum cross-sections of 4.5×10^{-18} cm² at 1650Å, and 8.0×10^{-18} cm² at 1300Å. Below 1250Å the spectrum consists of bands in which the cross-section varies by about a factor of ten. In contrast to the situation with molecular oxygen the Lyman-α line lies very

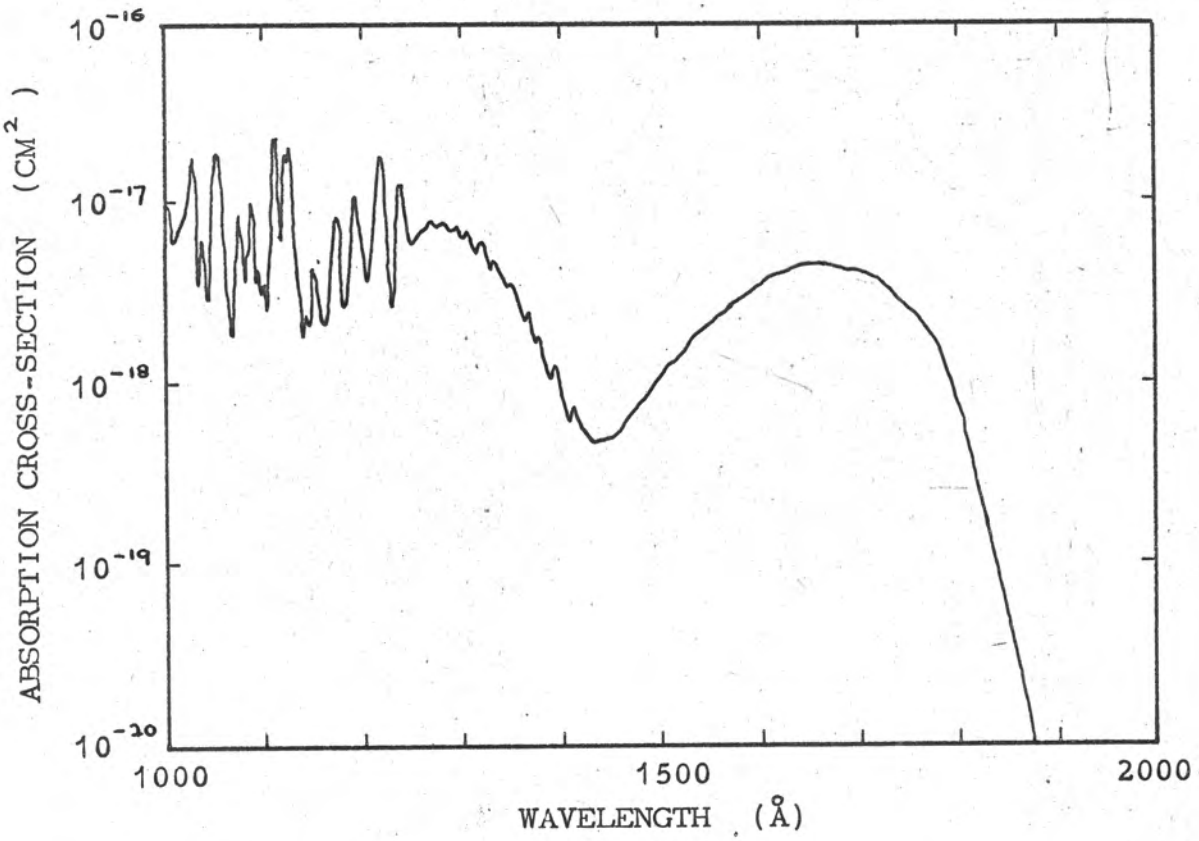

Figure 7. The absorption spectrum of water vapour (Watanabe and Zelikoff (1953)).

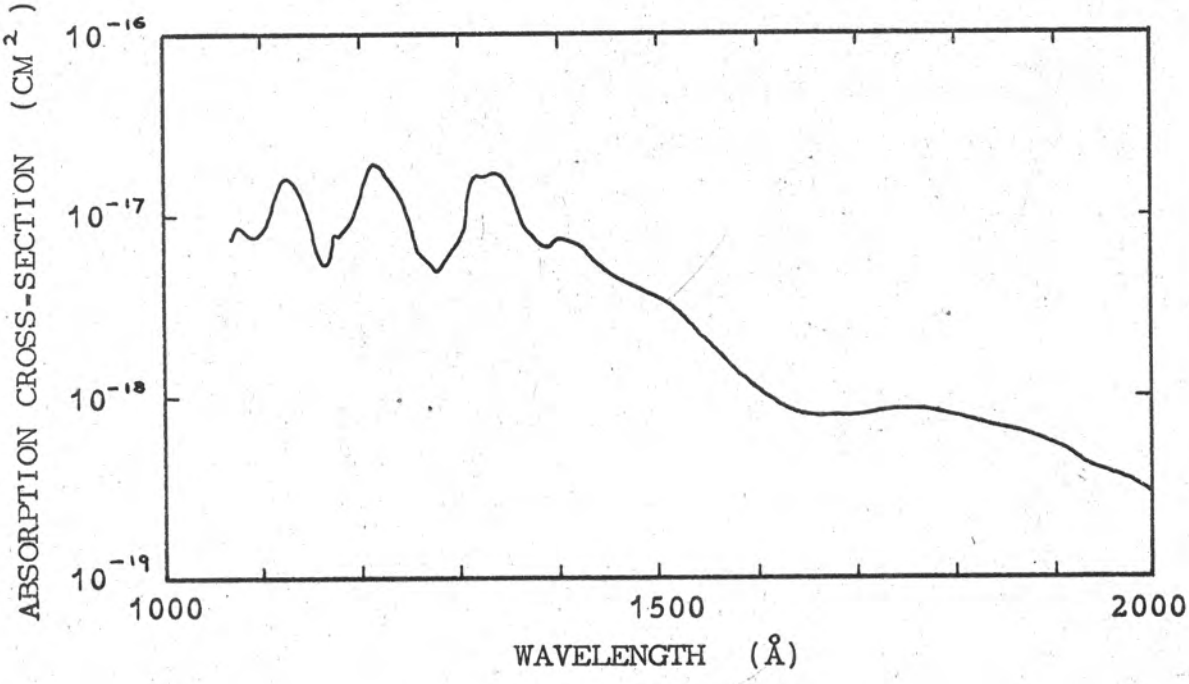

Figure 8. The absorption spectrum of ozone (Tanaka et al. (1953)).

near a maximum in the water vapour absorption spectrum. The values for the cross-section at Lyman-α obtained by various workers are 1.45×10^{-17} cm^2 (Preston 1940), 1.45×10^{-17} cm^2 (Watanabe and Zelikoff 1953), and 1.34×10^{-17} cm^2 (Ditchburn et al. 1954).

(d) Ozone.

Ozone absorbs strongly throughout the ultra-violet region, the cross-section being greater than 10^{-19} cm^2 at all wavelengths less than 3000Å. The variation of cross-section with wavelength in the region 1000 to 2000Å has been studied in detail by Tanaka et al. (1953), whose results are shown in Figure 8. Their value for the cross-section at Lyman-α is 2.3×10^{-17} cm^2.

(e) Carbon Dioxide.

The absorption spectrum of carbon dioxide is shown in Figure 9 (Inn et al. 1953). The Lyman-α line lies close to the minimum between the continuum which extends to wavelengths longer than 1200Å and the very strong bands which lie at wavelengths shorter than 1200Å. The value for the absorption cross-section at Lyman-α obtained by Inn et al. was 7.33×10^{-20} cm^2, which is very close to the value 7.47×10^{-20} cm^2 obtained by Preston (1940).

(f) Nitric Oxide.

The absorption cross-section of nitric oxide has been

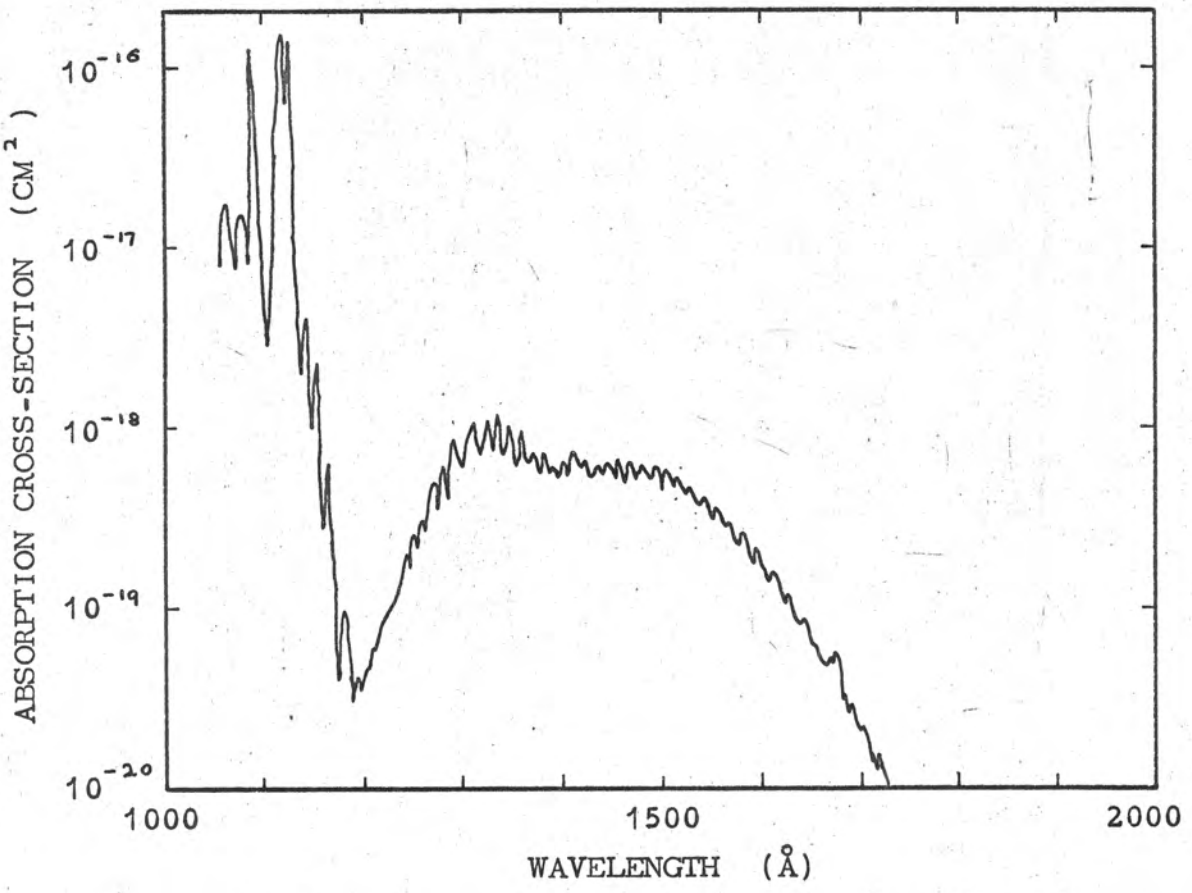

Figure 9. The absorption spectrum of carbon dioxide (Inn et al. (1953)).

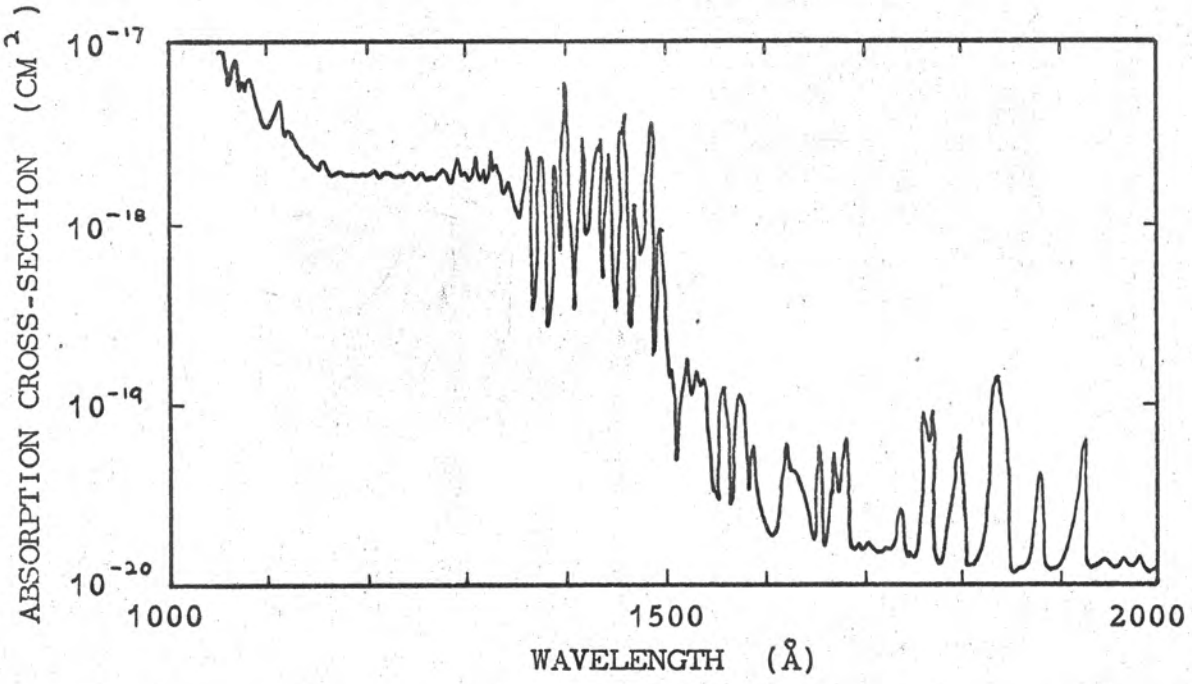

Figure 10. The absorption spectrum of nitric oxide (Marmo (1953)).

measured by Marmo (1953) and Watanabe (1954), their results being in good agreement. Figure 10 shows those of Marmo. At Lyman-α the values obtained were 2.5×10^{-18} cm^2 (Marmo) and 2.4×10^{-18} cm^2 (Watanabe).

(g) Atomic Oxygen and Atomic Nitrogen.

These two gases exhibit continuous absorption only below their first ionization limits which are 910Å for oxygen and 852Å for nitrogen. Thus they can be neglected in considering the absorption of solar radiation in the range 1000 to 1700Å. For the same reason the inert gases, which have ionization limits at 575Å (Ne), 787Å (A) and 886Å (Kr), need not be taken into account.

2.2 Absorption Processes Taking Place in the Atmosphere.

Table 2 shows the major constituents of the air in the homosphere (the region up to 90 km), and also some of the minor constituents which should be taken into consideration when dealing with ultra-violet absorption processes.

TABLE 2

		Fraction by Volume*
Major constituents		
nitrogen	N_2	.7808
oxygen	O_2	.2095
argon	A	.00934

TABLE 2 (Continued)

		Fraction by Volume*
Minor constituents		
carbon dioxide	CO_2	3×10^{-4}
water vapour	H_2O	$10^{-5} - 10^{-2}$
ozone	O_3	$10^{-7} - 10^{-5}$
nitric oxide	NO	$10^{-9} - 10^{-6}$

*The fractions for the major constituents are from the U.S. Standard Atmosphere, 1962, and for the minor constituents from Nicolet (1960) with some modification (see §5.8).

The relative concentrations of the major constituents remain constant throughout the homosphere, whereas the minor constituents have concentrations which are determined by photochemical and chemical reactions and so are rather variable. Very few direct experimental determinations have been made of the ozone and nitric oxide distributions above 70 km. In the case of the water vapour and carbon dioxide distributions there is no direct experimental evidence and theoretical estimates have to be used (see §5.8 for a discussion of the concentrations of the minor constituents in the 70 to 90 km region). Except for ozone, which is the only strong atmospheric absorber at wavelengths longer than 2000Å, the minor constituents account for only a small fraction of the absorption. Figure 11 shows the variation

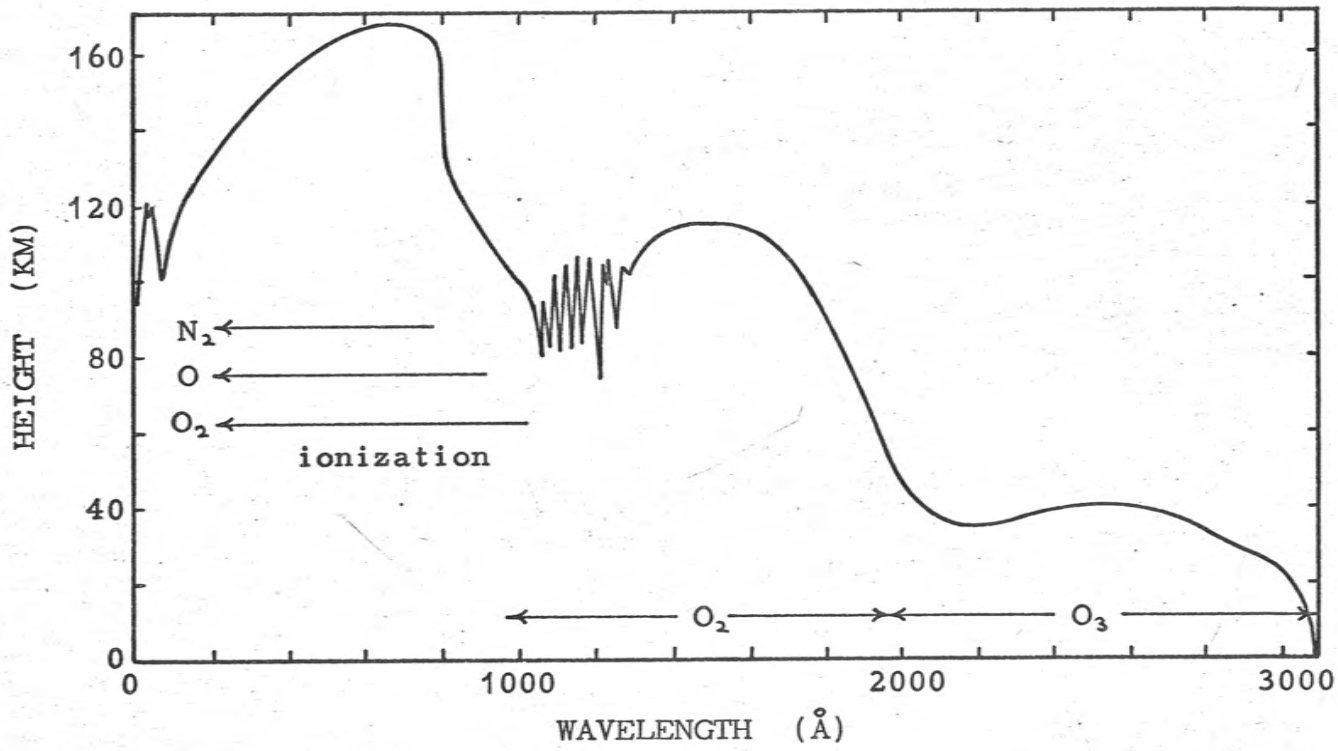

Figure 11. The penetration height h^* for solar ultra-violet radiation in the earth's atmosphere, plotted against wavelength (after Friedman (1960)). The principal absorbing constituents are indicated.

with wavelength of the penetration height h^* at which the solar flux has been attenuated to a fraction $\frac{1}{e}$ of its value outside the atmosphere (after Friedman 1960). From 2000 to 3000Å the radiation is absorbed by ozone which reaches its maximum concentration at an altitude of about 25 km. At shorter wavelengths molecular oxygen absorbs strongly and the absorption takes place at higher altitudes. Between 1000 and 2000Å the variation of h^* shows the same features as the variation with wavelength of the absorption cross-section of molecular oxygen. Absorption by the oxygen leads to its dissociation and the production of atomic oxygen. At wavelengths shorter than 1000Å molecular nitrogen also absorbs strongly, and atomic oxygen, which is the principal constituent above about 140 km, contributes to the absorption at wavelengths shorter than 700Å. The advent of high altitude rockets has made it possible to use the absorption of solar ultra-violet radiation as a means of investigating the distribution with altitude of various atmospheric constituents.

2.3 The Determination of Atmospheric Composition from Ultra-Violet Absorption Measurements.

2.3.1 The Absorption Law.

When monochromatic radiation passes through a gas the variation of the flux with distance through the gas is governed by the absorption law

$$\phi = \phi_0 \exp(-\sigma N) \qquad (1)$$

where ϕ is the flux in photons cm^{-2} sec^{-1},

σ is the absorption cross-section for the particular gas at the wavelength in question*, measured in cm^2,

N is the number of molecules in a column of area 1 cm^2, along the path the radiation has traversed,

and ϕ_0 is the flux where N = o.

The quantity $\tau = \sigma N$ is called the optical depth or optical thickness. If the number density of the gas molecules n cm^{-3} is constant over the path traversed by the beam the absorption law can be written

$$\phi(x) = \phi_0 \exp(-\sigma n x) \qquad (2)$$

where $\phi(x)$ is the flux after the beam has traversed a length x cm of the gas. Equation (2) may be written

$$\phi(x) = \phi_0 \exp(-ax) \qquad (3)$$

where $a = \sigma n$ is the absorption coefficient of the gas in cm^{-1}, at a number density n. The absorption coefficient can be determined in the laboratory by measuring the

---

* σ may depend on factors other than the type of molecule and the wavelength e.g. temperature and pressure. The latter effect is to be distinguished from the "Apparent pressure effect" due to variation of σ over the wavelength band which is being measured (see p.31).

transmission ϕ/ϕ_0 of a path length x of the gas. It is usually tabulated for the gas at S.T.P. (0°C and 760 torr pressure), and in the absence of temperature or pressure dependence of σ it may be calculated for any other conditions t°C and p torr pressure from the formula

$$a(t,p) = a_0 \times \frac{273p}{760(t + 273)} \qquad (4)$$

where a_0 is the absorption coefficient at S.T.P. The quantities a_0 and σ are related by $a_0 = \sigma n_0$ where n_0 is Loschmitt's number (2.687×10^{19} cm^{-3}).

Once the value of σ has been determined equation (1) can be used to determine N from a measured transmittance. This method has been used by a number of experimenters to determine number densities in the atmosphere using measurements of the attenuation of solar ultra-violet radiation at various altitudes. Both dispersing instruments such as photographic spectrographs and photoelectric monochromators, and non-dispersive detectors such as photon counters, ion chambers and photoelectric cells have been used (see §2.5).

2.3.2 Atmospheric Absorption

A detailed discussion of the interpretation of atmospheric absorption data is contained in a paper by Hinteregger (1962), and the notation used here is taken from that paper. If the radiation is being absorbed by a single constituent of the atmosphere the flux $\phi(\lambda,h,z)$, at

wavelength λ, height above the earth's surface h, and solar zenith angle* z, is given by

$$\phi(\lambda,h,z) = \phi_0(\lambda) \exp\left(-\int_h^\infty \sigma_i(\lambda) n_i(h)\,dh \sec z\right) \qquad (5)$$

where $\sigma_i(\lambda)$ is the absorption cross-section of the absorbing constituent,

$n_i(h)$ is the number density of the absorbing constituent,

and $\phi_0(\lambda)$ is the solar flux at wavelength λ.

This formula containing sec z is exact only for a planar atmosphere, but is a good approximation for the real (spherical) atmosphere when z is not too large. Hinteregger defines a quantity μ, which he calls the "extinction coefficient", by the relation

$$\mu(\lambda,h) = \frac{1}{\phi}\frac{\partial\phi}{\partial h}\cdot\cos z = \frac{\partial}{\partial h}(\ln\phi)\cdot\cos z \ . \qquad (6)$$

The extinction coefficient can be derived directly from the flux measurements, and may be regarded as the main experimentally determined quantity since the number densities can be expressed in terms of it. It should be noted that an absolute measurement of ϕ is not required to determine μ. In the case of absorption of monochromatic radiation by a

---

*The solar zenith angle is the angle between the direction of the sun and the zenith.

single constituent, as described by equation (5), the relation

$$\mu(\lambda,h) = \sigma_i(\lambda)n_i(h) \tag{7}$$

holds.

In general several constituents of the atmosphere will be absorbing the radiation, and then equation (5) must be replaced by

$$\phi(\lambda,h,z) = \phi_0(\lambda)\exp\left(-\int_h^\infty \Sigma_i \sigma_i(\lambda)n_i(h)dh \sec z\right) \tag{8}$$

where $\sigma_i(\lambda)$ and $n_i(h)$ refer to the different constituents. This can be rewritten

$$\phi(\lambda,h,z) = \phi_0(\lambda)\exp\left(-\int_h^\infty \sigma(\lambda,h)n(h)dh \sec z\right) \tag{9}$$

where $n(h) = \Sigma_i n_i(h)$ is the total number density, and $\sigma(\lambda,h)$ is the quantity defined by

$$\sigma(\lambda,h) = \frac{\Sigma_i \sigma_i(\lambda)n_i(h)}{n(h)} \quad . \tag{10}$$

Hinteregger calls $\sigma(\lambda,h)$ the "weighted mean absorption cross-section". In this case we have, from equation (9),

$$\mu(\lambda,h) = \sigma(\lambda,h)n(h) = \Sigma_i \sigma_i(\lambda)n_i(h) \quad . \tag{11}$$

In practice the quantity measured is not a monochromatic flux $\phi(\lambda,h,z)$, but the integrated flux $\phi(\lambda,\Delta\lambda,h,z)$ corresponding to an instrumental bandwidth $\Delta\lambda$ which may be only about 1 to 2Å, as in the case of the photoelectric monochromators, or 50 to 300Å, as in the case of the

ultra-violet ion chambers. The measured flux is then given by

$$\phi(\lambda,\Delta\lambda,h,z) = \int_{\lambda}^{\lambda+\Delta\lambda} \phi(\lambda,h,z)d\lambda$$

$$= \int_{\lambda}^{\lambda+\Delta\lambda} \phi_o(\lambda)\exp\left(-\int_{h}^{\infty}\sigma(\lambda,h)n(h)dh \sec z\right)d\lambda . \quad (12)$$

It can be shown that this leads to

$$\phi(\lambda,\Delta\lambda,h,z) = \phi_o(\lambda,\Delta\lambda)\exp\left(-\int_{h}^{\infty}\sigma_{eff}(\lambda,\Delta\lambda,h)n(h)dh \sec z\right) \quad (13)$$

where $\phi_o(\lambda,\Delta\lambda) = \int_{\lambda}^{\lambda+\Delta\lambda}\phi_o(\lambda)d\lambda$ and $\sigma_{eff}(\lambda,\Delta\lambda,h)$ is the quantity defined by

$$\sigma_{eff}(\lambda,\Delta\lambda,h) = \frac{\int_{\lambda}^{\lambda+\Delta\lambda}\phi(\lambda,h,z)\sigma(\lambda,h)d\lambda}{\phi(\lambda,\Delta\lambda,h,z)} . \quad (14)$$

Hinteregger calls $\sigma_{eff}(\lambda,\Delta\lambda,h)$ the "effective weighted mean absorption cross-section". If $\frac{\partial\sigma(\lambda,h)}{\partial h} = o$, then

$$\frac{\partial\sigma_{eff}}{\partial h} \geq o \quad (15)$$

i,e. if the composition of the air is constant, then σ_{eff} can only decrease or remain constant as the radiation penetrates down through the atmosphere. It will decrease when σ varies across the instrumental bandwidth, because the radiation of wavelengths at which σ is larger will be absorbed more

quickly leaving a higher fraction of the radiation of wavelengths at which σ is smaller. The changing distribution of flux within the bandwidth $\Delta\lambda$ is sometimes called "radiation hardening" and in laboratory measurements of absorption coefficients appears as an "apparent pressure effect" when the fine structure of $\sigma(\lambda)$ is smaller than the instrumental resolution. From equation (13), we have

$$\mu(\lambda,\Delta\lambda,h) = \sigma_{eff}(\lambda,\Delta\lambda,h)n(h) = \sum_i \sigma_{i,eff}(\lambda,\Delta\lambda,h)n_i(h) . \quad (16)$$

2.3.3 Absorption of Solar Radiation in the range 1000 to 1700Å.

At wavelengths less than 1000Å molecular nitrogen, molecular oxygen, and atomic oxygen all contribute to the atmospheric absorption (see §2.2), and the extinction coefficient must be measured at at least three wavelengths so that three equations like equation (16) are obtained which can be solved for the $n_i(h)$. However, between 1000 and 1700Å, the range covered by ion chambers, atmospheric absorption is due almost entirely to molecular oxygen i.e.

$$\sigma_{O_2}(\lambda)n_{O_2}(h) >> \sigma_2(\lambda)n_2(\lambda) + \sigma_3(\lambda)n_3(\lambda) + \cdots \quad (17)$$

in the height range near where $\frac{\partial\phi}{\partial h}$ is a maximum, the cross-sections $\sigma_2, \sigma_3, \cdots$ referring to the other constituents. (This statement may need some qualification in the case of Lyman-α radiation, but this will be discussed in detail in

§5.8). Under condition (17), equation (16) becomes

$$\mu(\lambda,\Delta\lambda,h) = \sigma_{O_2\,eff}(\lambda,\Delta\lambda,h)\,n_{O_2}(h) \tag{18}$$

where

$$\sigma_{O_2\,eff}(\lambda,\Delta\lambda,h) = \frac{\int_{\lambda}^{\lambda+\Delta\lambda} \phi(\lambda,h,z)\,\sigma_{O_2}(\lambda)\,d\lambda}{\phi(\lambda,\Delta\lambda,h,z)} \,. \tag{19}$$

The solar flux $\phi_o(\lambda)$ and the molecular oxygen absorption cross-section $\sigma_{O_2}(\lambda)$ vary widely with wavelength over the range 1000 to 1700Å (see §1.2 and §2.1 respectively), so it would appear that oxygen density determination using flux measurements made with ion chambers and equations (17) and (18) would be complicated. However, these equations can be considerably simplified in certain cases. Two important ones are

(a) When $\sigma_{O_2}(\lambda)$ is constant over the wavelength range λ to $\lambda+\Delta\lambda$ equation (19) becomes

$$\sigma_{O_2\,eff}(\lambda,\Delta\lambda,h) = \sigma_{O_2} \tag{20}$$

and equation (18) becomes

$$\mu(\lambda,\Delta\lambda,h) = \sigma_{O_2}\,n_{O_2}(h) \,. \tag{21}$$

These results are independent of the function $\phi_o(\lambda)$ which describes the intensity distribution in the solar spectrum over the range λ to $\lambda+\Delta\lambda$. An example is provided by an ion chamber, such as the one with a sapphire window and xylene filling,

which responds to the range 1420 to 1470 Å. Within this range the absorption cross-section of oxygen varies little (§2.1), and equation (20) and equation (21) are good approximations.

(b) If $\phi_0(\lambda)$ is much larger over some smaller range $\Delta\lambda'$ than elsewhere in the ion chamber range $\Delta\lambda$ then the effective value of the instrumental bandwidth is $\Delta\lambda'$. The best example of this occurs when the ion chamber responds to a range of wavelengths including the Lyman-α line which accounts for 80% of the solar intensity in the range 1050 to 1350 Å. In addition $\sigma_{O_2}(\lambda)$ varies little over the wavelength range covered by the Lyman-α line (§2.1) so that $\sigma_{O_2\,eff}=\sigma_{O_2}(1215.7)$ for an ion chamber sensitive to Lyman-α and

$$\mu(\lambda,\Delta\lambda,h) = \sigma_{O_2}(1215.7)n_{O_2}(h) \ . \qquad (22)$$

Also the coincidence of Lyman-α with a very sharp minimum in $\sigma_{O_2}(\lambda)$ (§2.1) means that most of the other wavelengths in the 1050 to 1350 Å range will be absorbed at much higher altitudes than the Lyman-α line, so that equation (22) will be a very close approximation to the actual conditions in the 70 to 90 km range where $\frac{\partial\phi}{\partial h}$ is a maximum.

2.3.4 The Shape of an Atmospheric Absorption Curve

Equation (6) can be rewritten

$$\phi(\lambda,\Delta\lambda,h) = \phi_0(\lambda,\Delta\lambda)\exp\left(-\int_h^\infty \mu(\lambda,\Delta\lambda,h)dh \sec z\right)$$

$$= \phi_0(\lambda,\Delta\lambda)\exp(-\tau) \qquad (23)$$

where the optical depth for the wavelength band λ to $\lambda+\Delta\lambda$ is defined by

$$\tau(\lambda,\Delta\lambda,h,z) = \int_h^\infty \mu(\lambda,\Delta\lambda,h)dh \sec z \ . \qquad (24)$$

It is convenient to introduce the penetration height h^* at which $\tau = 1$ i.e.

$$\int_{h^*}^\infty \mu(\lambda,\Delta\lambda,h)dh \sec z = 1 \ . \qquad (25)$$

Now consider a simplified situation in which

(a) the absorption is due to one constituent,

(b) the absorption cross-section σ of this constituent is constant over the range λ to $\lambda + \Delta\lambda$,

(c) the number density of this constituent varies exponentially with height i.e. $n(h)=n_0\exp(-h/H)$ where H is called the scale height.

Condition (c) will be a good approximation for any major constituent of the atmosphere over a limited height range. Under these conditions

$$\mu(\lambda, \Delta\lambda, h) = \sigma n(h) = \sigma n_0 \exp(-h/H) \qquad (26)$$

and so

$$\tau = \sigma n_0 H \sec z \exp(-h/H) \ . \qquad (27)$$

The variation of μ with height is shown in Figure 12(a). As μ is proportional to the slope of the graph of ln ϕ against height (equation (6)) the variation of ln ϕ with height will be as shown in Figure 12(b), and the variation of ϕ as shown in Figure 12(c). Using equations (23) and (27) the variation of ϕ with height can be tabulated as shown in Table 3.

TABLE 3

h	τ	ϕ/ϕ_0
$h^* + 3H$	0.05	0.95
$h^* + 2H$	0.14	0.87
$h^* + H$	0.37	0.67
h^*	1	0.37
$h^* - H$	2.7	0.067
$h^* - 2H$	7.4	0.00061

It can be seen that 90% of the absorption takes place over a height range of about 4H. This represents the practical limit to the range over which densities can be determined by the measurement of absorption at one value of σ. The range is limited at the upper end by the difficulty of measuring the relatively small changes in ϕ, and at the

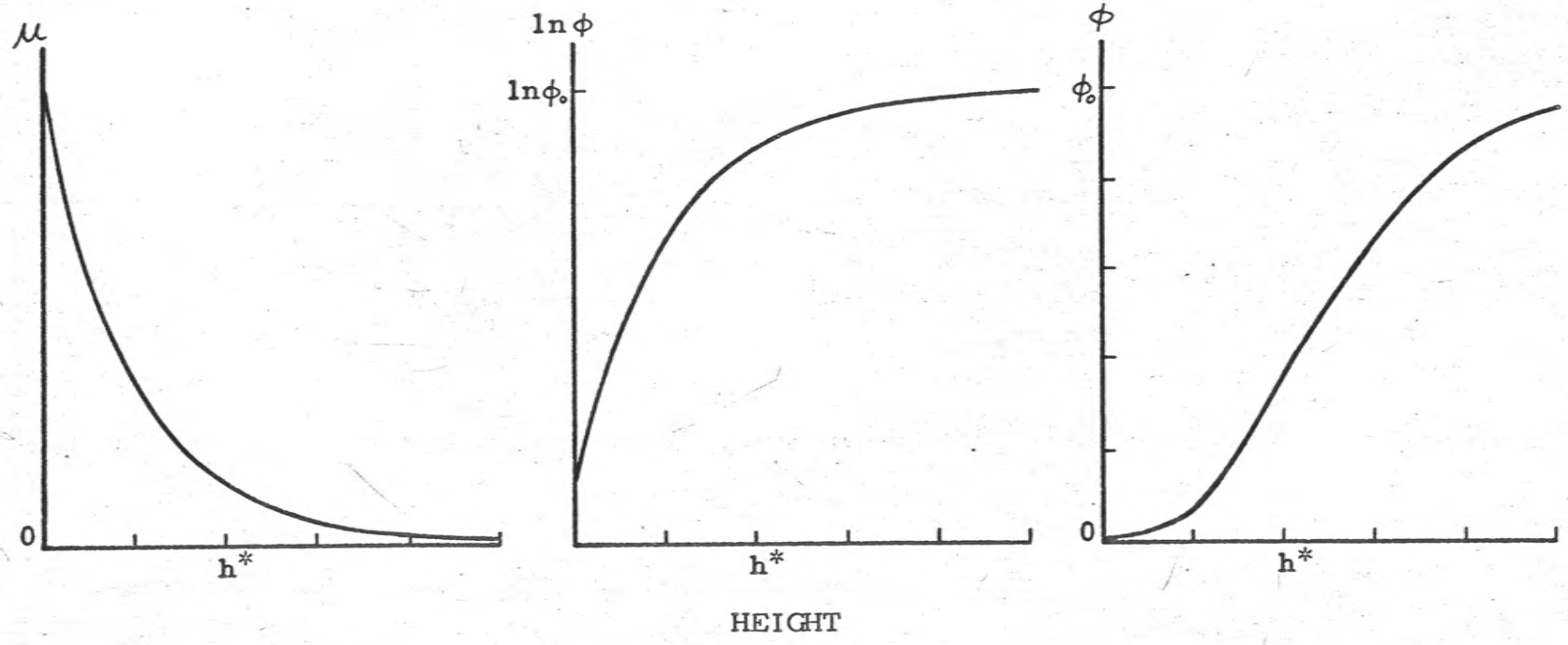

Figure 12. The variation with height of (a) the extinction coefficient μ, (b) the logarithm of the radiation flux $\ln\phi$ and (c) the radiation flux ϕ, for the absorption of monochromatic radiation in a homogeneous, isothermal atmosphere. The height scales are marked in units of the scale height H. h^* is the penetration height (see p.34).

lower end by the difficulty of constructing a measuring system which can accommodate the very wide range of variation of ϕ. In practice the instruments used usually have a range of about a factor of twenty.

Since $\sigma n_0 H \sec z \exp(-h^*/H) = 1$ the effect of altering z is to alter h^*, but the values given in Table 3 will not be affected, so the final result is that the absorption takes place higher up but over exactly the same range of heights. This statement is exactly true, of course, only for a planar atmosphere with the simplifying assumptions made above. When the zenith angle changes from 0 to z the absorption curve moves up by an amount h' given by $\sec z = \exp(h'/H)$ (equation (27)). Some values of h' are shown in Table 4.

TABLE 4

z	h'/H
0°	0
20°	0.06
40°	0.27
60°	0.69

It can be seen from the table that the range over which density can be determined from an absorption measurement is not raised much for quite large variations of zenith angle. In fact, because of the spherical shape of the actual

atmosphere, the range is not raised more than several scale heights for zenith angles up to 90°.

2.4 The Determination of Temperature Profiles from Density Profiles.

The basic equations governing the structure of the atmosphere are

(a) $p_i = n_i kT$ (The Gas Law)

where p_i is the partial pressure and n_i the number density of the constituent i, k is Boltzmann's constant, and T is the absolute temperature.

We may also write

$p = nkT \qquad p = \Sigma p_i, \quad n = \Sigma n_i$

where p and n are the total pressure and total number density.

(b) $\rho_i = m_i n_i \quad \rho = \Sigma m_i n_i$

where ρ_i is the density and m_i the molecular mass of constituent i, and ρ is the total density.

(c) $dp = -\rho g dh$ (The Hydrostatic Law)

The determination of the number density of one constituent $n_i(h)$ as a function of height will not in general allow a temperature profile to be calculated. However, there are two special situations in which the calculation can be made. These are

(a) Diffusive equilibrium

This is the situation where each constituent is distributed in height just as if it were the only constituent i.e. each constituent behaves independently of the others. Then

$$p_i(h_o) = \int_{h_o}^{\infty} \rho_i(h) g dh$$

$$= m_i \int_{h_o}^{\infty} n_i(h) g dh \qquad (1)$$

and

$$T(h_o) = \frac{m_i \int_{h_o}^{\infty} n_i(h) g dh}{n_i(h_o) k} \quad . \qquad (2)$$

(b) Mixing

In this case each constituent occupies a constant fraction by volume (i.e. number density) of the air. If the fraction occupied by the constituent i is $r_i = \frac{n_i}{n}$ and we define a mean molecular mass $\bar{m} = \frac{\Sigma m_i n_i}{n} = \frac{\rho}{n}$, then

$\rho = n\bar{m} = \frac{\bar{m} n_i}{r_i}$. Now

$$p_i(h_o) = r_i p(h_o)$$

$$= r_i \int_{h_o}^{\infty} \rho(h) g dh$$

$$= r_i \int_{h_o}^{\infty} \frac{\bar{m} n_i(h) g}{r_i} \, dh$$

$$= \bar{m} \int_{h_o}^{\infty} n_i(h) g \, dh \qquad (3)$$

and

$$T(h_o) = \frac{\bar{m} \int_{h_o}^{\infty} n_i(h) g \, dh}{n_i(h_o) k} \cdot \qquad (4)$$

Molecular oxygen is probably in diffusive equilibrium above about 120 km during the day (Kallman-Bijl and Sibley 1963), and below 90 km there is mixing, the mean molecular mass being 28.96 (U.S. Standard Atmosphere, 1962). Between 90 and 120 km, where the photodissociation of oxygen takes place, neither of the situations described above are applicable.

As the number density measurements do not extend to an infinite height, but only to some maximum height h_m, the integral in equation (4) cannot be evaluated from the measurements alone. There are two ways of overcoming this difficulty. The first is to make a direct estimate of $\int_{h_m}^{\infty} n_i(h) g \, dh$ from an extrapolation of the $n_i(h)$ curve. The second, more usual, method is to assume a temperature T_m at h_m and calculate $\int_{h_m}^{\infty} n_i(h) g \, dh$ from

$$T_m = \frac{\bar{m}\int_{h_m}^{\infty} n_i(h)g\,dh}{n_i(h_m)k} \quad . \qquad (5)$$

Whichever method is chosen the integral above h_m soon becomes a very small part of the total integral as the integration is extended down from h_m, since $n_i(h)$ increases approximately exponentially as h decreases, and so the actual choice made has little effect on the temperature values at heights more than about a scale height below h_m.

The value of g will usually be sufficiently constant over the height range used in the integration for an average value $\bar{g}$ to be used and it can then be taken out of the integral giving

$$T(h_o) = \frac{\bar{m}\left[\bar{g}\int_{h_o}^{h_m} n_i(h)dh + \int_{h_m}^{\infty} n_i(h)g\,dh\right]}{n_i(h_o)k} \quad . \qquad (6)$$

Finally it may be noted that in the case where the initial absorption measurement is made with monochromatic radiation the integral $\int_{h_o}^{h_m} n_i(h)dh$ may be obtained directly from the flux measurements using the relation

$$\int_{h_o}^{h_m} n_i(h)dh = \frac{1}{\sigma \sec z} \ln \frac{\phi(h_o)}{\phi(h_m)} \quad . \qquad (7)$$

2.5 Previous Measurements of Molecular Oxygen Densities

In this section the various methods which have been used to obtain molecular oxygen densities in the region 70 to 180 km will be discussed. This is the region in which oxygen densities can be determined from measurements of the absorption of solar ultra-violet radiation, made with ion chambers, and this technique will be compared with the others, both those based on the absorption of solar ultra-violet radiation, and those using some completely different method. The results of all the measurements mentioned below are displayed in Figure 13.

The first attempt to measure the absorption of solar ultra-violet radiation in the atmosphere was made in 1949 (Friedman et al. 1951) using two kinds of photon counter, the first having a lithium fluoride window and chlorine filling, and the second a sapphire window and bromine filling. They responded to the ranges 1180 to 1300Å and 1425 to 1650Å respectively. However, saturation of the counters, and some unwanted long wavelength response, made the analysis difficult and no oxygen densities were obtained. The results of similar experiments in 1952 (Byram et al. 1953) with these counters were also unsuitable for determining oxygen densities, but a plot of the intensity in the 1180 to 1300Å band against slant air

Figure 13. The results of experimental determinations of molecular oxygen densities in the range 60 to 180 km by workers using various methods. The height range within which each method is applicable is shown in the figure.

LEGEND

	———	U.S. Standard Atmosphere 1962 (see p.48)
Photographic spectrograph	+	Jursa et al. (1963, 1965) (32°N)
Photoelectric monochromator	■	Hall et al. (1963b, 1965)
Mass spectrometer	×	Nier et al. (1964) (see footnote p.48)
1450Å Counter	▽	Friedman et al. (1964)
Lyman-α ion chamber	▲ ●	Present work (summer 31°S)
"	◇	Smith and Weeks (1965) (summer 59°N)
"	○	" (summer 38°N)
"	□	" (autumn 38°N)
"	△	" (winter 38°N)
"	—·—·—	Kupperian et al. (1959) (summer 59°N)*
"	— — — —	" (spring 59°N)*
1220 to 1350Å ion chamber	·····	" (spring 59°N)

*Densities adjusted to a cross-section of 1.00×10^{-20} cm² at Lyman-α (see footnote p.44).

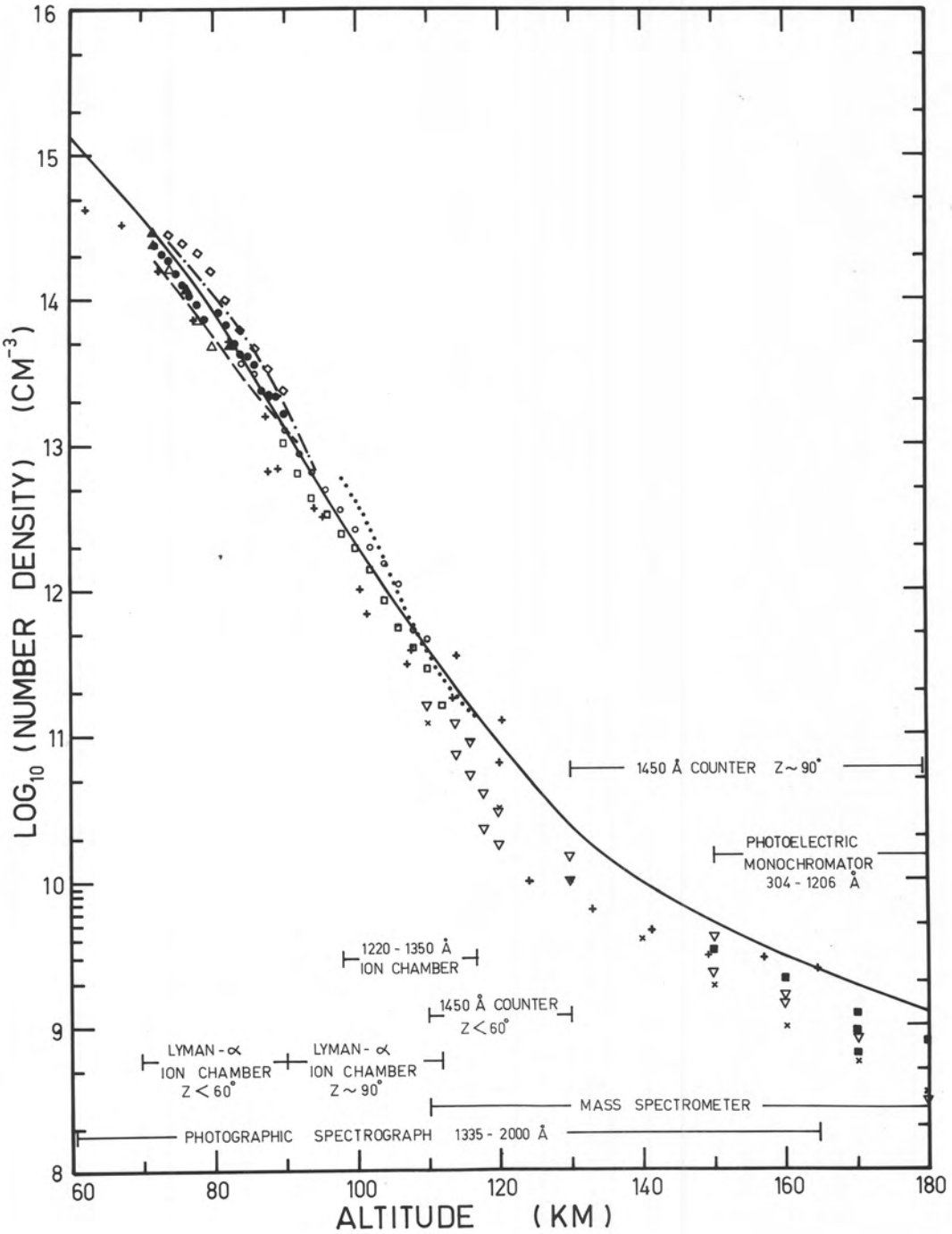
16
15
14
13
12
11
10
9
8
60
80
100
120
140
160
180
LOG10 (NUMBER DENSITY) (CM-3)
ALTITUDE (KM)
1450 Å COUNTER Z~90°
PHOTOELECTRIC MONOCHROMATOR 304 - 1206 Å
1220 - 1350 Å ION CHAMBER
1450 Å COUNTER Z<60°
LYMAN - ∝ ION CHAMBER Z<60°
LYMAN - ∝ ION CHAMBER Z~90°
MASS SPECTROMETER
PHOTOGRAPHIC SPECTROGRAPH 1335 - 2000 Å

mass* obtained from the Rocket Panel showed that this radiation was absorbed in the air as if it were monochromatic, and that the absorption coefficient was close to that of Lyman-α in dry air.

A new counter which had a sapphire window, and a filling of nitric oxide, xylene and helium, was first used in 1953 (Byram et al. 1955). It responded to the range 1425 to 1500Å, but had a much lower long wavelength response than the previous counter sensitive to this range. As can be seen from the plot of h^* in Figure 11, absorption measurements made with this counter can be used to determine oxygen densities in the 120 km region. The analysis of the results is relatively easy since the absorption cross-section of oxygen does not vary greatly within the sensitive range of the counter (see §2.3.3). Densities obtained from the results of this experiment and similar ones in 1955 and 1963 are shown in Figure 13 (marked ∇). All the densities are taken from the paper by Friedman et al. (1964). Two of the experiments were carried out when the solar zenith angle was close to 90° so that the region in which densities were determined was 130 to 180 km instead of 110 to 130 km as in the other experiments.

---

*The slant air mass is the mass of air in a column of unit area of cross-section between the detector and the sun.

Ion chambers were first used for absorption measurements in 1955 (Byram et al. 1956, Chubb et al. 1958). The ion chambers, which were sensitive to Lyman-α, had windows of lithium fluoride and fillings of nitric oxide. However, the Lyman-α measurements were not used for calculating oxygen densities and it was suggested, on the basis of the absorption coefficient obtained from a plot of Lyman-α intensity against slant air mass taken from the Rocket Panel, that water vapour accounted for approximately half the absorption of Lyman-α in the atmosphere. Although this was due mainly to a misconception concerning the Rocket Panel densities,* the question of absorption of Lyman-α by water vapour requires examination and will be discussed separately (§5.8). Two further flights were made in 1957 and 1958 (Kupperian et al. 1959), using both the ion chamber sensitive to Lyman-α, and one sensitive to the range 1220 to 1340Å (calcium fluoride window, nitric oxide filling). Absorption measurements

*A value of 0.044 cm^{-1} was obtained for the absorption coefficient of Lyman-α in air (Chubb et al. 1958), but it was assumed that the Rocket Panel densities were too high by a factor of two. While this subsequently proved to be correct for the region above 100 km it was not true for the region of Lyman-α absorption (70 to 90 km), where the Rocket Panel densities are only about 10% higher than those of the U.S. Standard Atmosphere (1962). When the absorption coefficient is corrected by this factor a value of 0.048 cm^{-1} is obtained. This is close to the presently accepted value of 0.0566 cm^{-1} for the absorption coefficient of Lyman-α in dry air (see p.20), although still below it, and so these results actually imply that water vapour does not make a large contribution to the absorption of Lyman-α in the atmosphere.

made with both chambers were used to derive oxygen densities (Figure 13*, marked ⁝⁝). Analysis of the data from the chamber sensitive to Lyman-α is straightforward due to the predominance of this line in the solar spectrum (see §2.3.3), but the analysis of the data from the other chamber was more complicated owing to the detection of radiation with widely varying absorption coefficients in oxygen.

Measurements of the absorption of Lyman-α radiation, made with ion chambers, have also been used by Smith and his colleagues (Smith et al. 1965, Smith and Weeks 1965) to determine oxygen densities (Figure 13, marked ◇ ○ □ △). They used both chambers filled with nitric oxide, and ones filled with carbon disulphide, but found that the latter showed some decrease in sensitivity during the period of the rocket flight. By carrying out some of the measurements when the solar zenith angle was close to 90°, densities were obtained for the 90 to 112 km region, as well as for the 70 to 90 km region covered by the flights at smaller zenith angles. The measurements were made at two different latitudes (38°N and 59°N) and in different seasons of the

---

*Kupperian et al. used a value of 0.82×10^{-20} cm² for the absorption cross section of oxygen at Lyman-α when analysing their results. However, both the results of Smith and Weeks (1965) and those of the author were derived using a value of 1.00×10^{-20} cm². Therefore, in order to make all the densities obtained from Lyman-α absorption measurements directly comparable, those of Kupperian et al. have been multiplied by 0.82/1.00 before inclusion in Figure 13.

year, and some conclusions have been drawn concerning latitude and seasonal variations in the oxygen densities (Smith and Weeks 1965).

Figure 13 also shows the results obtained from measurements on the absorption of Lyman-α radiation in the present work, as described in Chapter 5 (marked ▲ ●).

Jursa et al. (1959, 1963, 1965) have used a different method of measuring the absorption of ultra-violet radiation in the atmosphere. Making use of the Aerobee pointing control, they have flown a number of times between 1958 and 1963 photographic spectrographs covering the range 1000 to 3000Å. The resolution was sufficient to resolve the rotational structure of the Schumann-Runge bands of molecular oxygen, which appeared as absorption bands in the spectra taken in the 60 to 90 km region. Oxygen densities were derived from the variation with height of intensity in the region of the Schumann-Runge bands and at various wavelengths within the Schumann-Runge continuum. Because of the wide range of molecular oxygen absorption cross-sections covered (see Figure 5), densities were obtained at heights varying from 60 to 165 km (Figure 13, marked +). A very direct method was used to calibrate the instruments in the region of the Schumann-Runge bands. Spectra were taken in the laboratory with various path lengths of oxygen included in front of the spectrograph. In this way the depths of

the Schumann-Runge bands were determined as functions of the absorbing path length of oxygen. This method eliminates the possible effect of variation in the apparent absorption cross-section due to insufficient instrumental resolution (see p. 31).

Hinteregger and his co-workers have used the photoelectric monochromators described in §1.1.1 to carry out absorption measurements in the atmosphere. These instruments are limited to wavelengths less than 1300Å, and can only be operated at heights above about 120 km due to the effect of the air on the open photomultiplier. Thus, although the Lyman-α line is detected, its absorption cannot be measured with these instruments. Absorption analysis is most conveniently carried out at the wavelengths of strong solar emission lines. Plots of intensity against height for twenty of these lines, measured during a flight in 1961, are given by Hall et al. (1963a). Only one line (the SiIII line at 1207Å) is absorbed exclusively by molecular oxygen; the others lie below 1026Å and are absorbed also by molecular nitrogen or atomic oxygen or both. Measurements of the 1207Å line give molecular oxygen densities directly, while measurements of the other lines can be combined to obtain O_2, N_2, and O density profiles. The method used is described in a paper by Hinteregger (1962) which also gives the density distributions obtained

from an analysis of the results of the 1961 measurements. Density values derived from the results of two similar flights made in 1962 (Hall et al. 1963b) are shown in Figure 13 (marked ■).

A considerable improvement in this technique was made in 1963 using a fixed wavelength photoelectric monochromator (Hall et al. 1965). Nine selected strong solar emission lines between 304 and 1207Å were monitored in turn, instead of scanning through the whole wavelength range 300 to 1300Å as in previous experiments. This change effected an improvement by a factor of 3.3 in altitude resolution and a factor of 3.5 in counting statistics. The molecular oxygen densities obtained from this flight are also shown in Figure 13 (marked ■).

A completely different approach to the determination of atmospheric composition has been made by Nier et al. (1964) who used mass spectrometers flown in a rocket. Problems associated with contamination by gases given off by the rocket itself were reduced by sealing the mass spectrometers until they reached an altitude of approximately 100 km, and pumping them continuously with ion pumps. A complete mass spectrum was scanned once every two seconds and telemetered to the ground. Densities were derived at 10 km intervals from 110 to 210 km, the molecular oxygen

densities being shown in Figure 13 (marked ×)*.

Also shown in Figure 13 is an oxygen density profile derived from the U.S. Standard Atmosphere, 1962. This is a model atmosphere which represents the average values of many measurements of the temperature, total pressure and total density. In it the composition of the air is assumed to be constant below 90 km and so the molecular oxygen number density has been derived by multiplying the total number density by 0.2095, the sea-level fraction of oxygen. Above 90 km the composition changes due to dissociation of the oxygen, the change being represented in the Standard Atmosphere by a decrease in the molecular weight. The oxygen density profile above 90 km in Figure 13 has been calculated on the assumption that the fractions by weight of all the constituents except atomic and molecular oxygen remain constant and that the change in molecular weight is due only to the dissociation of molecular oxygen into atomic oxygen.

Several methods of obtaining number densities of individual atmospheric constituents have been described above, each of which has its own advantages. The

---

*Two sets of results were given. The one based on the assumption that the air molecules retained their ambient temperature when they were measured has been selected. The values in the other set differ by a factor which varies from 1.07 at 110 km to 0.5 at 180 km.

photoelectric monochromators provide the most detailed information, since they give an absorption curve for each of a number of strong solar lines, with good height resolution. As has been pointed out, however, the instrument is limited to operation above about 120 km. The photographic spectrographs are not so limited, but here the accurate determination of the solar fluxes is much more difficult. The main difficulty is in the calibration of the film, which is estimated to give rise to an error of about 50% (Jursa et al. 1963). Moreover, the number of exposures is limited and each exposure covers a considerable height range (3 to 9 km), so the height resolution is not good. Both these instruments require the use of a pointing control.

Non-dispersive measurements of ultra-violet absorption using ion chambers or counters have the advantage of not requiring a pointing control, and of being, in general, much simpler and less expensive than the dispersive experiments. They require a minimum of rocket space and telemetry. This compensates to some extent for the less detailed information which they provide. The height resolution of the absorption measurements made with non-dispersive detectors under favourable conditions is better than that of the measurements made with the photoelectric monochromator (compare flux measurements every 0.3 sec for HAD 304 (Chapter 5) with

measurements every 3 sec for the monochromator (Hall et al. 1965)).

The mass spectrometer, which also does not require a pointing control, is completely independent of a knowledge of absorption cross-sections, but is very difficult to calibrate absolutely (Nier et al. 1964). Difficulties arise with calibration for atomic oxygen, dependence of response on the orientation of the rocket, production of various atoms or molecules (e.g. atomic nitrogen) in the instrument itself, and uncertainty about the relationship between the temperature of the molecules in the ion source and those in the surrounding air. In spite of these difficulties the results obtained are in good agreement with those from the ultra-violet absorption measurements. The mass spectrometer is limited to operation above about 100 km.

In addition to the techniques described above there are several methods which have been used to measure total atmospheric density. These include the use of grenades, falling spheres and various types of gauges carried in rockets.

Chapter 3. Ion chambers for the Detection of Vacuum Ultra-Violet Radiation

3.1 Introduction

As pointed out in §2.5, experiments using dispersive instruments to study solar radiation in the vacuum ultra-violet region require a rocket with a pointing control, owing to the low sensitivity and narrow field of view of such instruments. Thus there is considerable value in having non-dispersive, but spectrally selective detectors which have sufficiently high sensitivity and wide field of view to be used in unstabilized rockets. In the laboratory, also, such detectors are useful when it is desired to detect vacuum ultra-violet radiation in the presence of a background of longer wavelength radiation. For use in rockets it is necessary that the detector provide an electrical output which can be telemetered to the ground during the flight. Two basic types of detector are available: (a) those in which the photoelectric effect at the surface of a solid is used, and (b) those in which the photoionization of a gas is used. Detectors of the first type have been described by Dunkelman et al. (1963). Photodiodes and photomultipliers having conventional Cs - Sb photocathodes, which respond throughout the visible and ultra-violet regions of the spectrum, can be combined with filters of various kinds to restrict the spectral response. Interference filters can

be made which transmit narrow spectral bands at wavelengths longer than 2000Å. None have, however, been made which transmit at wavelengths shorter than 2000Å. A different approach is to limit separately the response of the photoelectric cell on the short and long wavelength sides. Limitation of the response on the short wavelengh side is comparatively easy, since there are many solids which can be made into windows, and which transmit only radiation of wavelength longer than a certain limit. The transmissions of the most useful materials which are available at present are given by Dunkelman et al. (1963). Recently new photocathodes such as Cs - Te, Cs - I and Cu - I have been developed which have high sensitivities to radiation in the vacuum ultra-violet region but respond only weakly to longer wavelength radiation (Dunkelman et al. 1962). The cut-offs are not as sharp as those provided by the windows, the sensitivity decreasing over a range of several hundred angstroms in most cases. Pure metals such as nickel, tungsten and tantalum have also been used as photocathodes. These exhibit sensitivities which increase as the wavelength of the radiation decreases. The increased quantum yield (number of photoelectrons released per incident photon) at short wavelengths has been ascribed by Hinteregger and Watanabe (1953) to the internal photoelectric effect, which has both a higher work function and quantum yield than the

surface photoelectric effect. The quantum yields of metals for the surface photoelectric effect often depend on the condition and previous treatment of the surface, and therefore vary considerably from one surface to another.

Detectors employing the photoionization of a gas, on the other hand, will have a quite definite upper limit to their wavelength sensitivity. A molecule of the gas can be ionized only by a photon which has an energy greater than the first ionization potential of the molecule. The ionization potential decreases slightly as the temperature of the gas increases owing to thermal excitation but this effect is small in practice (see §3.9). The photoionization efficiency (number of photoelectrons produced per photon absorbed in the gas) is usually quite high (greater than 10%), and although it may fluctuate with wavelength the magnitude of the variation is small for most gases. The way in which the photoionization efficiency varies with wavelength near the threshold depends on the type of molecule. Molecules having an efficiency which rises sharply at the threshold are most suitable for radiation detectors. According to Watanabe et al. (1962), these include simple diatomic molecules (such as nitric oxide), alkyl halides, aldehydes and ketones, and simple aromatic compounds such as benzene and xylene. These observations are confirmed in the

present work (see Figure 25).

Detectors using the photionization of a gas, together with an appropriate window to provide the low wavelength limit, were first constructed by Chubb and Friedman (1955). Their detector operated as a Geiger counter, the photoelectrons from the gas initiating the avalanches. The counters proved rather unreliable in use however, their sensitivity changing with time, apparently because of changes in the counting efficiency (number of avalanches produced per photoelectron released in the gas). They were replaced by ion chambers (Friedman et al. 1958) in which the photoelectrons were collected by applying a potential difference of about 50V across the chamber and then measured as an electron current.

If the spectral response of the ion chamber is to have a sharp cut-off at the photoionization threshold of the filling gas there must be negligible response due to photoelectric emission from the cathode, which may be either the wall of the chamber, or the central wire. This will usually be the case for the following reasons:

(a) The filling gas will usually absorb strongly even at wavelengths above the photoionization threshold and so prevent this radiation reaching the wall. Since the photoelectric yield of metals decreases rapidly as the wavelength increases, the radiation most effective in releasing electrons from the wall

will probably be absorbed before reaching the wall.

(b) As was found by Chubb and Friedman (1955) the photoelectric yield of a surface is decreased in the presence of the filling gas, particularly if the gas is electronegative.

Ion chambers with machined copper bodies have been designed by workers at the U.S. Naval Research Laboratories (Friedman et al. 1958, 1964), and University College, London (Willmore 1961), while moulded ceramic bodies have been used by workers at the Goddard Space Flight Center (Stober et al. 1963).

3.2 Construction of the Ion Chambers

A cross-sectional diagram of the ion chamber used in the present work is shown in Figure 14. The design was such that the chambers could be quickly and easily assembled. The body consisted of a piece of 1 inch diameter copper tubing into which two pressed copper end pieces were soldered. Specially made dies were used to form the end pieces from copper sheet. A kovar-glass seal supported the central wire which was a length of 1 mm diameter ground tungsten rod. The seal included a guard ring and had a leakage resistance greater than $10^{13}\Omega$ between the guard ring and either of the other electrodes. The filling tube was made from 0.052 in I.D. annealed copper tubing. Soft silver solder was used in assembling the chamber.

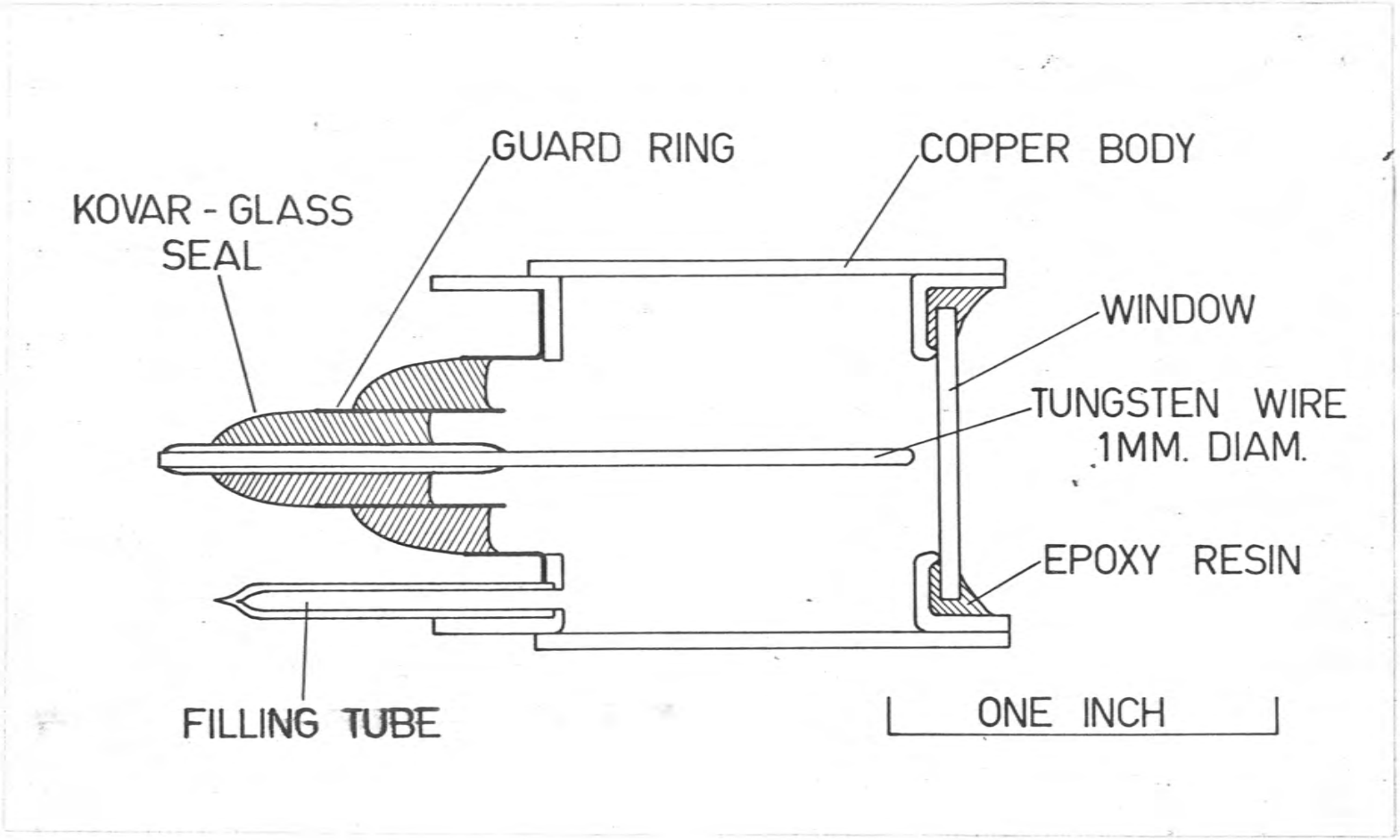

Figure 14. Cross-section of an ion chamber showing the method of construction.

After the assembled body had been cleaned the window was attached using cold setting epoxy resin. When set this resin provides a high-vacuum seal which can stand a wide range of temperatures (up to 200°C). Silver chloride has been used (Friedman et al. 1958), to obtain a seal which can withstand large temperature variations, but it is more difficult to use than epoxy resin and cannot be applied directly to copper. Not all epoxy resins have good adhesive properties, and after some experimenting it was found that Araldite AV100 was the most satisfactory. Careful preparation of the copper surface is necessary, the best treatment being cleaning and roughening with emery paper followed by cleaning with chloroform. The windows used, and their transmission limits (wavelengths at which the transmission was about 10%), are shown in Table 5.

TABLE 5 : Windows used on the Ion Chambers

Material	Form	Thickness	Transmission limit
lithium fluoride	cleaved crystal	1.5 mm	1050Å
calcium fluoride	cleaved crystal	1.5	1225
barium fluoride	cleaved crystal	1.5	1355
sapphire	polished plate	0.5	1425
quartz	polished plate	1.6	1570

When the chambers had been filled (§3.3) and tested leads were attached to the wire, guard ring, and body, and

Figure 15. Photograph of two ion chambers. The guard-ring seal and filling tube can be seen on the chamber which has not been potted.

the back of the chamber was potted in synthetic rubber, to protect the seal and support the leads. A 47 kΩ resistor, connected in series with the lead to the body, was also included in the potting, to provide protection against short circuits when several chambers were supplied from the same voltage supply. Figure 15 shows two completed ion chambers.

Acceleration and vibration during the burning stage of the flight of a HAD rocket may reach 70 g and 10 g respectively, so before the first flight an ion chamber was tested at the Weapons Research Establishment. It was subjected to an acceleration of 100 g in three directions and a vibration of 10 g at frequencies from 20 to 2,000 cps, and was found to be undamaged. The survival, in working condition, of one of the chambers from each of the flights HAD 302 and HAD 304 also demonstrates their ability to withstand not only the acceleration at take-off but also at impact. (The windows of the other ion chambers were smashed at impact).

The various combinations of window and filling gas which have been studied are listed in Table 6, with the limits of the spectral response in each case.

3.3 Filling the Ion Chambers

3.3.1 The Vacuum system.

Figure 16 shows the vacuum system used for evacuating and filling the ion chambers. A 2 in. fractionating oil diffusion

TABLE 6 : Ultra-violet Ion Chambers

Window	Filling Gas	Spectral Response
LiF	ethyl chloride	1050 - 1130 Å
	ethyl bromide	1050 - 1200
	carbon disulphide	1050 - 1240
	acetone	1050 - 1290
	nitric oxide	1050 - 1340
CaF_2	acetone	1220 - 1290
	ethyl iodide	1220 - 1330
	nitric oxide	1220 - 1340
	benzene	1220 - 1340
BaF_2	toluene	1350 - 1410
	p-xylene	1350 - 1470
sapphire	p-xylene	1420 - 1470
	mesitylene	1420 - 1480
quartz	triethyl amine	1560 - 1660

pump, backed by a 50 l sec^{-1} ballasted rotary pump, was used. Above the diffusion pump were a baffle valve and a stainless steel liquid air trap. An ionization gauge was used to measure the pressure in the trap. The manifold to which the ion chambers were attached was separated from the trap by a butterfly valve. Double O-ring seals were used to seal the filling tubes of the ion chambers into the manifold, thus allowing the chambers to be removed and replaced very easily.

Figure 16. The vacuum system used for evacuating and filling the ion chambers. The manifold to which the ion chambers were connected is on the left.

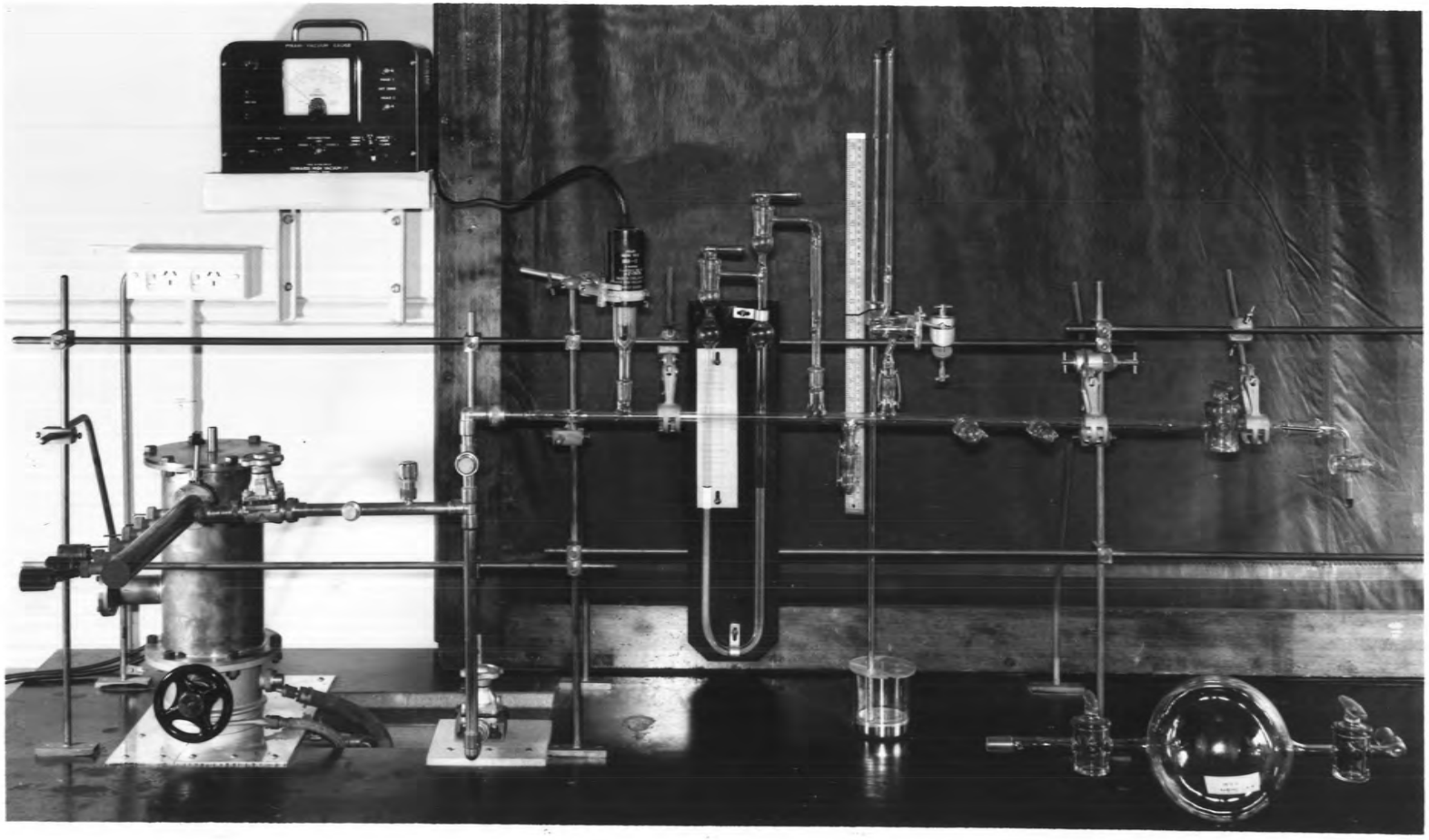

The gas handling section was connected to the manifold and consisted of a length of glass tubing to which were joined glass sockets for attaching pressure gauges, glass flasks, and liquid containers. The pressure gauges were (1) a Pirani gauge (1 to 10^{-4} torr), (2) an oil manometer (1 to 20 torr), and (3) a mercury barometer (5 to 760 torr). The oil manometer, which was used for measuring the filling pressures in the ion chambers, was filled with Apiezon C oil and was calibrated by measuring the density of the oil. The mercury manometer, which was normally shut off from the system, was used for measuring filling pressures in the proportional counter (Chapter 7).

The oil manometer was not entirely satisfactory since the oil absorbed to some extent a number of the filling gases used, and the manometer had to be pumped for about a day to remove them. However, it does provide a simple, accurate, means of measuring pressure, which is independent of the nature of the gas.

3.3.2 Filling Procedure.

The chambers to be filled were evacuated, usually for a period of several days, until the pressure was less than 10^{-6} torr. A mass spectrometer (AEI type MS10) was then used to test for any small leaks.

Nitric oxide was introduced into the system from a glass flask fitted with taps and cones, while the other fillings,

which were liquids under ordinary conditions, were introduced from a small glass phial holding about 5 ml of liquid. Since the phial contained air as well as the liquid it was necessary to pump away some of the liquid with the rotary pump before introducing the vapour into the ion chambers. The filling pressures were about 15 torr for most of the filling gases, but were lower for some of the fillings, which had low vapour pressures. The lowest pressure used was 3 torr, in the case of p-xylene and mesitylene. It is undesirable for the filling pressure to be close to the saturated vapour pressure at room temperature, since this can lead to variation in the gas gain characteristic with temperature (§3.10), and thus to errors in calibration.

Provided they have been annealed, the copper filling tubes can be pinched off to give a vacuum tight seal merely by applying sufficient pressure to them, since a cold weld is formed. Experiments with various tools showed that an ordinary pair of end cutting nippers was quite satisfactory for sealing the tubes. No leak in the seal could be detected with the mass spectrometer. The seal was protected by covering it with soft solder which was applied by dipping, since it was found that placing a hot soldering iron on the weld sometimes caused it to open.

3.3.3 Filling Gases.

Of the liquids used, the acetone and carbon disulphide

were both AR grade, the acetone stated to be 99.5% pure.

The nitric oxide was obtained from a cylinder (purity quoted as at least 99.0%), and then further purified by passing it over silica gel cooled to -80°C. This has been shown by Hughes (1961) to be as effective as many fractional distillations for removing all likely impurities except nitrogen. The procedure was to connect a 1 l glass flask to two U-tubes filled with silica gel cooled in a slush bath. After flushing the U-tubes and flask with argon, nitric oxide from the cylinder was passed through until the gas in the flask was quite colourless, and then the taps on the flask were closed. The only observed impurity was nitrous oxide (see §3.7).

3.4 Monochromators and Light Sources used in testing the Ion Chambers.

3.4.1 Monochromators

Two vacuum monochromators were used in carrying out measurements requiring dispersed radiation, both made by the McPherson Instrument Corporation. The first, which had a ½ m radius of curvature grating in the Seya-Namioka mounting, was used for almost all the measurements. The second, which had a 1 m radius of curvature grating in a normal incidence mounting was not available till most of the work was completed and was used for only a few of the tests. The ½ m instrument had a grating with 600 lines mm^{-1}, giving a dispersion of

30μ Å^{-1} at the exit slit. Two gratings were available for the 1 m instrument, one with 600 lines mm^{-1} giving a dispersion of 60μ Å^{-1} and the other with 1200 lines mm^{-1} giving a dispersion of 120μ Å^{-1}. Considerably greater intensity in the exit beam was available when using the 1 m instrument because of the larger grating area. Both instruments were equipped with wavelength counters and electrically driven scanning mechanisms. The wavelength scales were checked periodically using a sodium vapour lamp, and were also checked at Lyman-α each time a measurement was made. They were estimated to be accurate to $\pm$ 0.25Å.

3.4.2 Light Sources

The light source used with the monochromators was a McPherson discharge lamp which had a water-cooled glass capillary, a water-cooled earthed electrode, and an air-cooled high tension electrode. It was operated without a window between the lamp and the entrance slit so that gas from a cylinder continuously flowed into the lamp and then leaked out through the entrance slit, to be pumped away by the pumps in the monochromator.

The power supply used with the lamp could be operated in two ways. The voltage from a 15 kV transformer was either applied directly to the lamp, (A.C. mode of operation) or was used to charge, through a resistance, a set of condensors which then discharged through a spark gap and into

the lamp (spark mode of operation). In the spark mode several discharges of the condenser occurred during each half cycle of the 50 cps voltage supplied by the transformer. The maximum average current available from the supply was 120 mA.

Several gases emit radiation in the range 1000 to 1700Å when excited in a discharge lamp, the most useful of which are hydrogen and argon. The most intense radiation is obtained using hydrogen, which provides a large number of closely spaced lines in the region 1000 to 1650Å. These lines belong to overlapping bands of the Lyman ($B\ ^1\Sigma_u^+ \rightarrow X\ ^1\Sigma_g^+$) and Werner ($C\ ^1\Pi_u \rightarrow X\ ^1\Sigma_g^+$) systems. In addition, there is a weak continuum underlying the lines, and the dissociation continuum ($H_2(^3\Sigma_g^+) \rightarrow H_2\ (^3\Sigma_u^+) + h\nu \rightarrow H + H$) which extends to wavelengths longer than 1600Å. The nature of the spectrum was not particularly sensitive to the discharge conditions, but the continuum was found to be enhanced relative to the lines by using the spark mode, and as high a pressure as possible. On the $\frac{1}{2}$ m instrument the highest pressure obtainable in the lamp was 8 torr, when the pressure in the main chamber was 4×10^{-4} torr. Figure 17 shows the hydrogen spectrum under these conditions, as recorded by the sodium salicylate - photomultiplier combination, with a bandwidth of 2Å. The operating conditions were R = 160 kΩ, C = 0.0075μF, average current 120 mA, spark gap voltage 9 kV, and discharge

frequency 1000 cps. The Lyman-α line is also emitted by the hydrogen discharge, its intensity relative to the molecular spectrum increasing as the pressure in the lamp decreases. When this line was required a pressure of 1 torr and the A.C. mode were used.

Argon emits a continuum extending from 1050 to 1450Å with maximum intensity at 1250Å, but a pressure of 100 to 300 torr is required in the lamp and this could be obtained only with the 1 m instrument, which was fitted with differential pumping equipment. Thus full use could not be made of the argon continuum which is more suitable for obtaining the spectral responses of ion chambers than the hydrogen spectrum. The lamp must be excited in the spark mode to obtain the continuum, which is shown in Figure 17. The operating conditions were similar to those given above for the hydrogen spectrum.

3.5 The Portable Light Source

A portable hydrogen discharge lamp with a lithium fluoride window was constructed for carrying out tests on the ion chambers in which dispersed radiation was not required. A drawing of the lamp is shown in Figure 18. It was excited using a simple R.F. oscillator, coupled to the lamp with a length of coaxial cable and two metal clips placed round the lamp. The lamp was evacuated and filled on the vacuum system used for the ion chambers, a filling of

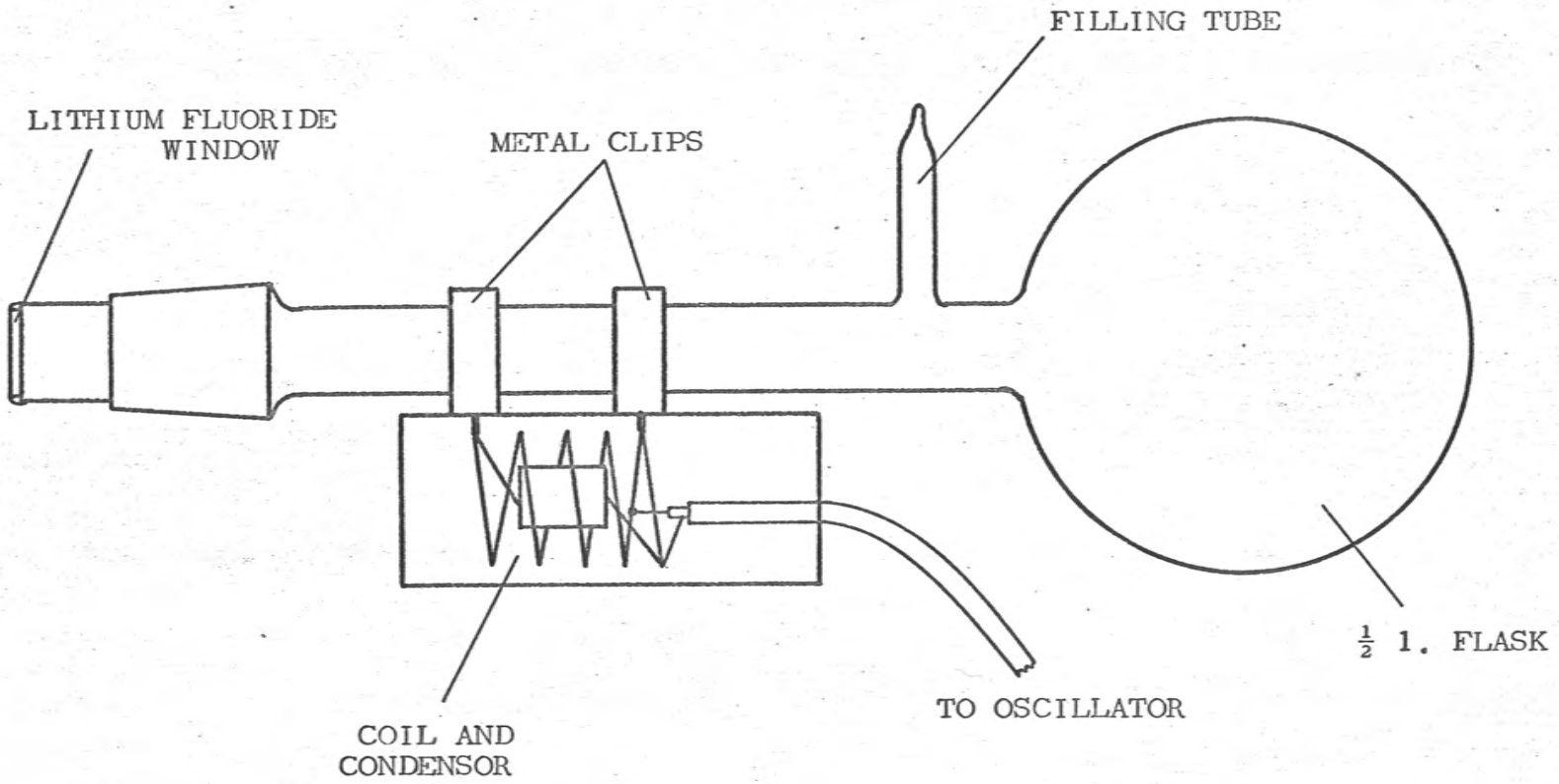

Figure 18. The portable hydrogen lamp.

hydrogen at a pressure of about 0.1 torr being used. This pressure was found to give the maximum light intensity in the 1050 to 1350Å range. The spectrum of the light from the lamp was recorded using the monochromator and was found to be similar to that shown in Figure 17.

Figure 19 shows the lamp and oscillator being used to test the response of an ion chamber. A mounting was made which held both the lamp and ion chamber. Since the vacuum ultra-violet radiation is strongly absorbed in the air (1mm of air will attenuate 1450Å radiation by a factor of 3000), the mounting was constructed so that the space between the lamp and ion chamber could be flushed with nitrogen. Ordinary cylinder nitrogen is unsuitable because it contains considerable amounts of oxygen and water vapour, but a grade called "Oxygen-free nitrogen" was found to be satisfactory. It contains less than 10 ppm of oxygen and less than 60 ppm of water vapour, which produce negligible absorption of the ultra-violet radiation over a path length of 1 cm.

An extra attachment for the lamp mounting was made which enabled the lamp to be used for checking the sensitivity of ion chambers mounted in a rocket. In this way tests could be carried out at Woomera just before the launching of the rocket.

3.6 Determination of the Spectral Response and Absolute Efficiency of the Ion Chambers.

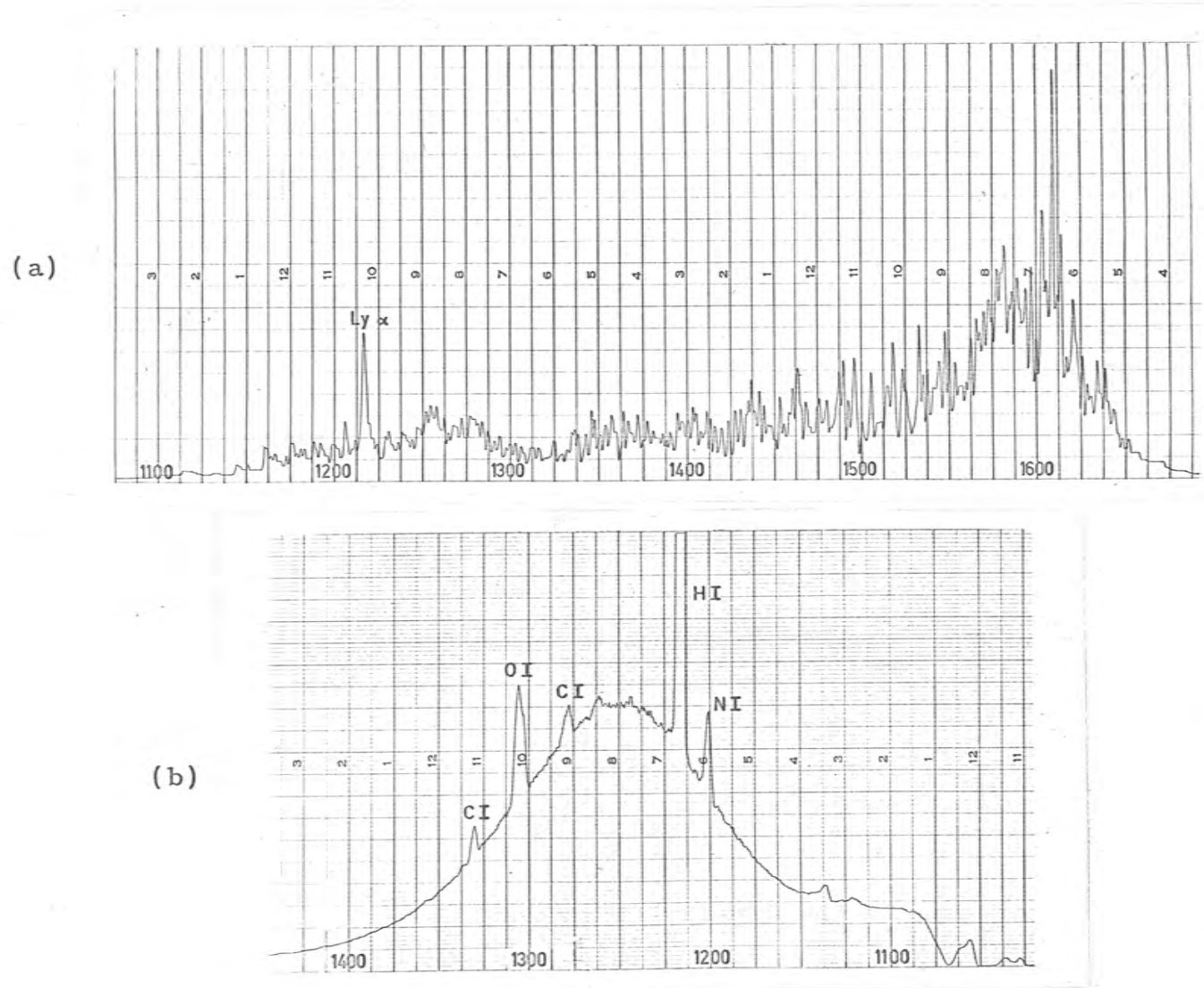

Figure 17. Spectra of the two light sources used (a) hydrogen and (b) argon. The lines in the argon spectrum due to impurities are identified in the figure. For operating conditions see text. Spectral bandwidths : hydrogen 2Å, argon 3Å.

Figure 19. Arrangement for testing ion chambers with the portable lamp.

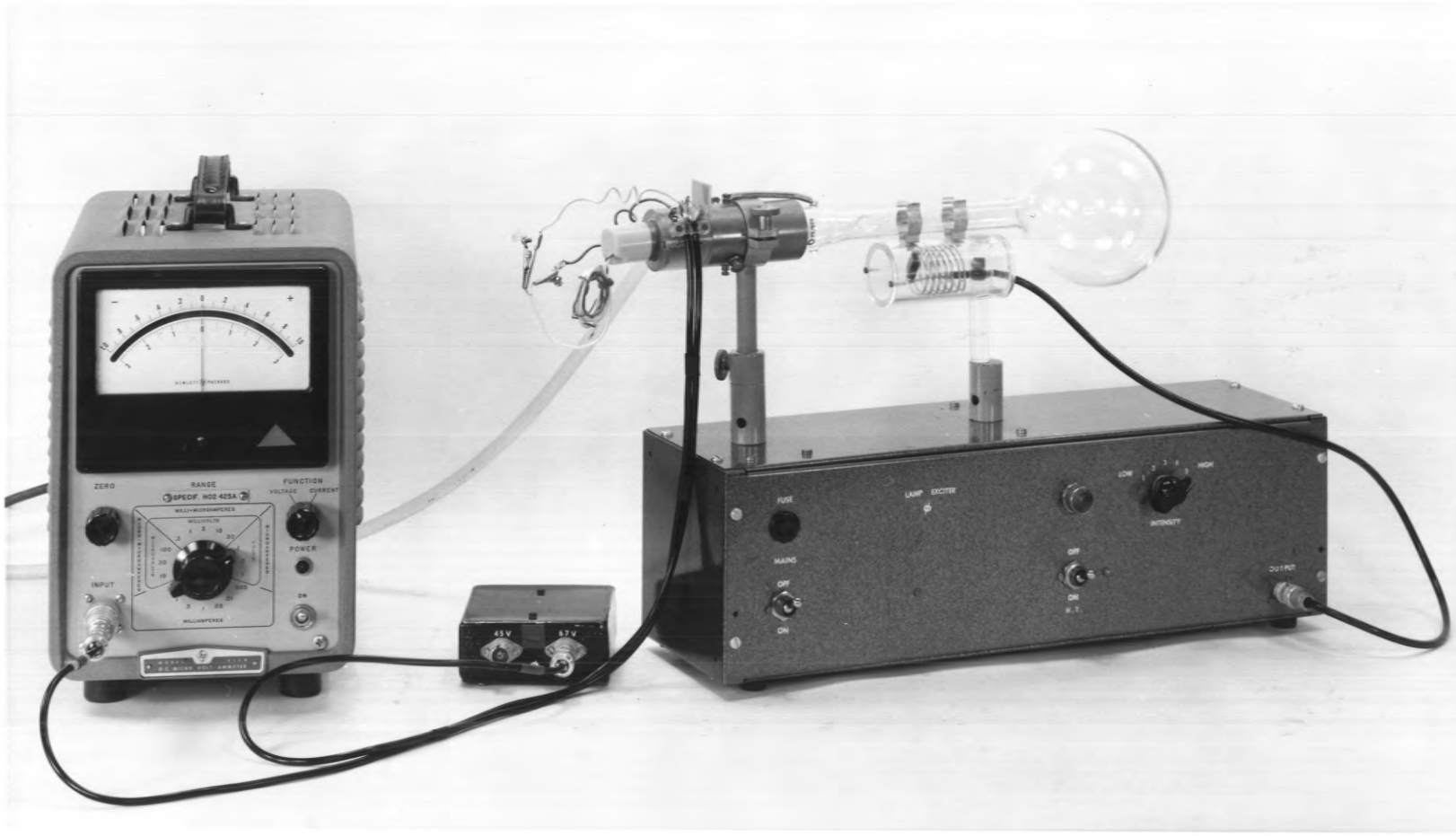
ZERO
RANGE
SPECIF. HO2 425A
FUNCTION
VOLTAGE
CURRENT
POWER
INPUT
ON
45 V
67 V
FUSE
LAMP EXCITER
LOW
HIGH
INTENSITY
MAINS
OFF
ON
OUTPUT
H.T.

3.6.1 Introduction

The sensitivities of the ion chambers used in the present work were measured in terms of the quantum efficiency, defined as the number of electrons collected at the anode of the chamber per photon incident on the window*. The quantum efficiency will be the product of (1) the transmission of the window, (2) the fraction of the radiation absorbed in the filling gas, and (3) the photoionization efficiency (p.53) of the filling gas.

Determination of the quantum efficiency at a particular wavelength involves the measurement of the current from the ion chamber when it is exposed to a monochromatic beam, of known intensity, at that wavelength. Absolute measurement of the intensity of dispersed vacuum ultra-violet radiation is difficult because of the low intensities available. Probably the most accurate method (Sampson 1964, Metzger and Cook 1965) is to absorb the beam from the monochromator in one of the inert gases and measure the ion current, making use of the fact that the photoionization efficiency of these gases is unity, but this method is applicable only at wavelengths shorter than 1022Å, the photoionization threshold of xenon. Radiation thermopiles, calibrated by exposing them to

---

*The current collected varies with the collecting voltage (see §3.10) but there is a range of voltages in the "plateau" region where the current is almost independent of the voltage, and the collection efficiency is close to 100%. In the present work the quantum efficiencies were measured with a collecting voltage of 45V, which lay in the plateau region for all the chambers used.

lamps in the visible region, have been used by Packer and Lock (1951), Watanabe and Inn (1953), and Knapp and Smith (1964) for absolute measurements at wavelengths longer than 1022Å. The assumption must be made that the thermopile is equally as effective in absorbing radiation in the vacuum ultra-violet region as in the visible*. An attempt was made during the present work to use a thermopile (Eppley, Bi - Ag, 12 junction) to measure the intensity of the monochromator beam, but it was unsuccessful because of the low sensitivity of the thermopile ($0.06V\ W^{-1}\ cm^{2}$).

The usual method of making the absolute measurement when a thermopile is not available is by means of a parallel plate ion chamber filled with a gas, the photoionization efficiency of which has been previously determined. The most convenient gas is nitric oxide, the photoionization efficiency of which has been determined by Watanabe and Matsunaga (1961), for wavelengths between 1050 and 1350Å. This method was adopted in the present work, as described in §3.6.3.

The variation, with wavelength, of the quantum efficiency of the ion chambers used in the present work, was determined by comparing their response with that of a photomultiplier detecting the fluorescent radiation from sodium salicylate, it being assumed that the latter combination gave a response which was proportional to the number of photons per unit time

---

*The thermopile could be calibrated at some wavelength below 1022Å against an ion chamber containing an inert gas, but this method does not seem to have been used as yet.

incident on the sodium salicylate, and independent of the wavelength of the photons. Of the fluorescent materials which have been investigated, sodium salicylate would appear to be the one which most nearly satisfies this condition, although the results obtained by different workers are not in complete agreement. Watanabe and Inn (1953) and Allison et al. (1964a) have reported that the quantum efficiency (number of fluorescent photons per incident ultra-violet photon) in the range 1000 to 1700Å was constant to within ±5% and showed no systematic variation, while Sampson (1964), and Knapp and Smith (1964), find a drop in quantum efficiency of approximately 20% at about 1300Å, with a weak maximum at about 1500Å. Exposure to the residual gases in a vacuum monochromator causes a gradual decrease in the quantum efficiency (Sampson 1964, Knapp and Smith 1964), the decrease being larger at shorter wavelengths, whereas exposure to dry air, or the vacuum produced by an ion pump, has no effect (Hammann 1958, Allison et al. 1964b, Nygaard 1964). It may be concluded that the quantum efficiency of sodium salicylate is constant to at least ±10% over the range 1000 to 1700Å, provided that it has not been in the monochromator for more than several days. In the present work fresh salicylate layers were always used and no corrections were made for the possible variation of quantum efficiency with wavelength.

3.6.2 Spectral Response.

To record the spectral response of an ion chamber a wire grid, coated with sodium salicylate, was placed in the exit beam of the monochromator, in such a way that the fluorescent radiation could be detected by a photomultiplier (Ditchburn 1962). The radiation which passed through the grid was allowed to fall on the window of the ion chamber, and the ratio of the current from the chamber, to the current from the photomultiplier, was then recorded automatically as the wavelength was varied.

A diagram of the experimental arrangement is shown in Figure 20, and a photograph of the apparatus in Figure 21. The wire grid (1.8mm spacing) was contained in a chamber with a side arm in which a polished perspex light pipe was placed. Sodium salicylate was coated onto the grid by spraying it with a concentrated solution of salicylate in methyl alcohol. The photomultiplier, type 9514S, had a spectral response which closely matched the spectral distribution of the salicylate fluorescent radiation. A spun aluminium can was used to enclose the photomultiplier and the dynode resistor chain. Since the light comes in short flashes, about 1μ sec long, when the lamp is excited in the spark mode, condensers must be placed across the last few dynodes of the photomultiplier to ensure linearity of response. The photomultiplier itself was wrapped in a shield connected to the cathode, to avoid

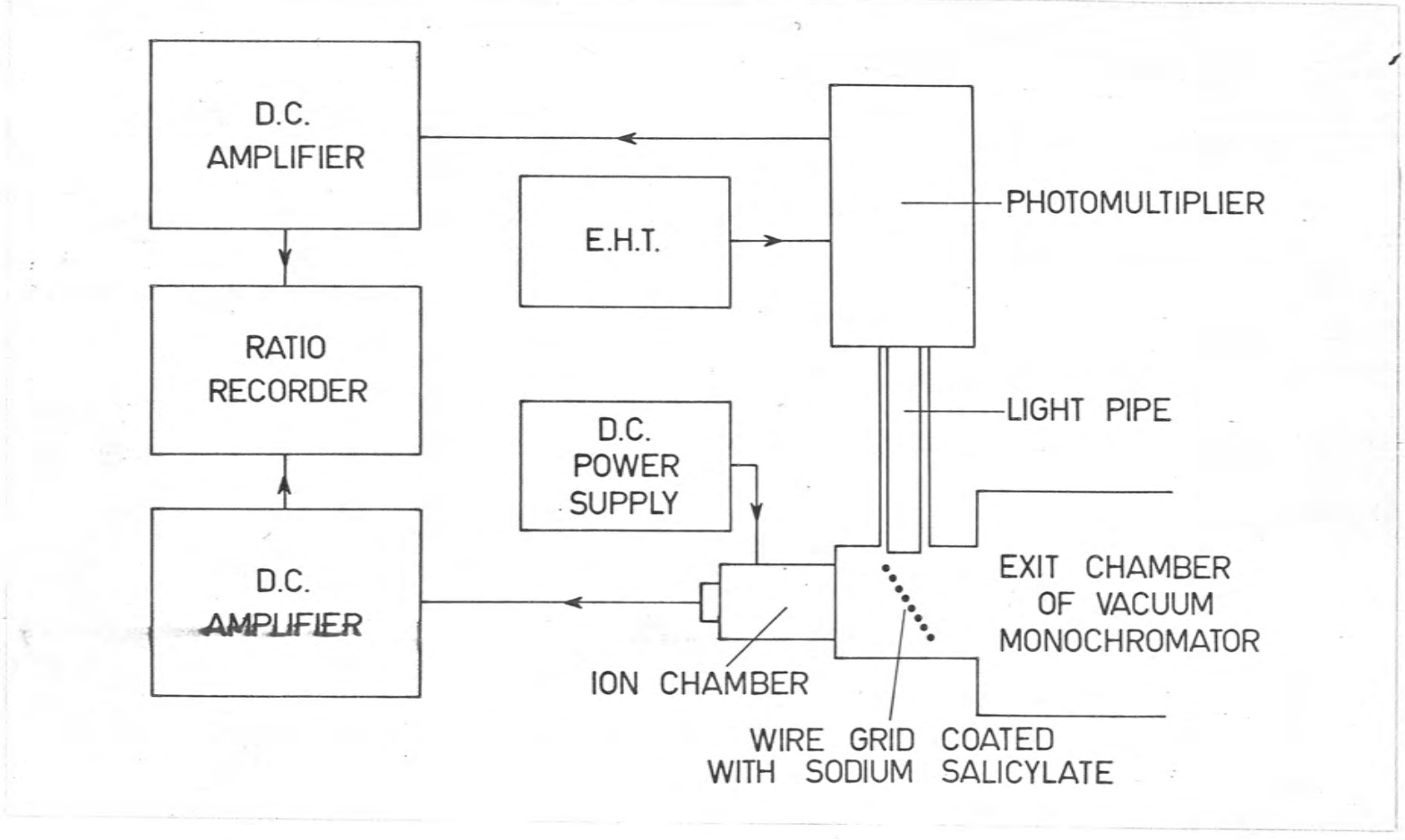

Figure 20. Experimental arrangement for measuring the spectral response of an ion chamber.

Figure 21. The $\frac{1}{2}$ m monochromator and apparatus used for recording the spectral response of an ion chamber.

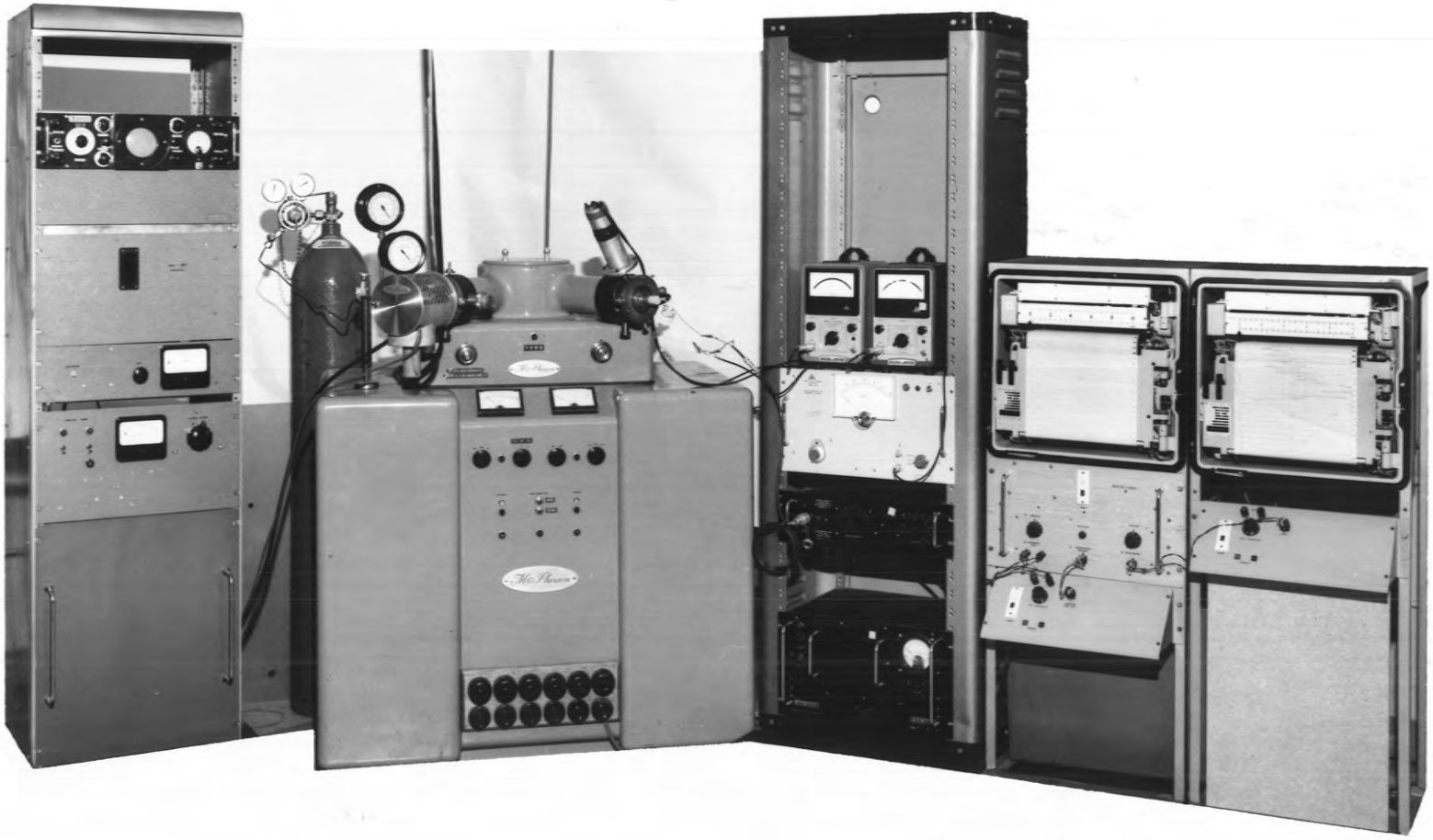

the increase in dark current which results from the close proximity of an earthed mounting (de Valence 1955).

The ion chamber was electrically insulated from the chamber containing the grid so that the collecting voltage could be applied to the case. Currents from the chambers when they were operated at 45V were in the range 10^{-11} to 10^{-12} A, so the voltage was increased to obtain gas gains in the range 30 to 300 (see §3.10).

The currents from the photomultiplier and ion chamber were both amplified by D.C. amplifiers, and then the ratio of the signals was formed by means of a servo system and recorded on a chart recorder. There is always a certain amount of scattered visible light emerging from the exit slit of the monochromator, and it will be detected by the photomultiplier. However, the intensity of the scattered light does not vary much with the wavelength setting of the monochromator, so it can be compensated for by a small adjustment of the zero on the amplifier used with the photomultiplier. The level of the scattered light was determined by means of a filter holder, in the chamber containing the grid, which enabled a lithium fluoride window to be moved into the beam. The signal obtained from the photomultiplier with the window in the beam and the monochromator set to 1000Å (below the transmission limit of lithium fluoride) was due to the scattered light. It was

always less than 1% in the present work.

3.6.3 Absolute Efficiency.

The absolute efficiencies of the ion chambers were determined by first calibrating one lithium fluoride-nitric oxide chamber at Lyman-α, and then using this chamber to calibrate the others. The lithium fluoride-nitric oxide chamber was calibrated by using a parallel plate ion chamber filled with nitric oxide, and assuming that the photoionization efficiency of nitric oxide at Lyman-α is 81% (Watanabe and Matsunaga 1961).

Figures 22 and 23 show the experimental arrangement. The exit beam from the monochromator passed through the grid coated with sodium salicylate and then entered the ion chamber through a 1 cm diam. lithium fluoride window, which was fixed in an aluminium mounting electrically insulated from the ion chamber mounting plate. The copper chamber was 6 cm diam. and 17 cm long, and contained two parallel stainless steel plates mounted on teflon insulators. Radiation not absorbed in the chamber struck a layer of sodium salicylate on a glass plate at the end of the chamber and excited fluorescent radiation which was detected by a photomultiplier mounted behind the plate. The stainless steel plates touched the glass plate at one end and protruded past the window at the other, so there was a very small probability of an ion produced in the chamber not being collected. In addition the window mounting was connected electrically to the plate

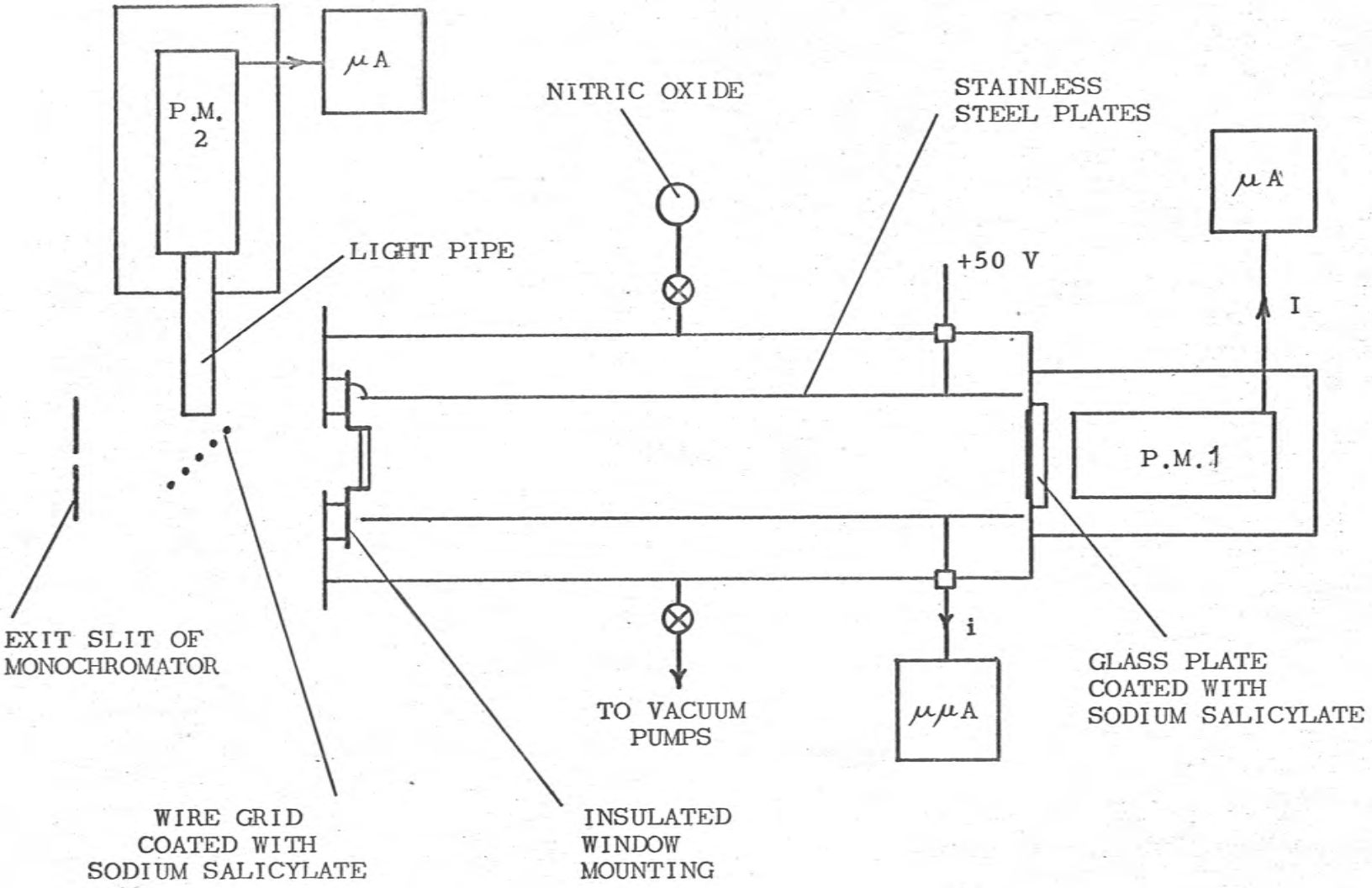

Figure 22. Diagram of the parallel plate ion chamber used for determining the absolute efficiencies of the small ion chambers.

Figure 23. The parallel plate ion chamber used for determining the absolute efficiency of an ion chamber.

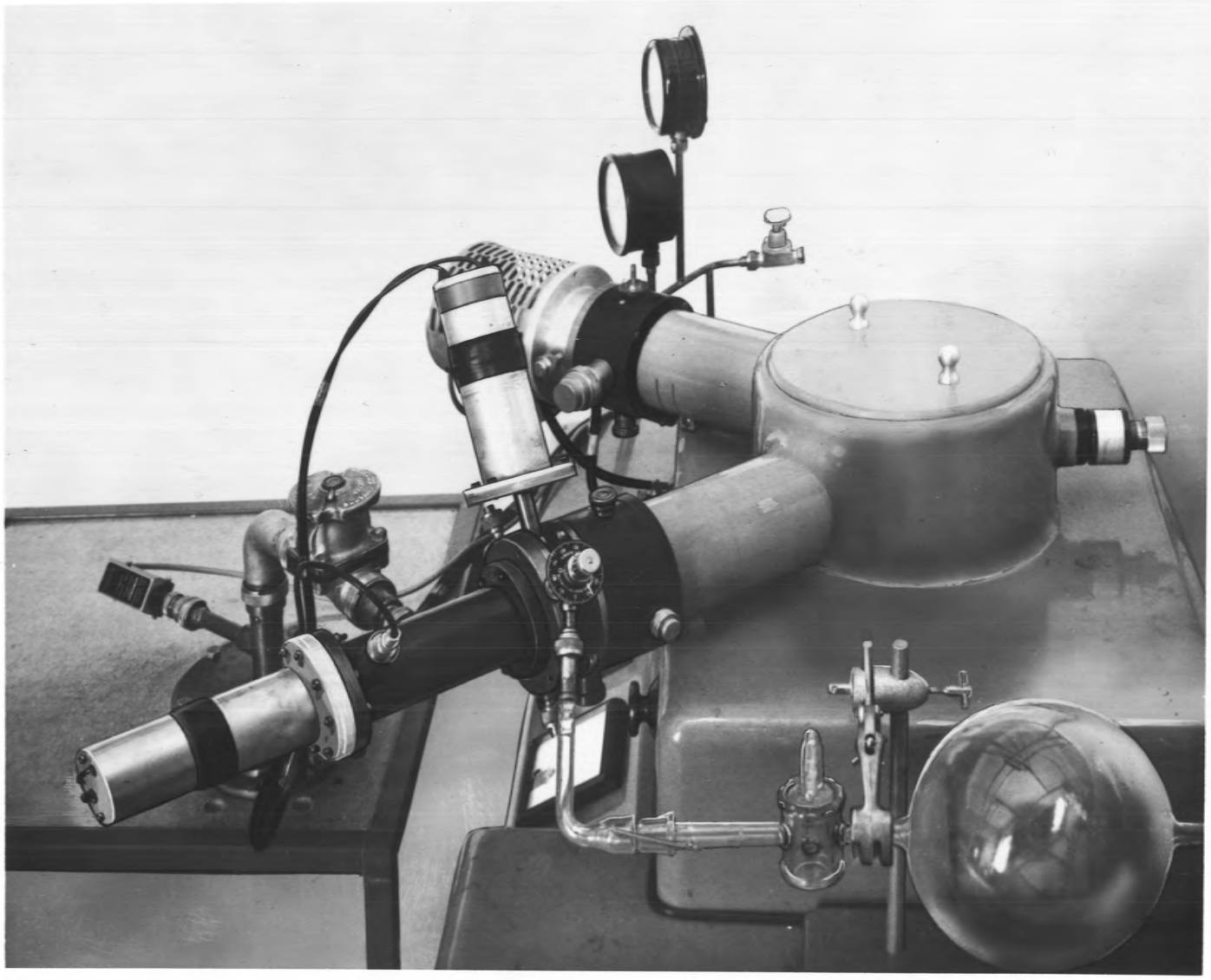

to which the positive voltage was applied, in order to produce a collecting field for the ions in the space near the window. A portable vacuum system was used to evacuate the chamber to a pressure lower than 10^{-5} torr, and the nitric oxide, purified as described in §3.3.3, was admitted through a needle valve.

The procedure was as follows. The monochromator lamp was excited using the A.C. discharge through hydrogen, and the monochromator was set to Lyman-α with a spectral bandwidth of 2Å. The currents from the photomultipliers at the end of the chamber (P.M. 1) and at the end of the light pipe (P.M. 2) were first noted, and then nitric oxide admitted to the chamber at a series of pressures in the range 0.3 to 10 torr. At each pressure the collecting voltage on the ion chamber was adjusted till a plateau was obtained, then the current I given by P.M. 1 and the ion current i were noted. The current from P.M. 2 was used to correct I and i for any variations in the beam intensity, which were never more than 5%. The currents I and i were then plotted as shown in Figure 24.

By using a number of gas pressures the ion collection efficiency can be checked. If all the ions are being collected, the decrease in I when gas is admitted to the chamber will be proportional to the increase in i, and a straight line graph will result (Figure 24). As the pressure was increased to about 10 torr I decreased to some small value

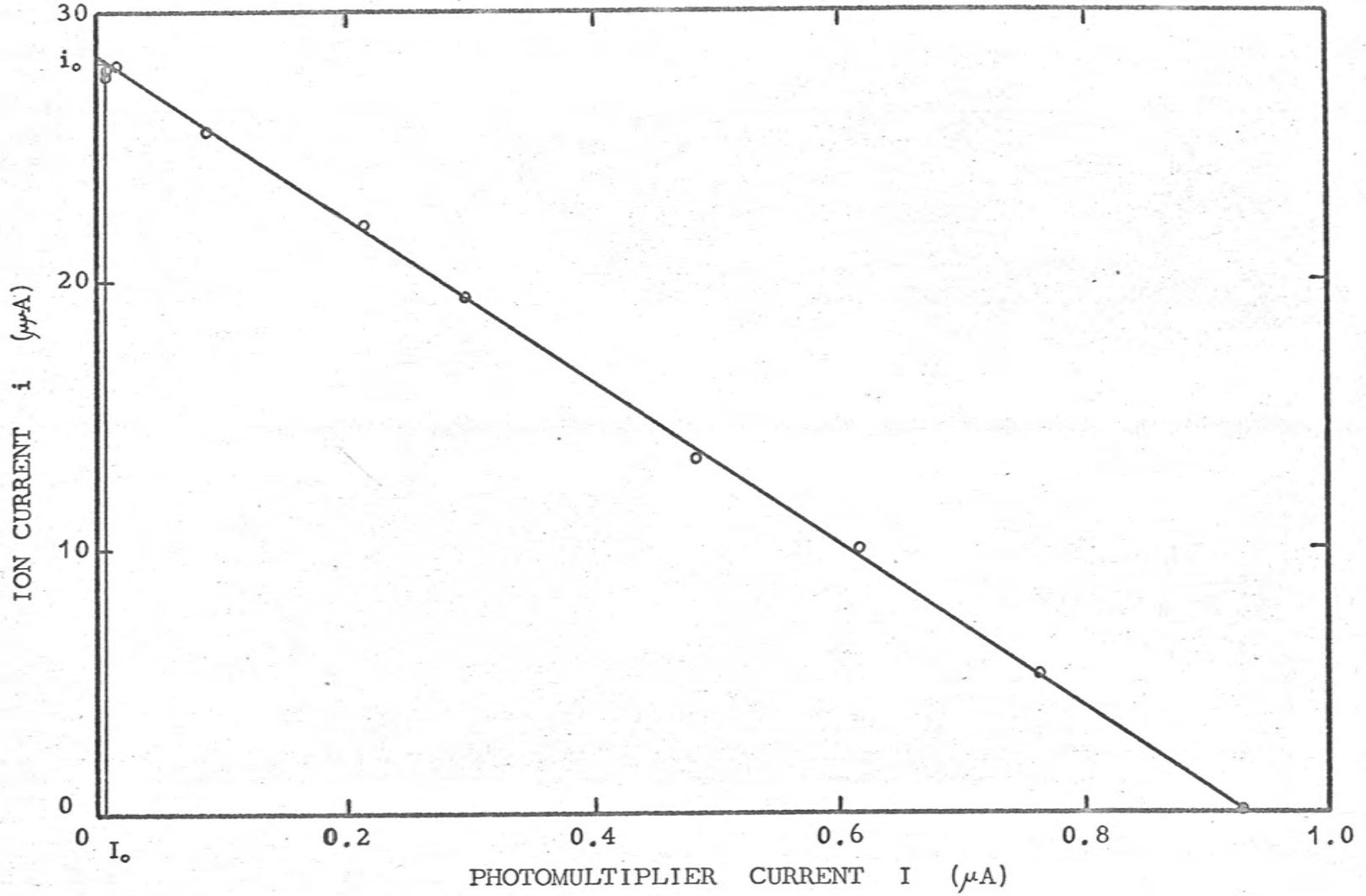

Figure 24. A plot of ion current i against photomultiplier current I for the parallel plate ion chamber shown in Figure 22.

I_o representing the scattered visible light in the monochromator beam. A straight line was drawn through the experimental points, and from the line i_o, the value of i corresponding to I_o, was determined (Figure 24). This represented the ion current which would have been obtained if all the Lyman-α photons emerging from the window had been absorbed and the ions collected. If all the photons had produced an ion the current would have been $i_o/0.81$, using the above-mentioned photoionization efficiency of 81%.

After the measurements with the parallel plate ion chamber had been completed it was removed, leaving the window in place, and replaced by a lithium fluoride-nitric oxide chamber. The space between the window and the chamber was evacuated using a rotary pump. The current i_L given by this chamber, operated at 45V, was measured and corrected if necessary for any variations in the current from P.M. 2. The quantum efficiency Q_L, at Lyman-α, of this chamber was then calculated from

$$Q_L = \frac{0.81\ i_L}{i_o}$$

The spectral response curves for the various chambers, obtained as described in §3.6.2, had different quantum efficiency scales, since each chamber was operated at a different gas gain, and the sensitivity of the chart recorder was altered for each chamber to obtain a trace which occupied

the full width of the chart. To determine the scale in each case the following procedure was adopted. After each trace had been recorded the monochromator was set to a wavelength within the sensitive range of the chamber and the ratio recorded on the chart. At the same time the actual values of the photomultiplier current I_c and the ion chamber current i_c were noted. The absolutely calibrated lithium fluoride-nitric oxide chamber was then placed in position, the monochromator set to Lyman-α, and the corresponding currents I_L and i_L noted. The mark on the chart then corresponded to a quantum efficiency of

$$\frac{i_c \, I_L \, g_L}{i_L \, I_c \, g_c} \cdot Q_L$$

where g_L and g_c were the gas gains of the lithium fluoride-nitric oxide and other chambers (measured as described in §3.10), and Q_L was as defined above. Using the mark on the chart a linear quantum efficiency scale was then constructed.

3.7 Spectral Response Curves.

Figures 25 and 26 show the variation of quantum efficiency with wavelength for the ion chambers listed in Table 6. These curves are reproductions of the chart recorder traces obtained as described in §3.6.2 using the spark discharge through hydrogen as the light source and a bandwidth of 2Å. Since the filling pressures for the present ion chambers are sufficient for almost all the radiation entering the chambers

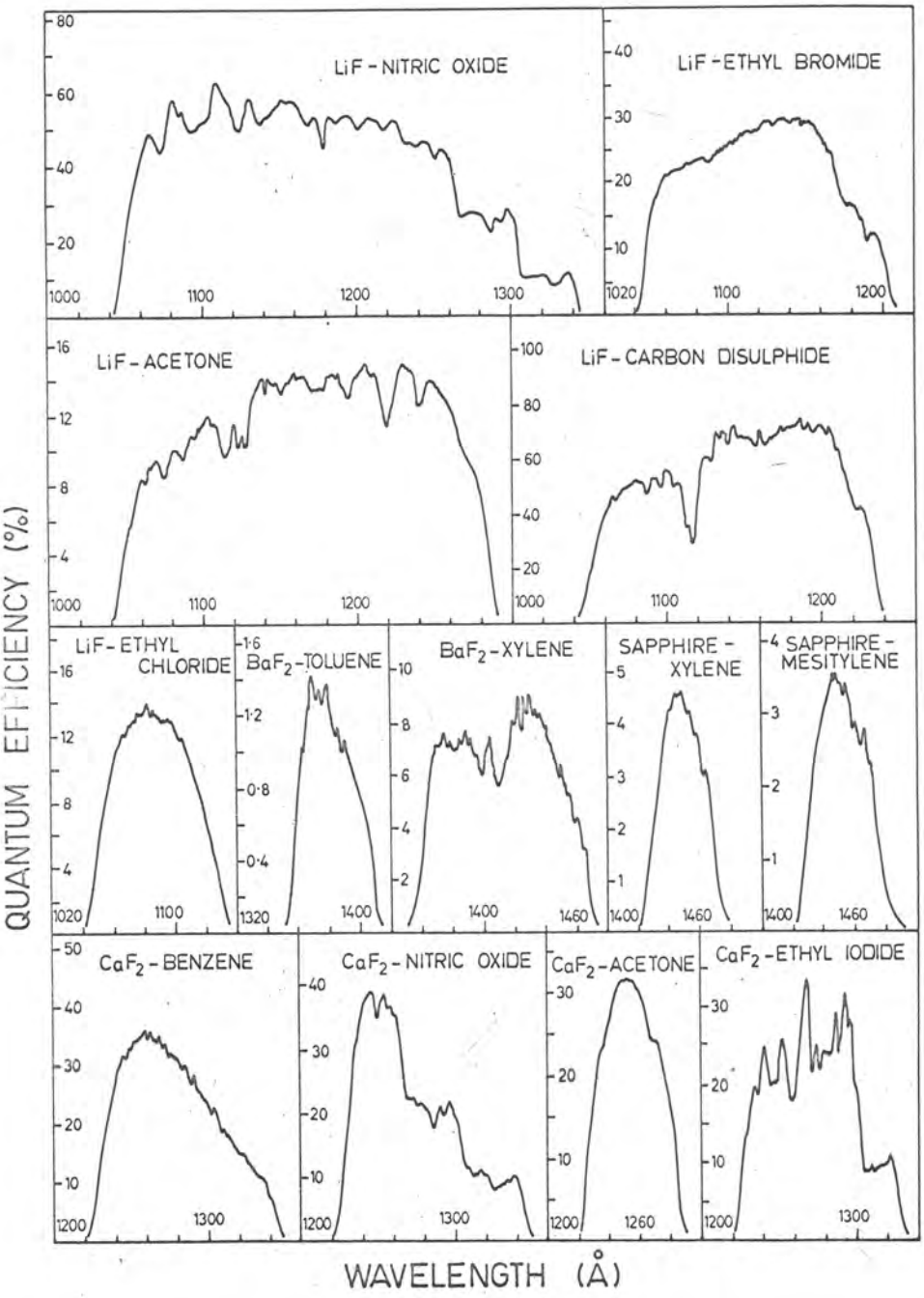

Figure 25. Spectral response curves for all the ion chambers listed in Table 6 except the quartz window one. All the wavelength scales are marked in 20 Å divisions.

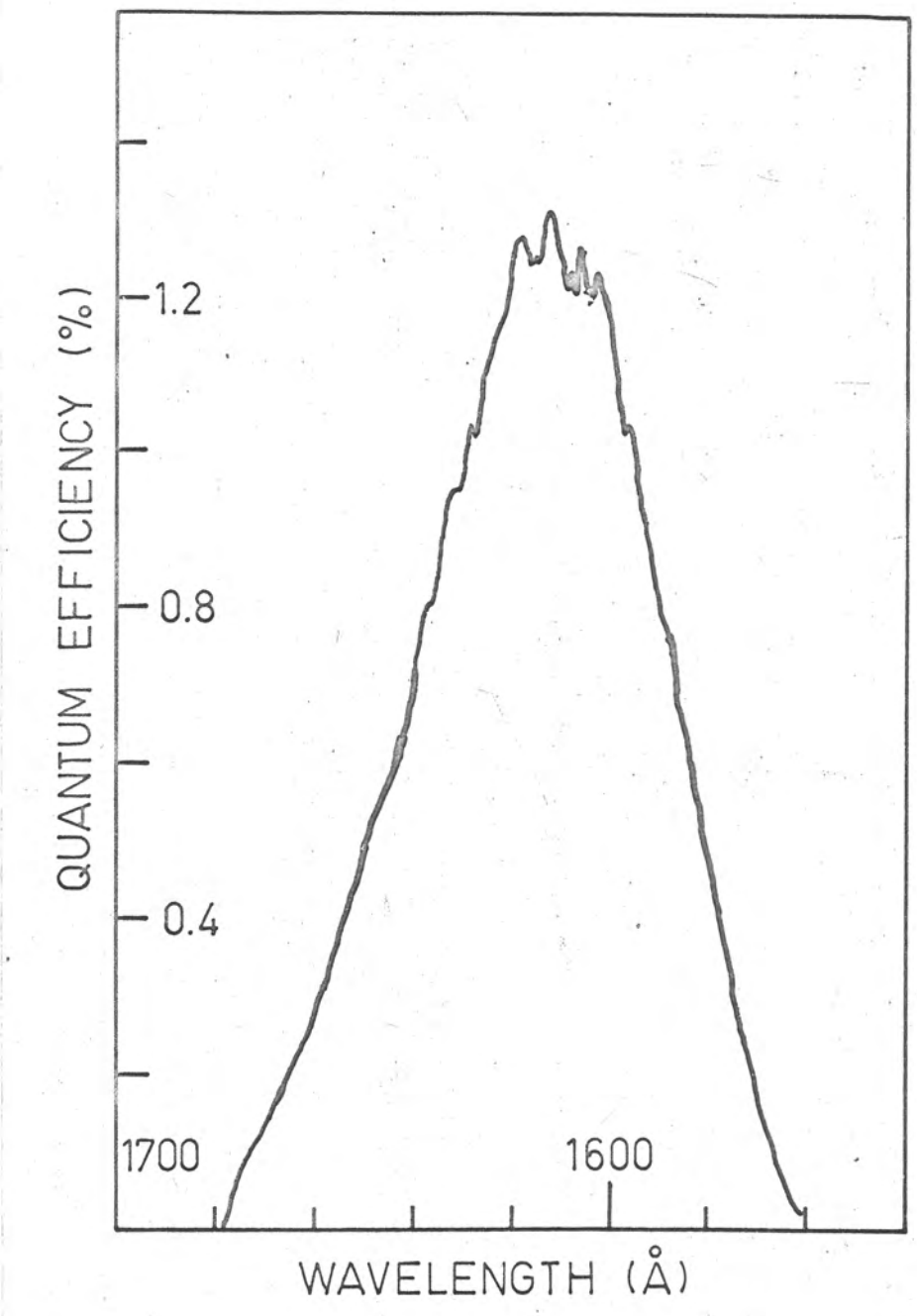

Figure 26. Spectral response curve for the quartz-triethyl amine ion chamber. The wavelength scale is marked in 20 Å divisions.

to be absorbed (see §7.4), the quantum efficiency will be equal to the product of the window transmission and the photoionization efficiency of the filling gas. Most of the very fine structure, such as that on the curve for the calcium fluoride-benzene chamber, corresponds to variations with wavelength of the intensity of the source and thus reflects inaccuracy in the ratio system, rather than variations in quantum efficiency. The fluctuations due to this cause were never more than 5% even though the beam intensity varied by as much as a factor of two over a few Angstroms. Larger fluctuations, such as those seen in the curves for the lithium fluoride-acetone and calcium fluoride-ethyl iodide chambers, represent variations in the photoionization efficiency of the filling gas.

The curve for the lithium fluoride-nitric oxide chamber follows very closely the photoionization efficiency of nitric oxide as given by Watanabe and Matsunaga (1961) and shows clearly the effects of photoionization leading to the first and second vibrationally excited levels of the nitric oxide ion, the thresholds of which lie at 1300Å and 1260Å respectively. This curve is in good agreement with that published by Kreplin et al. (1962) for a similar chamber. Both show a dip at 1177Å probably due to the presence of

nitrous oxide in the filling*. The curves for the lithium fluoride-carbon disulphide, calcium fluoride-nitric oxide and calcium fluoride-acetone chambers are similar to those given by Stober et al. (1963) for the same combinations. The sharp dip at 1117Å in the curve for the carbon disulphide chamber appears to be due to a drop in the photoionization efficiency of carbon disulphide, since it corresponds to a peak in the absorption spectrum (see §7.4). The curve for the sapphire-xylene chamber is rather smoother than that of Friedman et al. (1964), and more in agreement with the photoionization efficiency of xylene as given by Watanabe (1954).

Of the three chambers sensitive to Lyman-α the one filled with nitric oxide is the most suitable for measurements of solar radiation, since the one filled with acetone has considerably lower efficiency, and the one filled with carbon disulphide shows a rapid decrease in sensitivity when exposed to high ultra-violet fluxes (see §3.11). For a 1450Å chamber mesitylene does not seem to offer any advantages over xylene, and has the disadvantage that it is very difficult to remove completely from the vacuum system used for filling the chambers.

The long wavelength response of the ion chambers was

---

*There is a sharp peak in the absorption spectrum of nitrous oxide at 1177Å (Zelikoff et al. 1953), the absorption cross-section being larger than that of nitric oxide by a factor of about 50, and the photoionization threshold of nitrous oxide is at 962Å, so only about 0.3% of nitrous oxide is required to produce the dip seen in Figure 24.

investigated using a beam of 2537Å radiation from a high intensity monochromator (Bausch and Lomb, type 33) with a mercury lamp as the source. The intensity of the beam, as measured with a calibrated radiation thermopile, was 2.1×10^{4} erg cm^{-2} sec^{-1}, and the area was about 0.5 cm^{2}. It was found that when the wall of the chamber was negative there was no current greater than 10^{-12} A, irrespective of where the beam was directed inside the chamber. On the other hand a few of the nitric oxide chambers showed a weak response when the wall was positive and the beam was directed at the wire. Since the intensity in the beam was greater than the integrated solar intensity at wavelengths less than 2900Å*, and the currents obtained were several orders of magnitude smaller than those to be expected due to photoionization of the filling gas, it was concluded that the long wavelength response would not be significant when using these chambers to measure solar radiation. The fact that there was no detectable response below 69 km from the chambers flown in the rockets HAD 301 and HAD 304 (Chapter 5) confirmed this conclusion.

3.8 Angular response and effective aperture of the Ion Chambers.

3.8.1 Angular Response.

When the ion chambers are used in rockets for measurements of solar radiation it is necessary to know their

*There was no response at 2900Å or any longer wavelength.

Figure 27. Experimental arrangement for determining the angular response of an ion chamber.

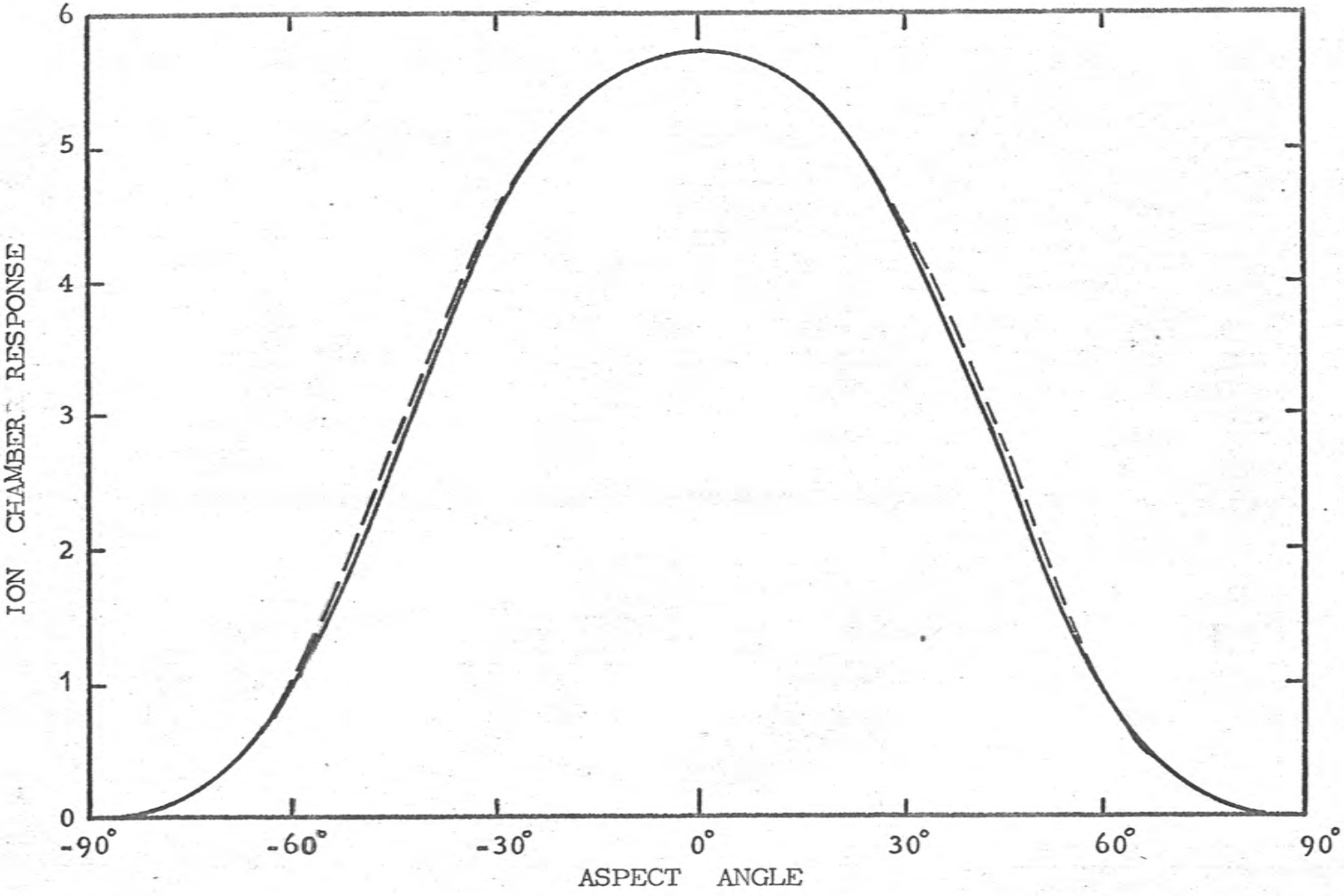

Figure 28. Angular response of one of the ion chambers flown in HAD 304. Full curve: Response obtained with the apparatus shown in Figure 27. Dashed curve: Response derived from an analysis of the signal obtained during the rocket flight (see § 5.5). The response curves have been normalized at 0°.

angular responses. Under favourable conditions these may be determined during the actual flight, making use of the roll of the rocket (see §5.5), but in case this was not possible the angular responses of the chambers used in the HAD rockets were determined before the flights.

The apparatus used is shown in Figure 27. The portable hydrogen discharge lamp described in §3.5 was mounted in the side of a chamber flushed with oxygen-free nitrogen (see §3.5), and the ion chamber was held on the end of a rotating shaft passing through the lid. Since the beam from the lamp was not strictly parallel it would not be expected that the angular response obtained in this way would be exactly the same as that obtained during the rocket flight for the same chamber. However, a comparison of the response obtained in the laboratory, with that obtained during flight, for one of the chambers flown in HAD 304 (Figure 28) shows that the laboratory response is not in error by more than 3%.

3.8.2 Effective Aperture.

The calibration of the ion chambers used in the rocket flights was carried out using the beam from the monochromator, which was considerably smaller in area than the window of the ion chamber, so it was necessary to check that the response of the chamber was constant across the window and that the epoxy resin had not caused any drop in transmission near the edge. This was done using the apparatus shown in Figure 29, by means of which a beam of radiation from the portable lamp, 0.5mm in

Figure 29. Apparatus for determining the effective aperture of an ion chamber.

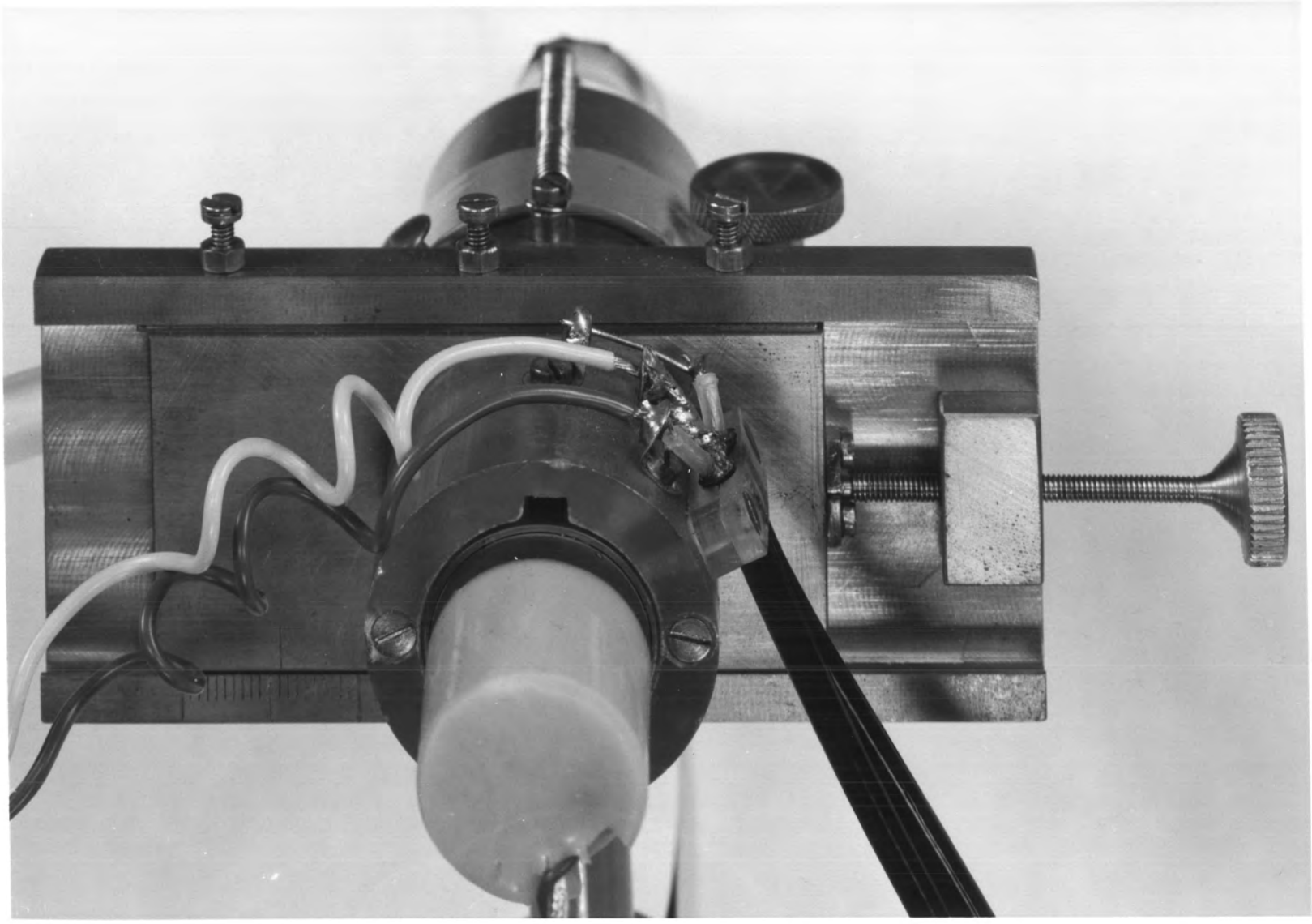

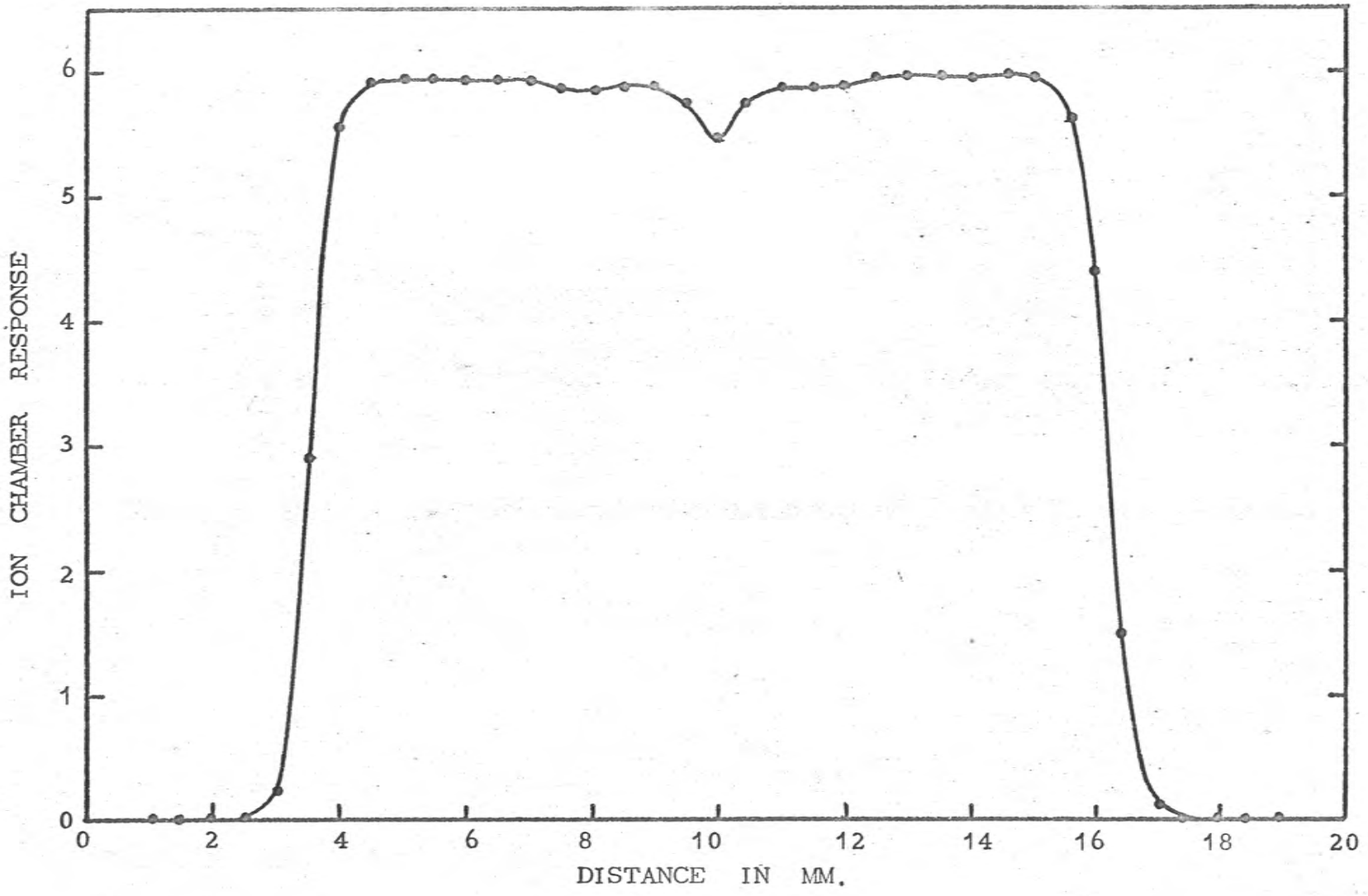

Figure 30. Variation of response when a 0.5 mm. diam. beam was scanned across the window of an ion chamber. The small drop in response in the region of the wire is insignificant since the wire occupies only 0.6% of the window area.

diameter, could be moved across the window of the chamber. It was found in all cases that the response was uniform, and that the effective aperture was 12.5mm, the diameter of the hole in the copper end piece of the chamber (Figure 14). A typical result is shown in Figure 30.

3.9 Temperature Effects.

As the ion chambers may be subjected to considerable heating during a rocket flight it is important to know the effect on the sensitivity of changes in temperature. It is known that the transmission limits of the window materials are moved to longer wavelengths as the temperature is raised. Calcium fluoride has been studied by Knudson and Kupperian (1957), while lithium fluoride, calcium fluoride, barium fluoride and sapphire have been investigated by Laufer et al. (1965), who gave transmittance curves at various temperatures for windows similar to the ones used on the present ion chambers. The photoionization threshold of the filling gas will also move to longer wavelengths as the temperature is raised due to thermal excitation of the molecules of the gas.

The apparatus shown in Figure 31 was used for raising the temperatures of ion chambers while they were mounted on the monochromator. The brass mounting plate was water-cooled to prevent heat being conducted to the photomultiplier and monochromator. A heating jacket wound with nichrome strip was placed over the chamber which was heated by conduction through the air. The temperature of the ion chamber was

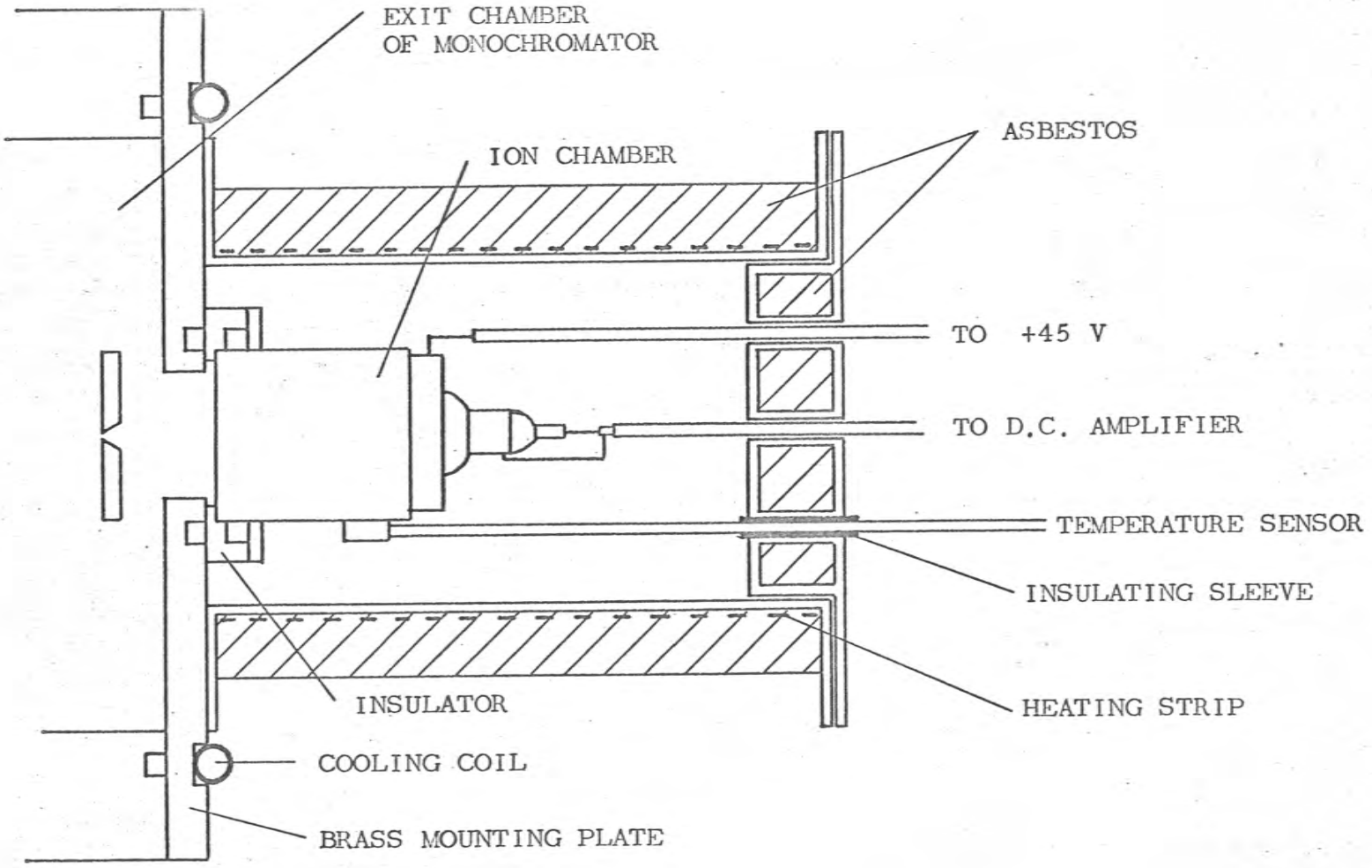

Figure 31. Cross-sectional diagram of the arrangement for heating an ion chamber mounted on the monochromator.

measured by a thermistor temperature sensor, the tip of which rested on the chamber. To avoid the effects of changes in gas gain the chamber was operated at 45V (i.e. without gas gain). The method of obtaining the spectral response was the same as that described in §3.6.2, except that a vibrating reed electrometer was used to amplify the current from the ion chamber. With each ion chamber the current through the heating coil was increased in steps to obtain several temperatures between 15 and 100°C. Sufficient time was allowed after each increase for the ion chamber to reach a steady temperature before the spectral response was recorded. Finally the chamber was allowed to cool and the response recorded again at room temperature to ensure that no permanent change had taken place.

A lithium fluoride-nitric oxide, a calcium fluoride-benzene, a barium fluoride-toluene, and a sapphire-xylene chamber were studied. The results are shown in Figure 32. It can be seen that the change in the lower limit of the spectral range is much greater than the change in the upper limit.

Laufer et al. (1965) found that as the temperature rose the transmittance versus wavelength curve at wavelengths near the transmission limit was displaced to longer wavelengths, the displacement varying linearly with temperature. Their result is confirmed by the present investigation. To make

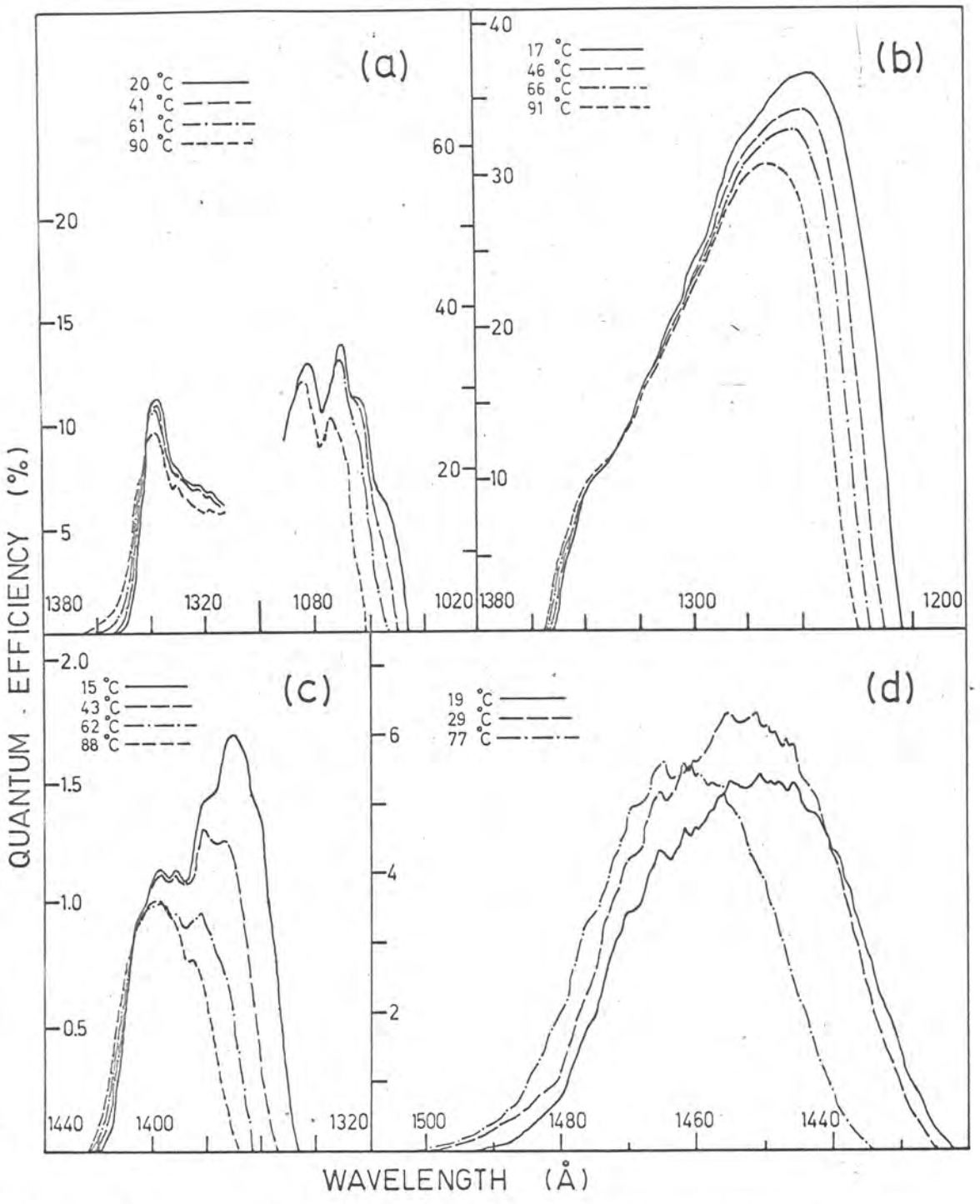

Figure 32. Variation of spectral response with temperature for the following ion chambers (a) lithium fluoride-nitric oxide,(b) calcium fluoride-benzene,(c) barium fluoride-toluene and (d) sapphire-xylene. The wavelength scale is marked in 20 Å divisions for (a),(b) and (c),and 10 Å divisions for (d). Only the ends of the curve are shown in (a) since there was no variation in the central portion.

an estimate of the rate at which the curve was displaced as the temperature changed, the wavelength at which the transmission fell to a specified value* was plotted against temperature for the four windows, as shown in Figure 33. Values for the rate of displacement of the transmission curves for the four windows, obtained from Figure 33, are shown in Table 7. They are significantly lower than those

TABLE 7. Variation of Window Transmissions with Temperature

Window	Displacement of transmission curve with temp. change ($\mathring{A}$ deg^{-1}C)		
	Present work	Laufer et al. (1965)	Knudson and Kupperian (1957).
lithium fluoride	0.22	0.30	
calcium fluoride	0.23	0.35	0.25
barium fluoride	0.37	0.39	
sapphire	0.21	0.32	

of Laufer et al. for all except barium fluoride, even considering the possible errors due to changes in photoionization efficiency in the present work. The value for

*Actually the wavelength at which the quantum efficiency of the ion chamber fell to a specified value was plotted, the values being 7% for the lithium fluoride and calcium fluoride chambers, 0.3% for the barium fluoride chamber and 1% for the sapphire chamber. However the photoionization efficiency of the filling does not vary greatly over a small wavelength range, and the transmission falls rapidly near the transmission limit, so to a good approximation it was the variation in transmission which was plotted.

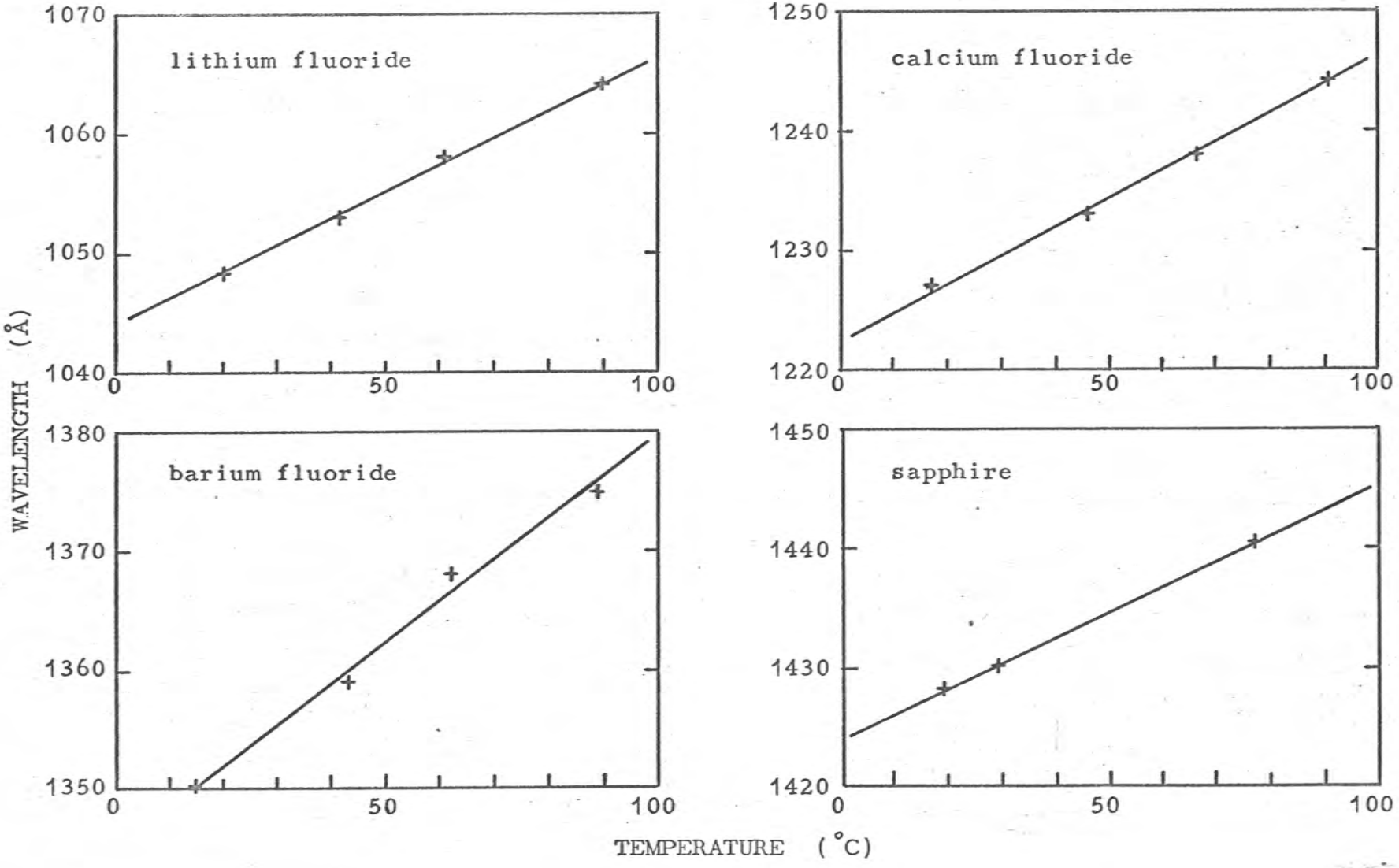

Figure 33. Variation of window transmission limits with temperature for windows of lithium fluoride, calcium fluoride, barium fluoride and sapphire.

calcium fluoride is close to that of Knudson and Kupperian.

The variation with temperature of the photoionization efficiency of the filling gas near the photoionization threshold may be estimated by making the simplifying assumption that at wavelengths longer than the wavelength λ_0 ($= \frac{hc}{E_0}$), corresponding to the adiabatic ionization potential E_0, the photoionization efficiency depends only on whether it is energetically possible for a photon to ionize a molecule, i.e. that the photoionization efficiency at a wavelength λ longer than λ_0 is proportional to the fraction of the molecules with energies greater than $E_0 - \frac{hc}{\lambda}$. If the energies of the molecules are distributed according to a Boltzmann distribution then the photoionization efficiency $P(\lambda)$ at a wavelength λ becomes

$$P(\lambda) = P_0 \exp\left[- (E_0 - \frac{hc}{\lambda})/kT \right]$$

$$= P_0 \exp\left[- hc(\lambda - \lambda_0)/kT\lambda\lambda_0 \right] \qquad \lambda > \lambda_0$$

where P_0 is the photoionization efficiency at λ_0. For wavelengths near λ_0, and a fixed photoionization efficiency $P(\lambda)$, $(\lambda - \lambda_0)$ will be nearly proportional to T. If, for example, we take $P(\lambda)/P_0 = 0.1$ and $\lambda_0 = 1400$Å, then

$$\frac{\lambda - \lambda_0}{T} = 0.031 \text{ Å deg}^{-1}\text{K}$$

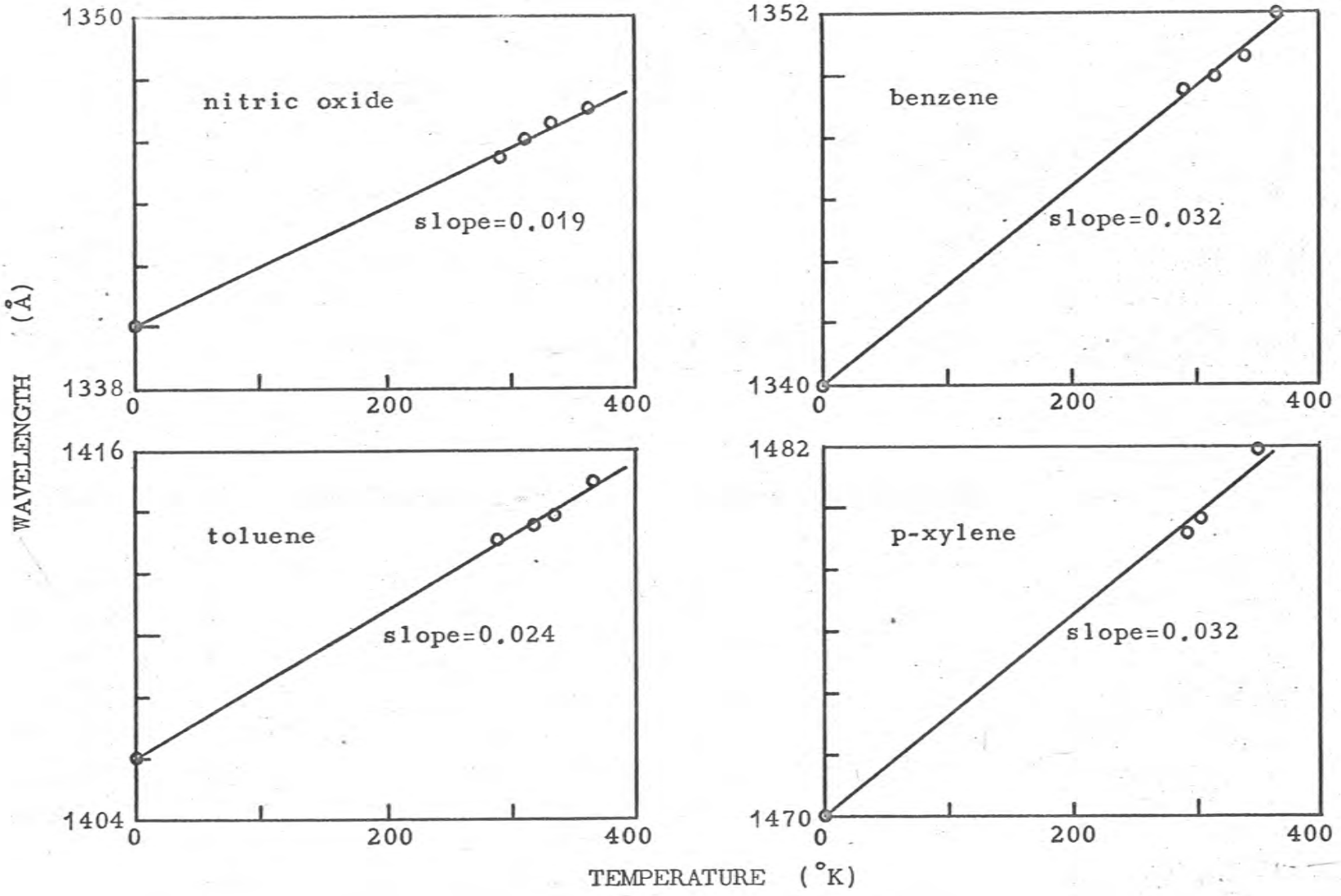

Figure 34. Variation of photoionization threshold with temperature for four filling gases. The wavelength scales are marked in 2Å divisions. The slope of each line is given in Å $deg^{-1}C$.

For $P(\lambda)/P_0 = 0.30$ the proportionality constant is 0.014 Å deg^{-1} K, and for $P(\lambda)/P_0 = 0.05$ it is 0.040. In Figure 34 the wavelength at which $P(\lambda)/P_0$ had a specified value* has been plotted against the absolute temperature. The threshold wavelength λ_0 was determined from the change of slope in the spectral response curve, the values obtained in this way being in agreement with those of Watanabe et al. (1962). The results are consistent with the interpretation given above, the temperature coefficients lying in the range 0.019 to 0.032 Å deg^{-1} K.

3.10 Gas Gain

If the voltage applied to an ion chamber is increased with a constant ultra-violet light intensity and negative polarity on the case there will be a "plateau" region where the current is almost independent of the voltage, followed by a region where the current increases due to secondary ionization near the wire. A typical current-voltage characteristic obtained under these conditions is shown in Figure 35. It was obtained using the apparatus shown in Figure 19. The gas gain at a particular voltage is defined as the ratio of the current at that voltage to the current in the plateau region. It was not necessary to use gas gain

*The values were 30% for the nitric oxide chamber, 25% for the benzene and toluene chambers and 20% for the xylene chamber.

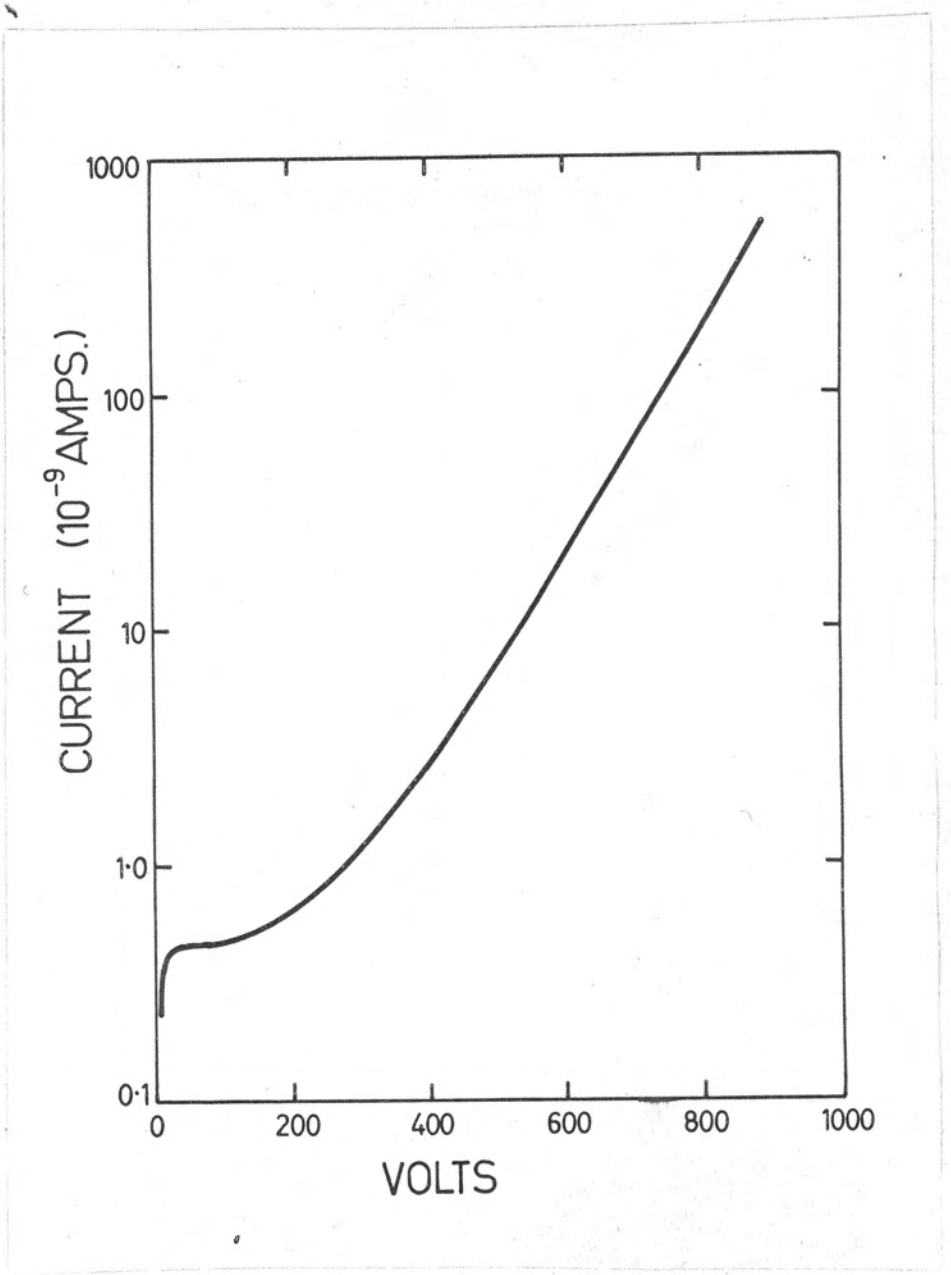

Figure 35. A typical current-voltage characteristic for an ion chamber.

for the ion chambers in the rocket experiments described in Chapter 4, but it is very useful in experiments where lower fluxes have to be detected, and also when making laboratory calibrations (see §3.6.2). Because of the importance of gas gain a more detailed study was undertaken of the statistical properties of the multiplication process, as described in Chapter 6.

While studying the effects of temperature changes on the spectral responses of the ion chambers, the effect on the gas gain was also observed. No change was observed with the chamber filled with nitric oxide, but the gas gain at 550V, of the chamber filled with xylene, decreased steadily from 55.0 at 20°C to 3.5 at 80°C. The filling pressure of the xylene filled chamber was 3 torr and was close to the saturated vapour pressure of xylene at room temperature, so the decrease in gas gain was presumably due to increased pressure in the chamber resulting from evaporation of condensed xylene and desorption from the walls of the chamber. The increase in the density of the xylene inside the chamber may be estimated by assuming that the gas gain is a function of the ratio V/ρ, where V is the voltage applied to the chamber and ρ is the density of the xylene, say $g(V,\rho) = F(V/\rho)$ (e.g. Schlumbohm 1958). Then if ρ_1 and ρ_2 are the densities at 20°C and 80°C respectively

$$g(550, \rho_2) = g\left(\frac{550\ \rho_1}{\rho_2}, \rho_1\right)$$

Using the value 3.5 for $g(550, \rho_2)$, and the gas gain curve measured at 20°C, the ratio ρ_2/ρ_1 was found to be about 2. This is considerably less than the ratio of the saturated vapour pressures of xylene at 80°C and 20°C and indicates that there was not a large amount of condensed xylene in the chamber.

3.11 Effect of intense Ultra-violet Radiation on the Ion Chambers.

It is essential that an ion chamber which is to be used for making rocket measurements of solar radiation be able to withstand exposure to the solar radiation above the atmosphere without any deterioration in response. The decrease in sensitivity, during a rocket flight, of a chamber filled with carbon disulphide, reported by Smith et al. (1965) suggested the investigation of the effects of extended exposure to ultra-violet radiation on the ion chambers used in the present work.

Each of the chambers listed in Table 6 was exposed to the radiation from the portable hydrogen lamp (§3.5) for a period of several hours, the intensity of the lamp being adjusted so that the current from the chamber was approximately equal to that which would have been obtained if the chamber had been exposed to the sun above the atmosphere. At intervals the current from the chamber was recorded. To correct for changes due to fluctuations in the intensity of

the lamp, a lithium fluoride-nitric oxide chamber was exposed to the lamp each time the response was measured, and the ratio of the two currents calculated. Figure 36 shows the results obtained when chambers filled with carbon disulphide, nitric oxide, and xylene were exposed continuously. It can be seen that there is a steady decrease in the sensitivity of the carbon disulphide chamber, but that the other two are unaffected. The results for the other chambers listed in Table 6 were similar to those for the chambers filled with nitric oxide and xylene. The carbon disulphide chamber showed a slight recovery over a period of 5 days after the irradiation was stopped (Figure 36). It was then evacuated and refilled, to determine whether the deterioration in response was due to an effect on the window or filling. The sensitivity after refilling was only about half the original value (Figure 36) showing clearly that the transmission of the window had been permanently decreased, presumably due to decomposition of the filling and deposition of the decomposition products on the window*.

The drop in sensitivity observed in this experiment was not as great as that observed by Smith et al. during the

---

*A similar effect has been observed with oil vapour by Taylor et al. (1965).

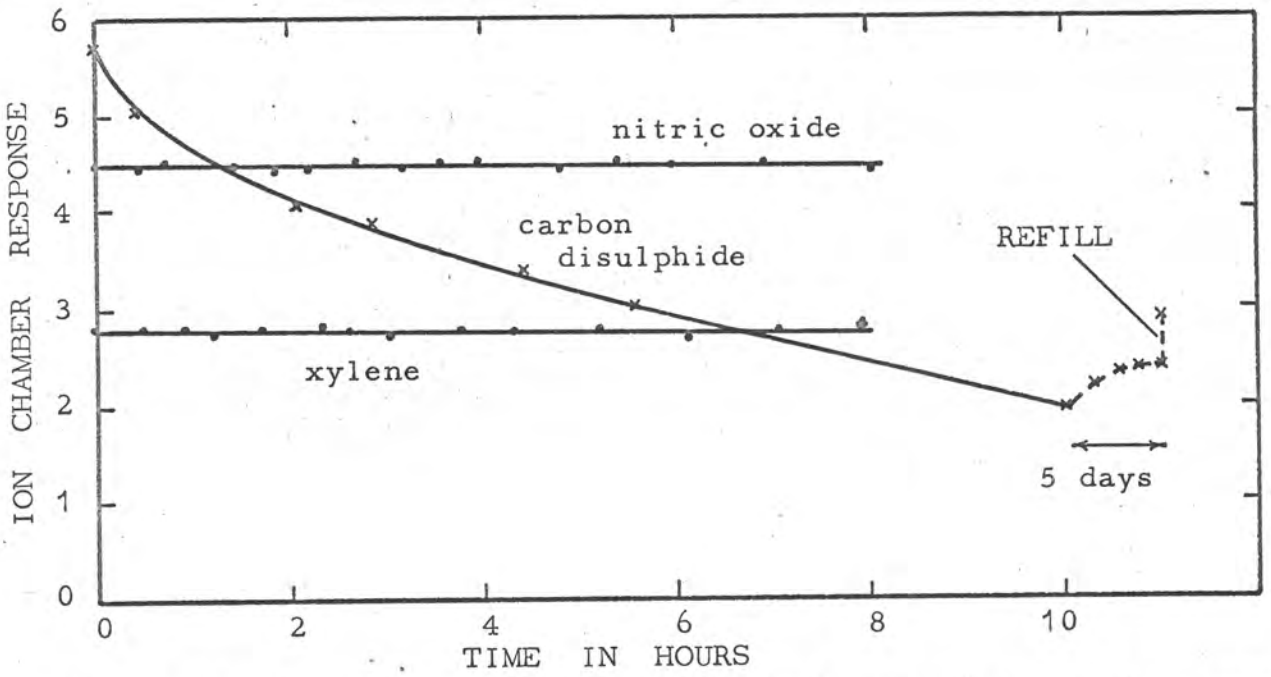

Figure 36. The variation with time of the response of three ion chambers exposed to vacuum ultra-violet radiation. The fillings are indicated on the curves.

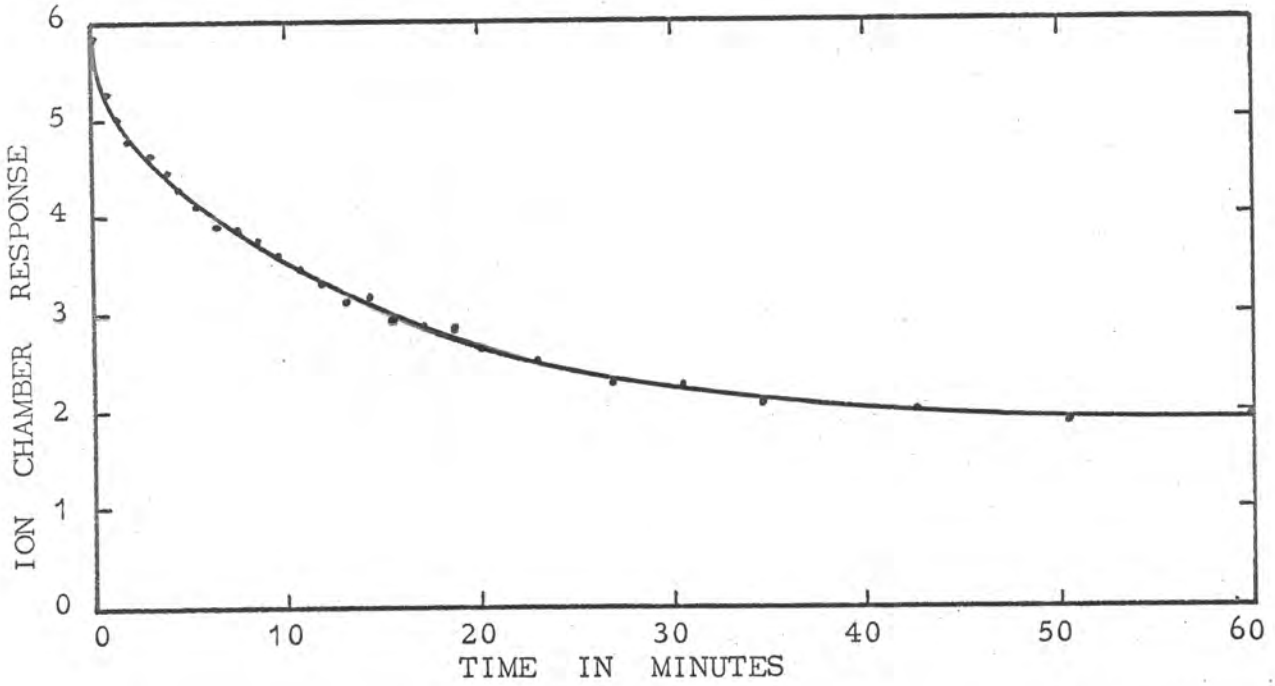

Figure 37. The variation with time of the response of the ion chamber filled with carbon disulphide when exposed to intense ultra-violet radiation from a mercury discharge lamp.

rocket flight (about 15% in 2.5 min.*, as calculated from their published curve). Carbon disulphide, however, can be decomposed by any radiation of wavelength shorter than 3260Å, the threshold for the process

$$CS_2 + h\nu \rightarrow CS + S$$

(Smyth and Blewett 1934), and the hydrogen lamp is much less intense than the sun at wavelengths longer than 1600Å. The refilled chamber was then exposed to the radiation from a quartz envelope mercury discharge lamp. The total intensity of the radiation emitted by this lamp in the range 1600 to 3000Å (mainly in the lines at 2537 and 2967Å) was measured using the radiation thermopile and found to be close to the total intensity of the solar radiation at wavelengths less than 3000Å. Figure 37 shows the variation in response observed in this case. The drop in sensitivity during the first 2.5 min. was 19% in agreement with that observed by Smith et al. After this test a deposit of rather oily appearance was clearly visible on the inside of the window. Carbon disulphide filled chambers are obviously unsuitable for rocket observations of solar radiation.

The other ion chambers listed in Table 6 were also tested with the mercury lamp but no changes in sensitivity

---

*It has been assumed that the maximum altitude of the rocket was 200 km, and the time for which the rocket was above 95 km has been halved to take into account the roll of the rocket.

larger than 2% (the limit of the accuracy of the sensitivity measurements) were observed after exposures of 10 min.

3.12 Conclusions.

Fourteen different types of ion chamber, suitable for measurements of solar ultra-violet radiation using rockets such as the HAD or Long Tom, have been constructed. The lithium fluoride-nitric oxide chamber has proved very reliable for measuring Lyman-α fluxes using the HAD rocket (Chapter 5). The spectral responses of the chambers have been measured using a method which enables the response to be automatically plotted as the wavelength is varied. It has been shown that the angular response and effective aperture of an ion chamber can be quite accurately measured in the laboratory.

As a result of tests involving exposure to ultra-violet light sources for periods of time, carbon disulphide has been proved to be unsuitable as a filling for ion chambers used in observations of the solar spectrum, because the carbon disulphide is decomposed by the relatively long wavelength ultra-violet radiation ($\lambda < 3260$Å) and the decomposition products are deposited on the window of the chamber, causing a rapid drop in transmission at short wavelengths. None of the other chambers used in the present work showed any measurable decrease in sensitivity during exposure to an ultra-violet light source equal in intensity to the sun, for a period approximately equal to that of a rocket flight.

The effects on the responses of the ion chambers of temperature changes in the range 15 to 100°C have been investigated. The limits of the spectral response are both displaced to longer wavelengths as the temperature is raised, but the response is otherwise unchanged. As expected, the change in the transmission limit of the window is larger than the change in the photoionization threshold of the filling gas, although the temperature coefficients of the lithium fluoride, calcium fluoride and sapphire windows appear to be significantly lower than those measured by Laufer et al. The change in the photoionization threshold of the filling gas may be accounted for by assuming that it is due to thermal excitation of the gas molecules which have a Boltzmann distribution of energies. Both the change in the lower limit (~ 0.25 Å $deg^{-1}C$) and upper limit (~ 0.05 Å $deg^{-1}C$) of the spectral response would need to be taken into account when making solar measurements if a strong solar line were near the limit. It has also been shown that the gas gain characteristics of chambers such as the one filled with xylene may undergo considerable changes as the temperature varies. Therefore care is necessary when making measurements with these chambers using gas gain to ensure that the gas gain is measured at the same temperature as that at which the measurements are to be made.

Of the chambers investigated the lithium fluoride-nitric

oxide, sapphire-xylene, and quartz-triethyl amine ones are especially suited to the determination of molecular oxygen densities at altitudes from 70 to 140 km in the atmosphere. The first responds to Lyman-α radiation while the other two have spectral ranges over which the absorption cross-section of molecular oxygen is almost constant (see §2.3.3).

Chapter 4. Design of the Rocket Experiment to Measure Solar Lyman-α Radiation

4.1 The HAD Rocket

The HAD rocket is a two-stage solid fuel rocket developed by the Flight Projects Group, Weapons Research Establishment, for making upper atmosphere measurements. It has been used extensively for carrying out determinations of total atmospheric density and upper atmosphere winds using the falling sphere method (Pearson 1966). When carrying telemetry equipment it reaches an altitude of approximately 90 km which makes it very suitable for measurements of the absorption of solar Lyman-α radiation at zenith angles less than about 60°, since it will spend a greater period of time in the 70 to 90 km region where the absorption takes place than a rocket which goes to a higher altitude. The space available for instrumentation is in the forward section which has a diameter of 5 in. and a length of 48 in. including the nosecone. Careful attention to the volumes and arrangement of the components was necessary in order to accommodate the Lyman-α ion chambers and their associated equipment as well as the detectors for 2700Å radiation which were included so that ozone concentrations could be measured. During the three second burning period of the motors the acceleration may reach 70g and the vibration 10g so the components must be able to withstand

these conditions.

Three HAD rockets were instrumented for the Lyman-α and ozone measuring experiments. Those designated HAD 301 and HAD 304 were successfully fired on 6 December 1963 and 4 February 1965, respectively. The third, HAD 302, was fired on 11 December 1963 but failed owing to a fault in the second stage motor which caused exhaust gases to pass through the instrument section. All the firings took place at the Woomera Rocket Range (lat. 30°56'S, long. 136°31'E).

Altitude data for the flights were obtained from radar tracking of the rocket body. Aquisition by the radar was assisted by a tracking oscillator* in the instrument section. The analysis of the height data is described in detail in §5.4

4.2 Design of the Rocket Head

The arrangement of the components in the rocket head is shown in Figure 38, while Figure 39 is a photograph of the completed head.

The strong-ring which contained the Lyman-α detectors, aspect sensors and telemetry aerials can be seen in Figure 39 about half-way up the head. The detectors and sensors were covered by a fibre glass band during the first part of

---

*The oscillator formed part of the "ackaid" system installed at Woomera. The signal from the oscillator was received by a special aerial and used to supply altitude and azimuth data directly to the radar equipment.

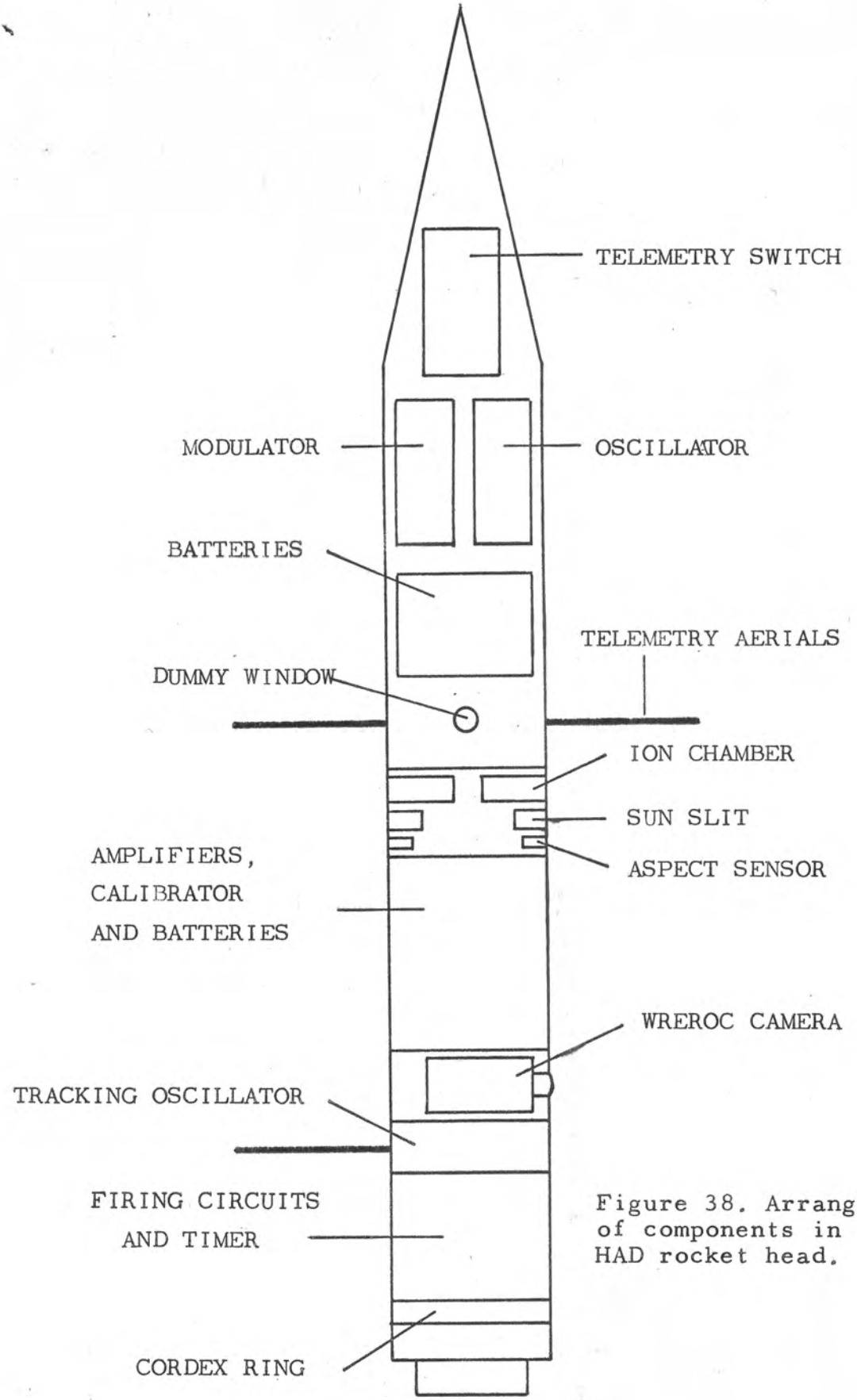

Figure 38. Arrangement of components in the HAD rocket head.

Figure 39. Complete rocket head for HAD 304. The cover band which fitted just below the telemetry aerials has been removed so as to expose one of the lithium fluoride-nitric oxide chambers and the aspect sensors associated with it. Level with the aerials is the dummy window with a thermistor attached. The lens of the WRREOC camera can be seen half-way between the detector ring and the base.

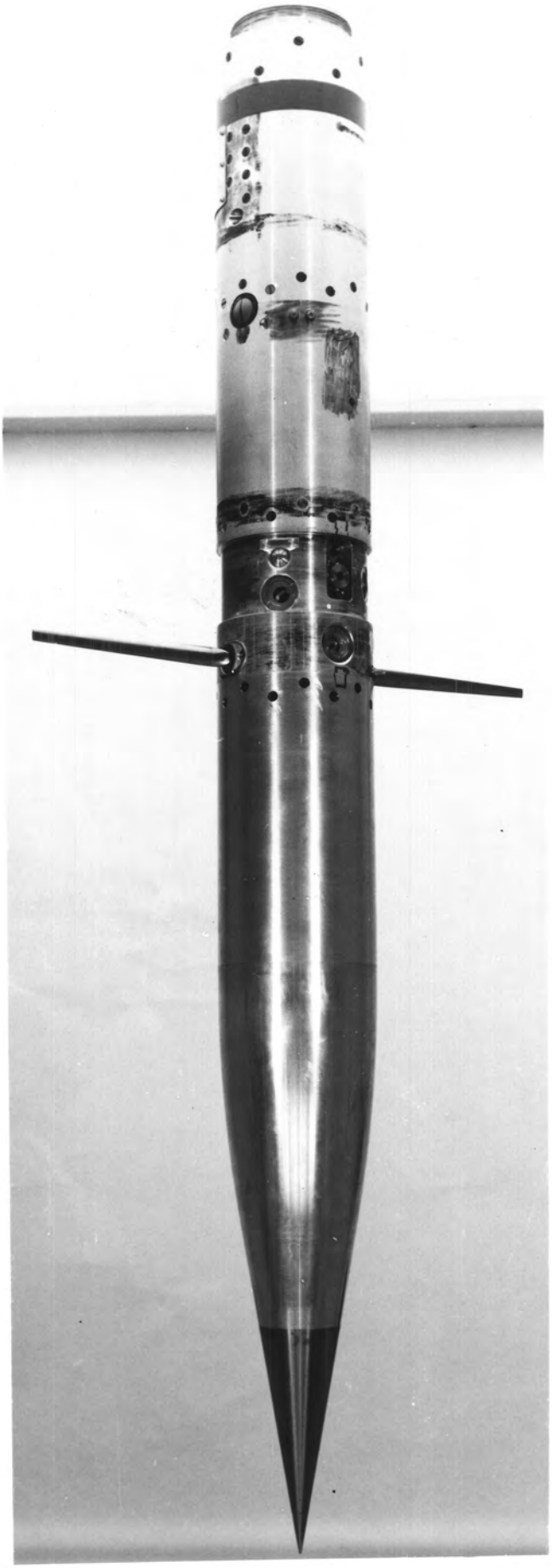

the flight to protect them from the effects of heat generated on the surface of the rocket during its rapid passage through the air at low altitudes. It was timed to be released 28 sec. after launch at an altitude of 30 km, just after the second stage motor had finished burning. Two lithium fluoride-nitric oxide ion chambers, one of which can be seen in Figure 39, were mounted so that they pointed in opposite directions. The use of two chambers provides a safeguard against failure in one of the chambers or its associated circuits. If both function satisfactorily they give twice as many measurements of Lyman-α intensity as one chamber and so give better data in the event of a slow roll rate. Teflon washers were used to insulate electrically the cases of the chambers from the rocket body so that the operating voltage of 45V could be applied to the cases. The resistors potted in the backs of the chambers (§3.2) were included so that in the event of a short circuit occurring between the case of one chamber and earth the voltage on the other chamber would not also drop to OV.

The cover band release mechanism can be seen to the left of the Lyman-α detector (Figure 39), and below the detector are the aspect sensors which are described in detail below (§4.4). Level with the telemetry aerials is the dummy window which was included in HAD 304 to measure the temperature to which an ion chamber would rise if

unprotected during the whole flight (see §5.3). It was identical to the front section of an ion chamber but had a thermistor attached to the back of the window.

The section above the aerials, including the nosecone, contained the telemetry sender and its power supplies, while below the strong-ring were the amplifiers, calibrator and power supplies associated with the detectors. Below these were the WRERDC camera (§4.4), the lens of which can be seen in Figure 39, and the tracking oscillator. The dark band around the base of the head was a cordtex ring used to separate the head from the second stage motor at an altitude of 15 km on the way down. In this way the head is made to tumble rapidly so that the aerodynamic drag is considerably more than it would be for a rocket pointing straight down. Thus the velocity is reduced and there is less damage at impact.

4.3 Electrical Circuitry

The circuit of an ion chamber and its amplifier are shown in Figure 40. A miniature electrometer valve was used for the input stage of the amplifier, the current from the chamber being passed through a resistor connected between the grid of this valve and earth. Resistances of 27 MΩ were required for the Lyman-α detectors but values up to 1000 MΩ could be used with this valve. Compensation for zero drift caused by temperature changes was provided by a

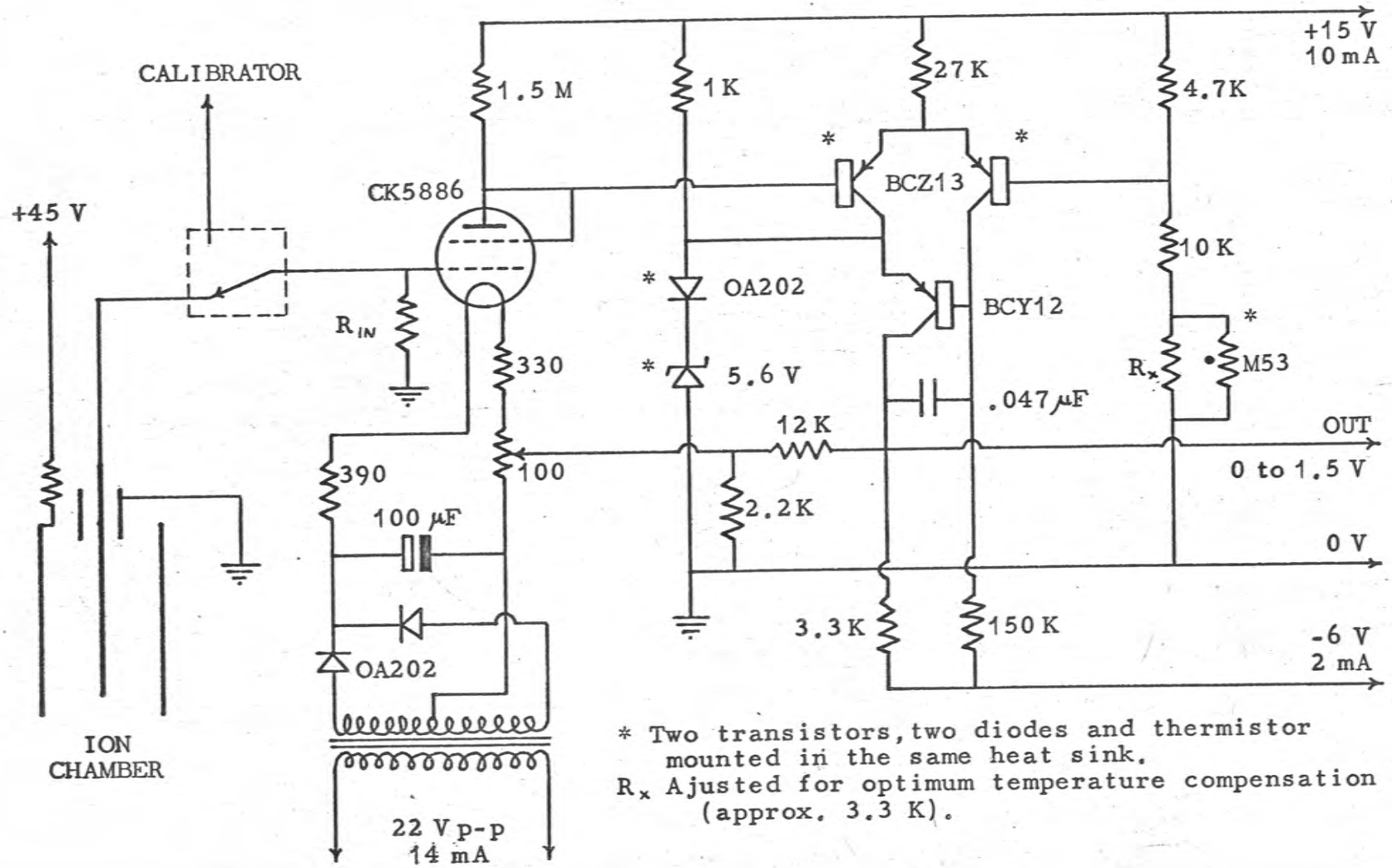

Figure 40. Circuit of an electrometer amplifier and ion chamber.

thermistor attached to the heat sink in which the transistors were mounted. During flight the zero drift observed at the output was always less than 10 mV or about 0.7% of full scale.

The telemetry sender was assembled from standard components. The outputs from the ion chamber amplifiers and other sensors (0 to + 1.5V) were taken to a 24 channel rotary switch which sampled each channel 80 times per second. From the switch the signals went to a frequency modulator, the output of which was used to modulate the 465 Mc signal from the main oscillator. Fixed voltage levels were applied to five positions on the switch to enable the linearity of the telemetry sender and receiver to be checked.

A calibrator was included so that the ion chamber amplifiers could be calibrated during the flight. At 30 sec. intervals the currents from the ion chambers were disconnected from the amplifiers by a relay and two voltages of 0 and 0.35V respectively were applied to the inputs for 200 m sec. each. The distance between these levels on the final telemetry record then corresponded to an input current of $\frac{0.35}{R}$ A, where R was the input resistor of the particular amplifier.

4.4 Aspect Sensing

4.4.1 The Different Methods of Obtaining Solar Aspect.

Since the response of an ion chamber changes as the

aspect angle* varies (§3.8.1) it is essential to know the solar aspect angle during the rocket flight so that the response of the ion chamber can be corrected to what it would have been if the chamber had been pointing directly at the sun. Several methods have been used for obtaining this information.

In most flights the roll rate of the rocket (the rate of rotation about the rocket axis) is much greater than the rate at which the rocket axis changes its position in space due to precession or any other motion. In this case the Lyman-α detector will show one peak in its output for each roll and it is the aspect angle at the peak which is required. For any ion chamber pointing in a direction perpendicular to the axis of the rocket this angle is the complement of the angle between the direction of the sun and the rocket axis (see Figure 41). This will be referred to as the rocket aspect angle θ in such cases. However, the HAD rocket will not always behave in this way (e.g. HAD 301, see §5.1), and then a sensor which gives the aspect angle of the ion chamber continuously is required. The relative merits of the different aspect sensors are discussed below.

---

*The aspect angle is the angle between the direction in which the ion chamber is pointing and the direction of the incident light.

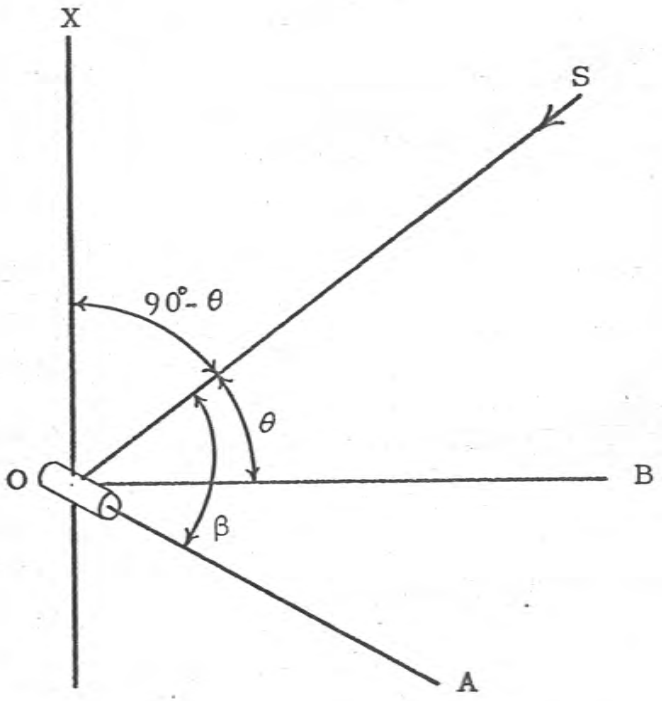

Figure 41. Diagram illustrating the rocket aspect angle. The axis of the rocket is OX and the detector is situated at O pointing in the direction OA. The direction of the sun is OS so β is the aspect angle for the detector. The rocket aspect angle is θ where OB is perpendicular to OX and in the plane of OX and OS.

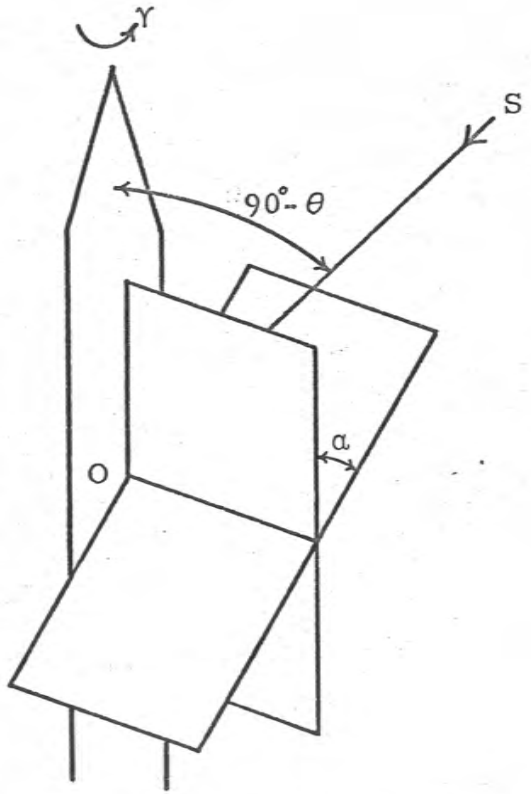

Figure 42. Diagram illustrating the operation of the sunslits. The two planes inclined at an angle α are the planes of the slits cut in the sensor. The direction of the sun is OS and the rocket rolls through an angle γ while OS passes from one plane to the other. Then

$$\tan\theta = \sin\gamma \cot\alpha \ .$$

(a) Sensors using amplitude-modulation.

A sensor of this type was used in the experiments of Kupperian et al. (1959) and has been described by Kupperian and Kreplin (1957). It consisted of a phototransistor sensitive to visible light mounted behind a filter glass window so that the response varied with angle due to variation of the effective area. Calibration was carried out prior to flight.

The main problem with an aspect sensor of this type is that the light to which it is responding is attenuated in passing down through the atmosphere owing to Rayleigh scattering (increasing as the wavelength decreases) and absorption by ozone and water vapour. However, the scattering and absorption will take place mainly in the lower, more dense atmosphere, so that in the region above 70 km where the aspect is required the intensity of the sun's visible and near infra-red radiation will be constant. Thus if the aspect angle can be determined at one particular time while the rocket is above about 40 km (see §5.5) this information enables the level of the laboratory calibration curve to be adjusted so that the aspect angle can be determined at other times. The extra information may be obtained, for example, from the sunslit sensor or the camera described below. Using these detectors the time at which the rocket aspect angle was zero can be determined quite

accurately if the roll rate is high. However, the information required to adjust the level of the calibration curve may not be available, particularly if the motion of the rocket is irregular. To overcome this difficulty a double amplitude-modulation sensor was designed which is described below (§4.4.2).

A second difficulty when using this type of sensor arises from the fact that, owing to reflection from the surface of the earth and clouds, light coming up from below will be detected by the sensor as well as light coming directly from the sun. Since this earthshine* extends almost over a hemisphere and the sensor has a wide field of view there will be response to the earthshine at all times except when the sensor is pointing to the zenith. This is discussed further in §4.4.2.

(b) Sensor using time-modulation.

A different type of sensor is that which responds only when the sun crosses one of several planes fixed relative to the rocket body, and the aspect information is derived from the spacing in time of the pulses so produced. These sensors rely on a suitable roll rate to produce the pulses and are of little use if the motion of the rocket is slow or irregular. On the other hand a roll rate which is too fast will be unsuitable when using a telemetry system such

---

*The term suggested by Danjon (1954) has been used to describe the reflected light.

as the one used in the HAD rockets where each channel is sampled 80 times per second. For example, if the roll rate is 2 cps the spacing of the pulses can be determined with an accuracy of only ± 4.5° in roll and this would lead to considerable error in the determination of the rocket aspect angle. The advantage of this type of sensor over those using amplitude-modulation is that variations in the intensity of the light to which they are responding or in the sensitivity of the sensor do not affect the accuracy. The earthshine also has no effect.

The sunslits used on the Skylark rocket (Gross and Heddle 1964) have a detector placed behind two slits, one cut in a plane containing the rocket axis, and the other in a plane intersecting the first along a line perpendicular to the rocket axis and making an angle α with it (see Figure 42). Then if the rocket has rolled through an angle γ in the interval between two pulses the rocket aspect angle θ is given by

$$\tan \theta = \sin \gamma \cot \alpha$$

A modified version of the Skylark sunslit was used in the HAD rockets. It can be seen in Figure 39 immediately below the Lyman-α detector. Three slits 0.3 mm wide were cut in an aluminium hemisphere, one containing the rocket axis and the other two making an angle of 45° with it so that the slits intersected along a line passing through the

centre of the sensor. A photodiode placed behind a pinhole detected the passage of the sun across one of the slits. The use of three slits allows a check to be made on whether the roll axis coincides with the axis of the rocket, since if the axes do not coincide the time intervals between the second pulse and each of the others will not be the same. If the axes do not coincide the analysis of the sunslit data will be more complicated. The sunslits were calibrated before flight to determine whether they obeyed the relation given above, which for $\alpha = 45^\circ$ becomes

$$\tan \theta = \sin \gamma$$

It was found that this relation was satisfied for values of θ in the range -40° to $+40^\circ$. Outside this range no response was obtained through the two 45° slits.

A more elaborate aspect sensor employing time-modulation has been developed by McKinnon and Smith (1964) and used in experiments similar to the present one (Smith et al. 1965, Smith and Weeks 1965). A diamond shaped slit was made in a flat plate which was mounted in front of a photovoltaic cell. The sensitive area of the cell was restricted by a second plate with a small hole in it, a pulse being produced whenever the sun crossed a plane defined by the hole and one section of the diamond shaped slit. It is stated that with this sensor the aspect angle can be measured with a probable

LIBRARY OF THE UNIVERSITY OF ADELAIDE

error of 1° or less in the range $\theta = -70^{\circ}$ to $+ 70^{\circ}$.

(c) Cameras

Photography provides a simple method for determining rocket aspect but suffers from the disadvantage that recovery of the rocket head is essential. Recovery facilities are available at Woomera but an object the size of a HAD rocket head is obviously difficult to find even when its approximate position is known from radar tracking. Of the three HAD rockets used in the present work the heads of HAD 302 and HAD 304 were recovered but that of HAD 301 was not. Although a camera cannot be relied upon exclusively for aspect information one was included in each of the HAD rockets to provide a check on the operation of the other sensors.

The camera used was a WRERDC camera supplied by the Weapons Research Establishment. It has a 180° lens masked so that a strip of the sky parallel to the rocket axis is imaged onto a continuously moving (1 in. sec^{-1}) 35 mm film (see Figure 39). If the rocket motion is regular (roll rate faster than the motion of the rocket axis) an image of the sun is formed on the film for each roll of the rocket and the rocket aspect angle can be determined from the position of the image.

4.4.2 The Double Amplitude-Modulation Sensor.

Since neither the sunslit nor the WRERDC camera was entirely satisfactory for use in the HAD rocket, for the

reasons given above, an amplitude-modulation sensor was designed which could be included together with the other sensors.

A small silicon photodiode (type LS 400) was used for the sensor. The angular response of the photodiode by itself was found to peak strongly in the forward direction, so to overcome this it was mounted in a teflon plug contained in a aluminium body as shown in Figure 43 (sensor 1). Light reached the photodiode by diffusion through the teflon and the response depended mainly on the effective area of teflon exposed to the light. This can be seen from the measured response shown in Figure 44 (sensor 1) which varies approximately as the cosine of the aspect angle. This curve was obtained using as a source a light globe placed behind a screen in which a 5 mm hole had been drilled. The distance of the sensor from the screen was adjusted so that the hole subtended an angle at the sensor equal to the angular diameter of the sun ($\sim 0.5^{\circ}$).

As pointed out above (§4.4.1 (a)) even if the sensor had been calibrated using the sun as a source the level of the response for a particular aspect angle would be different at an altitude of 70 km owing to atmospheric absorption. This difficulty may be overcome by using a second sensor having a different angular response but the same spectral response. Then if the angular responses are suitably

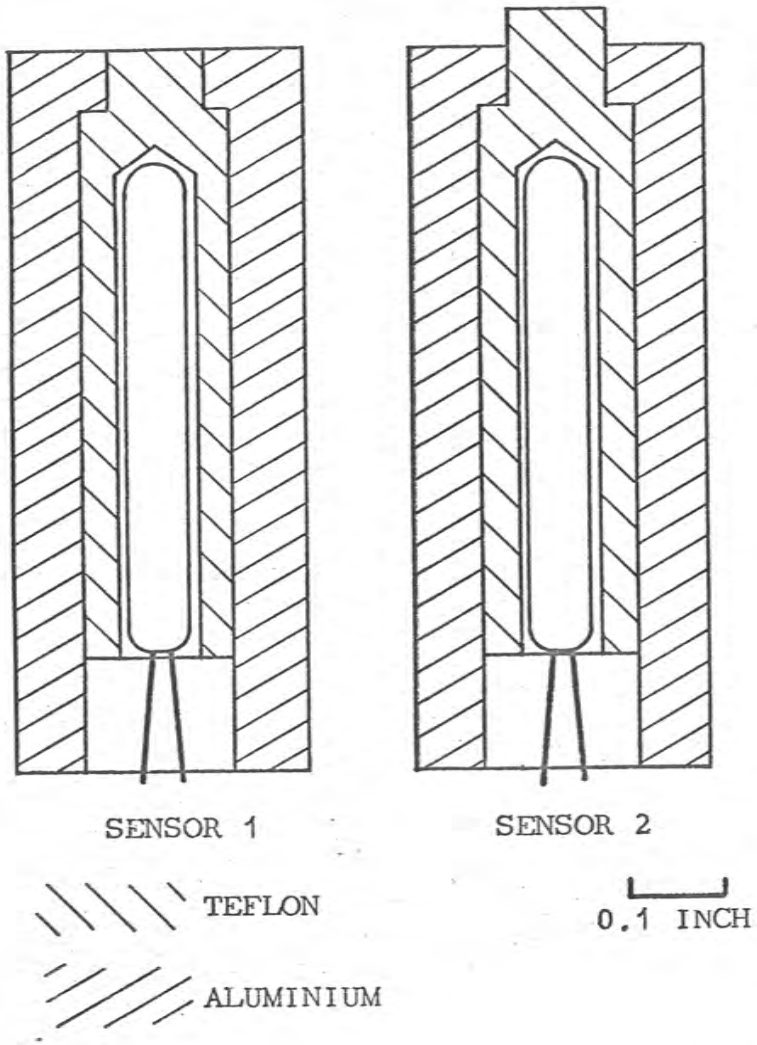

Figure 43. Cross-sectional diagrams of the two aspect sensors.

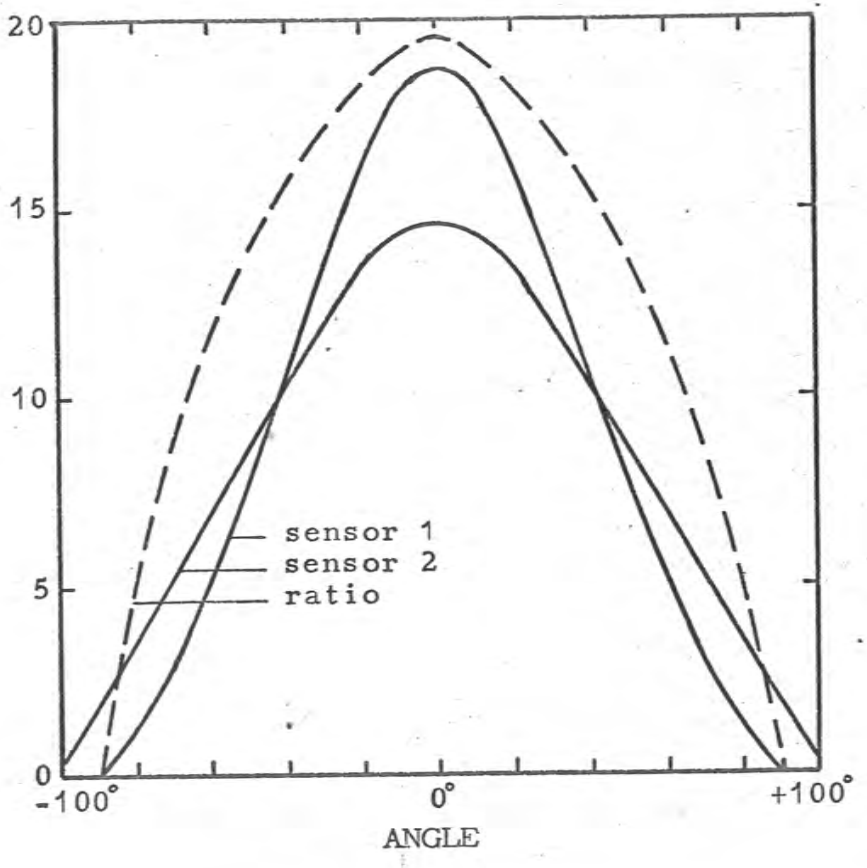

Figure 44. Angular response curves for the two sensors shown in Figure 43. The dashed line is the ratio $\frac{\text{sensor 1}}{\text{sensor 2}}$.

chosen their ratio will be a unique function of the aspect angle and as the sensors respond to the same radiation the ratio will be independent of the intensity. A suitable modification of the angular response was produced by making a teflon plug identical to the first except that the teflon protruded a small distance from the aluminium body as shown in Figure 43 (sensor 2). The resulting broadened response curve is shown in Figure 44 (sensor 2). Also shown is the ratio of the two responses as a function of aspect angle.

The spectral response of the sensors was measured by exposing both the sensor and a radiation thermopile simultaneously to the beam from a quartz prism spectrometer (Beckman type DU) using a tungsten lamp as the light source. At each wavelength the ratio of the two responses was calculated, giving the spectral response curve shown in Figure 45. To minimize the effect of the earthshine (§4.4.1 (a)) the sensor should be sensitive to the wavelength region where the ratio of the intensity of the solar spectrum to the intensity of the earthshine is a maximum. The spectral distribution of the earthshine is not accurately known, however, so it is not possible to say where this region is. Kupperian and Kreplin (1957) state that their sensor was insensitive to the earthshine, but the spectral response was not given. They used a germanium photo-transistor with a red glass filter. The present sensors

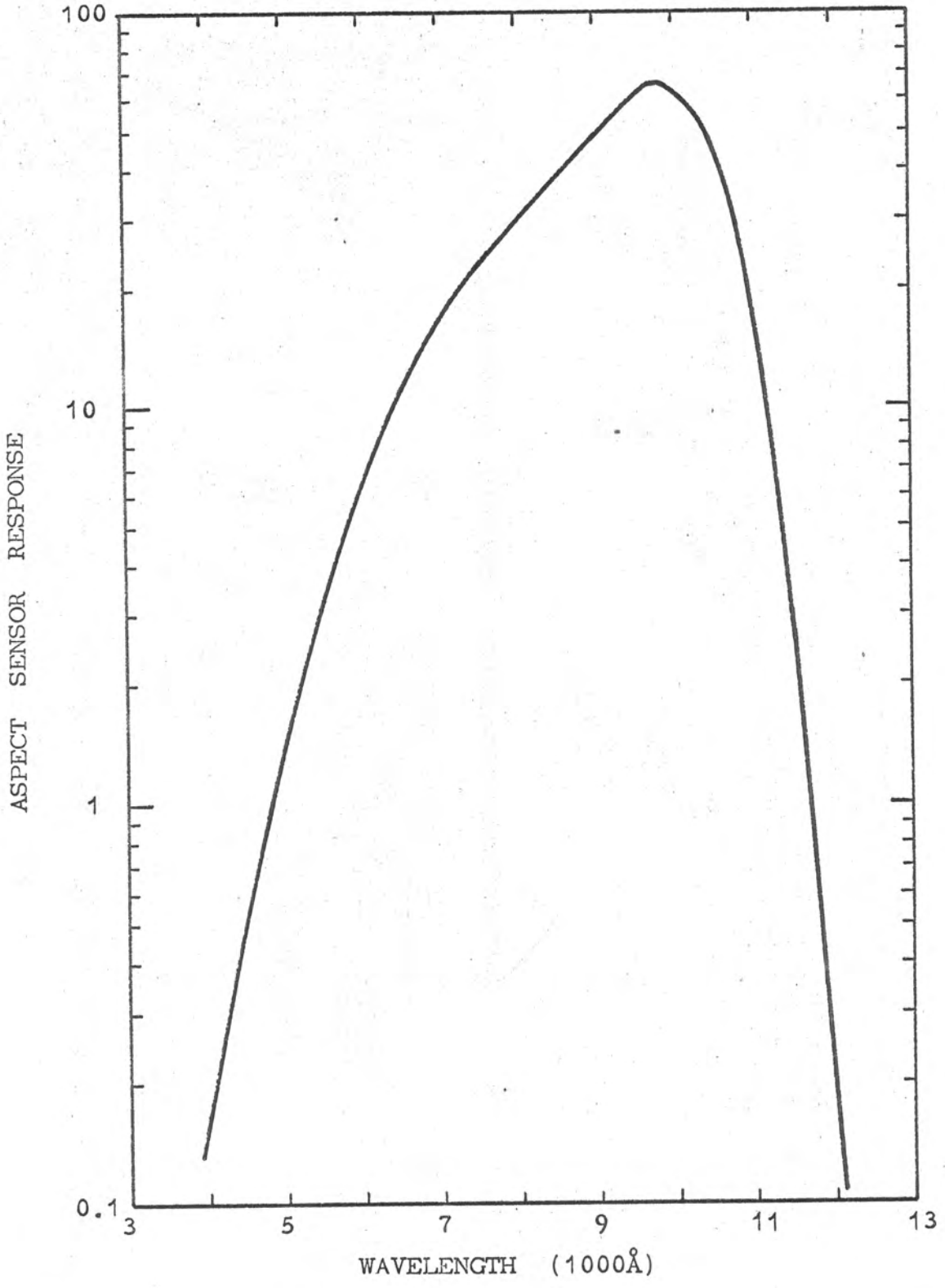

Figure 45. Spectral response of the aspect sensors shown in Figure 43. The response is given in units proportional to the current from the sensor per unit energy flux incident on it.

recorded a maximum signal due to the earthshine which was 10% of the signal due to the sun at an aspect angle of 0°. Since their spectral response (which had a maximum at 9800Å) probably lay further towards the infra-red than that of Kupperian and Kreplin's sensor, it appears that the ratio of the intensity of the solar spectrum to the intensity of the earthshine is lower in the near infra-red than in the visible. If this is the case the operation of the present sensors would be improved by reducing their response to near infra-red radiation.

In the rocket the two sensors 1 and 2 forming a pair were mounted directly below the sunslit (Figure 39) so that they pointed in the same direction as each other and the ion chamber. When operated as a photoconductive diode the LS 400 shows a "plateau", the current for a fixed light input being independent of the voltage over the range 0.5 to 10V. Therefore the output signal was obtained simply by connecting the diode and a resistor in series to a 6V supply and taking the voltage across the resistor to the telemetry sender.

The results obtained from the use of this sensor in HAD 304, and the method of analysis, are described in §5.5.

4.4.3 Conclusion

The problem of aspect determination has been discussed at some length because of its importance and because none

of the methods previously used satisfied all the requirements necessary for use in the HAD rocket. These were (1) the aspect sensor had to be able to operate when the motion of the rocket was slow or irregular (2) the sensor had to be compatible with a telemetry system which had a time resolution of 125 m sec. and (3) the sensor had to be sufficiently small to be mounted near the skin of a 5 in. diam. rocket so that it could have a wide field of view.

Neither the single amplitude-modulation sensor of Kupperian and Kreplin nor the time-modulation sensors of Gross and Heddle or McKinnon and Smith satisfy all these requirements for the reasons discussed in §4.4.1. However, the double amplitude-modulation sensor described in §4.4.2 does satisfy these requirements and in addition is easy to construct and requires only very simple electrical circuitry. Its principal disadvantage at present is its relatively large response to the earthshine, but this can probably be overcome by altering the spectral response.

Chapter 5. The Results of Two Experiments to Measure Solar Lyman-α Radiation

Introduction

As mentioned in §4.1, two HAD rockets were successfully fired carrying ion chambers to measure the intensity of solar Lyman-α radiation and to determine the density of molecular oxygen in the 70 to 90 km region from the absorption of the Lyman-α radiation. Owing to a higher roll rate and more accurate determination of the solar aspect, the data from HAD 304 were considerably better than those from HAD 301, and will be discussed in more detail.

(A) HAD 301

5.1 Rocket Performance

The rocket HAD 301 was fired at 0912 hours local solar time on 6 December 1963, when the solar zenith angle was 37°*. It carried two ion chambers for detecting Lyman-α radiation, together with their associated equipment as described in Chapter 4, except that the only aspect sensors were the sunslits and the WREROC camera. The rocket reached a maximum altitude of 88 km and satisfactory telemetry signals were received throughout the flight.

---

*The solar zenith angles for the two flights were calculated using astronomical tables.

The roll period of the rocket during the flight was about 17 sec which was much longer than had been expected. A total of fourteen scans of the sun were made by the two Lyman-α detectors and since the sunslits provided the aspect angle only once for each scan only fourteen measurements of the Lyman-α flux were obtained. The relatively slow roll rate also meant that the aspect data from the sunslits were subject to considerable error, the uncertainty being about ±5°. No aspect information was obtained from the WREROC camera since the rocket head was not recovered.

5.2 Results from HAD 301

Because of the uncertainty in the intensity measurements due to the uncertainty in the aspect data, values obtained at approximately the same height on ascent and descent were averaged giving eight values for the Lyman-α flux at various heights between 69.7 and 88.3 km. These are shown in Figure 46 together with a smooth curve representing the variation of Lyman-α flux with height.

To calculate the molecular oxygen densities the four flux values listed in Table 8 were derived from the ones shown in Figure 46. The total number of oxygen molecules per cm^2 column in each of the three height intervals was then calculated from the relation

$$\phi(h_1)/\phi(h_2) = \exp(-\sigma N \sec z) \qquad (1)$$

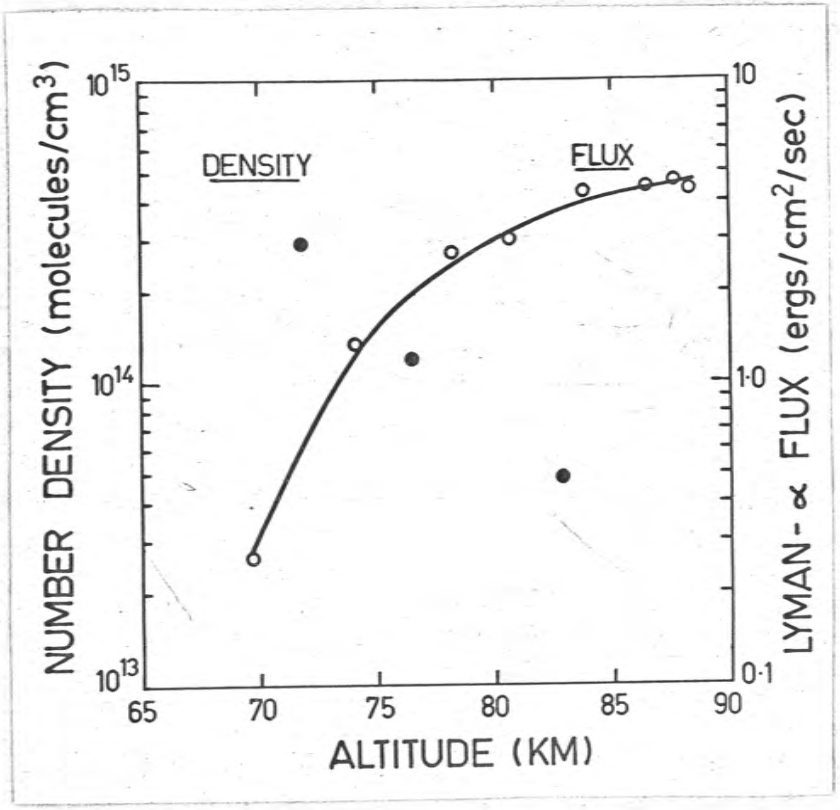

Figure 46. Lyman-∝ fluxes (open circles, o) and oxygen densities (solid circles, ●) from HAD 301.

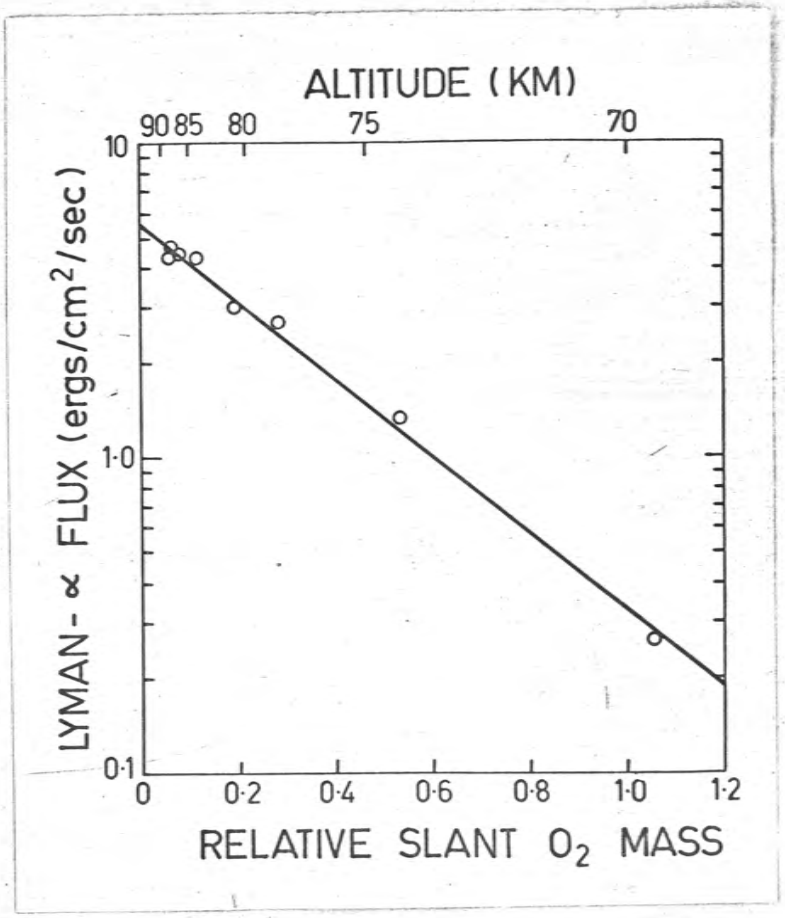

Figure 47. Lyman-∝ fluxes from HAD 301 plotted against slant oxygen mass (see text).

TABLE 8 : Oxygen Densities from HAD 301

Height h (km)	Lyman-α flux $\phi(h)$ (erg cm^{-2} sec^{-1})	Height h' (km)	O_2 number density n(h') (cm^{-3})
69.7	0.266	71.9	2.9×10^{14}
74.1	1.33	76.5	1.18×10^{14}
79.0	2.79	82.8	4.8×10^{13}
86.5	4.41		

where N is the number of molecules per cm^2 between h_1 and h_2 (equation (5), p.28). It was assumed (see §5.6, §5.8) that the detectors were detecting only Lyman-α radiation and that molecular oxygen was the sole absorber. A value of 1.00×10^{-20} cm^2 was used for σ (§2.1 (a)), and z was 37° as stated above. The average number density in each height interval was then calculated from $n = N/\Delta h$, where $\Delta h = h_2 - h_1$, and this was taken to be the density at the mid-point h' of the height interval (Table 8). This assumption was a good approximation to the actual situation since the height intervals were of the order of the molecular oxygen scale height (6.5 km) in this region*. The values of n(h') are plotted in Figure 46.

*Footnote next page.

To determine the intensity of the solar Lyman-α line the measurement taken at the highest altitude could have been corrected by estimating the amount of oxygen still above the detector and applying a correction for the absorption due to it. However it was preferable in this case to use a method which took into account all the measurements, since each was subject to experimental error. The method was as follows. From the three densities shown in Figure 46 it was estimated that in the region 70 to 85 km the scale height of the molecular oxygen density was 6.5 km. It was then assumed that this was true for all heights above 65 km, i.e.

$$n(h) = n(70)\ \exp[-(h-70)/6.5]$$

for all values of h greater than 65. Then

$$\ln \phi(h) = \ln \phi_0 - \sigma N(h) \sec z$$
$$= \ln \phi_0 - \sigma N(70) \sec z \exp[-(h-70)/6.5]$$

where ϕ_0 is the Lyman-α flux above the oxygen and N(h) is the number of oxygen molecules per cm^2 column above the height h.

---

*(from page 108)

If $n(h)=n_0\exp(-h/H)$ over an interval Δh above h_1, and the density at the height $h_1 + \Delta h'$ is equal to the average density in the interval h_1 to $h_1 + \Delta h$, then

$$\frac{\Delta h'}{\Delta h} = -\frac{H}{\Delta h} \ln\left[\frac{H}{\Delta h}\left(1-\exp\left(-\frac{\Delta h}{H}\right)\right)\right]$$

Some values are given in the following Table

$\Delta h/H$	0.1	0.5	1	2
$\Delta h'/\Delta h$	0.495	0.48	0.46	0.42

In Figure 47 the logarithms of the flux values shown in Figure 46 have been plotted against the quantity $\exp[-(h-70)/6.5] = N(h)/N(70)$, resulting in a straight line as suggested by the relation given above. The quantity $N(h)/N(70)$ has been called the slant oxygen mass. From the graph a value of 5.4 erg cm^{-2} sec^{-1} was obtained for ϕ_o. The slope of the graph is equal to σ sec z N(70) and using the values of σ and z given above a value of 2.2×10^{20} cm^{-2} was obtained for N(70), the number of oxygen molecules per cm^2 above 70 km.

(B) HAD 304

5.3 Rocket Performance

The rocket HAD 304 was fired at 0825 hrs. local solar time on 4 February 1965, when the solar zenith angle was 53°. The instrumentation was identical to that of HAD 301, except for the addition of the amplitude-modulation sensor described in §4.4.2. This sensor functioned very satisfactorily and the analysis of the aspect data is described in detail below (§5.5). In addition HAD 304 differed from HAD 301 in that the tail fins were shaped so as to increase the roll rate. The result was that the roll period was 0.38 sec, considerably less than that of HAD 301. The period was constant to ± 0.005 sec while the rocket was above 65 km. While this period was very suitable for the Lyman-α detectors, the amplifiers for which had a frequency response of 70 cps,

it was unfortunately too short for accurate data to be obtained from the sunslits, the time resolution of the telemetry system corresponding to 12° in roll.

The maximum height attained was 91 km, but the radar tracking was incomplete as the radar lost the rocket from 85 km on the way up to 65 km on the way down. The method used to interpolate the heights in the missing part is described in the next section. Owing to noise originating in the telemetry modulator in the rocket, the telemetry records were unreadable from a few seconds after launch until just before the rocket reached maximum height. However, the noise was completely absent on the downward part of the flight so no essential data were lost.

The cover band release mechanism operated 3.5 sec after launch instead of 28 sec as planned thus exposing the Lyman-α detectors to the effects of aerodynamic heating. The thermistor mounted behind the dummy window (§4.2) recorded a maximum temperature of 110°C, 10 sec after launch, so the Lyman-α detectors probably reached a temperature near this. The fact that the detectors performed satisfactorily thoughout the flight, and that the one which was recovered intact had the same sensitivity as it had before the flight, shows that the ion chambers used in the present work are able to withstand the conditions in a HAD flight without the protection of the cover band.

5.4 Analysis of the Height Data

Before describing the method used in the analysis of the height data it will be useful to discuss the effects of factors which cause the trajectory of a rocket to deviate from the simple form $h(t) = h(o) - \frac{1}{2}gt^2$. (Throughout this section the time t will be measured from the time of maximum height, i.e. $v(o) = o$ where $v(t)$ is the vertical component of the velocity). The two most important factors are (a) air drag, and (b) variation in g.

(a) Air Drag.

The effect of air drag is to make the trajectory unsymmetrical i.e. $h(-t) < h(t)$. This is illustrated in Figure 48(a). The effect will decrease as the height increases, and since for a HAD rocket drag may be ignored at heights greater than 50 km (see below) the form of the trajectory will not be analysed in detail.

(b) Variation in g.

The value of g varies inversely as the square of the distance from the centre of the earth, but over a range of about 40 km the decrease of g with height will be very nearly linear and we may write

$$a(t) = -[g_o + k\,(h(o) - h(t))] \qquad k>o$$

where $a(t)$ is the vertical acceleration of the rocket and g_o is the value of g at the height $h(o)$.

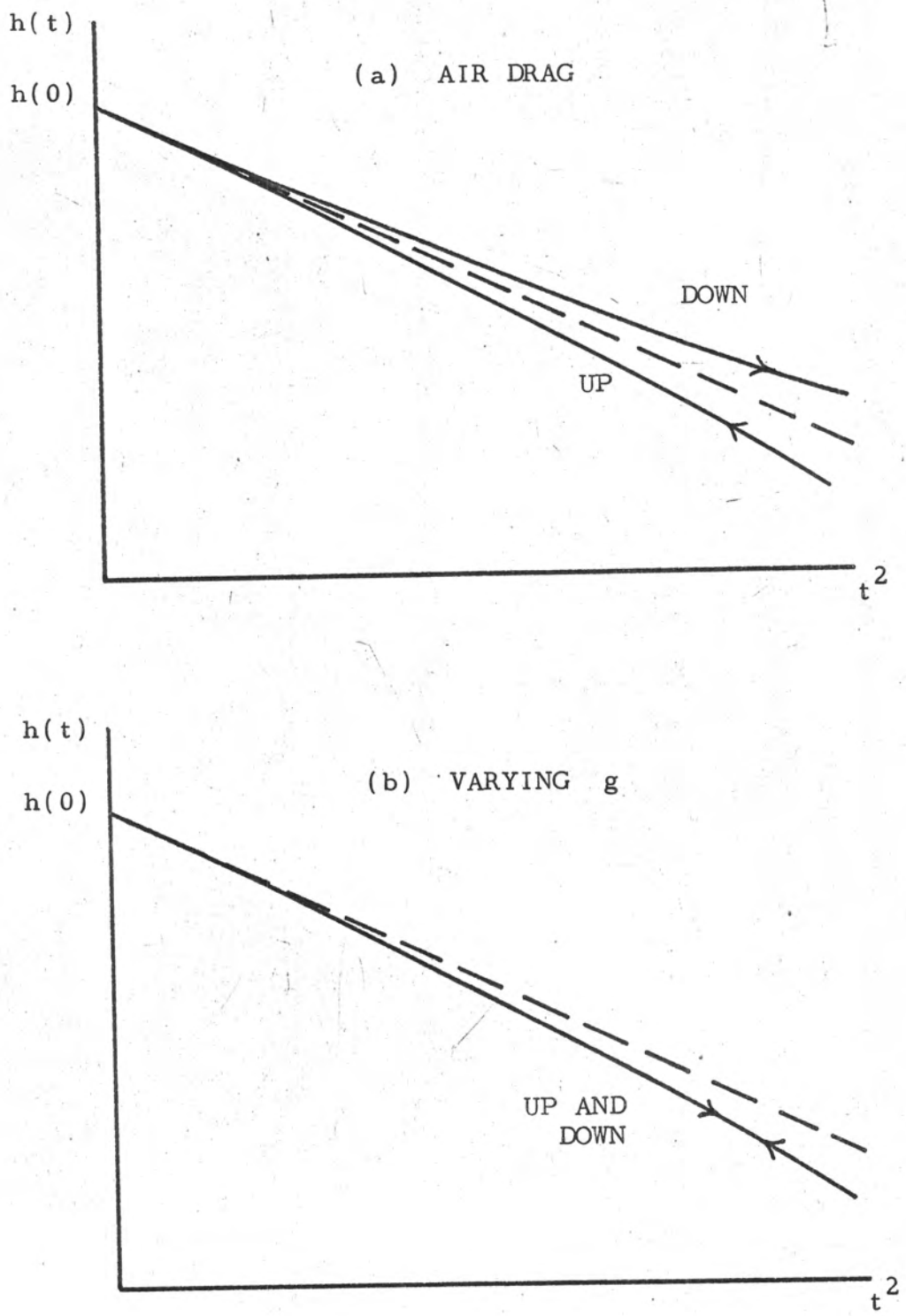

Figure 48. The effects on a rocket trajectory of (a) air drag and (b) varying g. The height h(t) has been plotted against t^2 where t is the time measured from the time of maximum height. The dashed lines represent the trajectory when there is no air drag and g is constant.

In the height range 50 to 90 km the value of k is 2.98×10^{-6} sec^{-2} (U.S. Standard Atmosphere 1962). Because k is small we may to a good approximation put

$$a(t) = -(g_o + \tfrac{1}{2} k g_o t^2)$$

Then

$$v(t) = v(o) + \int_o^t a(t)dt$$

$$= -(g_o t + \tfrac{1}{6} k g_o t^3)$$

and

$$h(t) = h(o) + \int_o^t v(t)dt$$

$$= h(o) - \tfrac{1}{2} g_o t^2 (1 + \tfrac{1}{12} k t^2)$$

It can be seen that the trajectory is symmetrical, i.e. $h(-t) = h(t)$ as shown in Figure 48(b).

As the radar tracking data were missing for the top portion of the flight an analysis had to be performed on the available data to obtain the missing heights. The available data, which were in the form of heights at 1 sec intervals, were first plotted and a smooth curve drawn through them. Some of the points were displaced from the curve by amounts up to 0.12 km indicating that this is the limit of the accuracy of the radar height determination. To determine the time of maximum height the times at which the height was a particular value on the upward and downward portions

of the flight were averaged, for heights spaced 0.75 km apart between 30 and 66 km. At heights above 50 km the mean time was constant, but below this height it showed a steady increase, the effect to be expected if the air drag discussed above were influencing the trajectory (see Figure 48(a)). This showed that the effect of air drag on the HAD rocket may be ignored at heights above 50 km. By averaging the mean times for heights above 50 km a value was obtained for the time of maximum height which was estimated to be accurate to ± 0.01 sec.

The maximum height determined by an analysis of the data from 50 to 85 km on the upward portion of the flight. From the smooth curve the heights were read for times which were an integral number of seconds before the time of maximum height. A tabulation was then made of the quantities

$$x = \frac{h(t) - h(t_0)}{t_0^2 - t^2}$$

where t_0 was the time at which the height was approximately 50 km, the times being measured from the time of maximum height. The average value $\bar{x}$ was then used to calculate the maximum height h(o) using $h(o) = h(t_0) + \bar{x}\, t_0^2$. The value obtained was 91.20 km. However the values of x decreased slightly as t^2 decreased, suggesting the effect of the variation in g discussed above (see Figure 48(b)). Values of the quantity

$$y = \frac{h(o) - h(t)}{t^2(1 + \frac{1}{12} kt^2)}$$

where $k = 2.98 \times 10^{-6}$ sec^{-2} were then tabulated at 1 sec intervals for various values of h(o) close to 91.20 km. It was found that a value h(o) = 91.17 km gave no systematic variation in the values of y whereas there was there was a variation with values of h(o) differing by more than 0.03 km from 91.17 km. Therefore it was concluded that the maximum height was within the range 91.17 ± 0.015 km. The average value of 2y was found to be equal to the value of g at 91.17 km thus providing a check on the calculation.

This analysis showed that above 50 km the trajectory of a HAD rocket is very accurately described by the equation

$$h(t) = h(o) - \tfrac{1}{2} g_o t^2 (1 + 2.48 \times 10^{-7} t^2)$$

where t is the time in seconds measured from the time of maximum height and g_o is the gravitational acceleration at the height h(o). Neglecting the term $2.48 \times 10^{-7} t^2$ does not give rise to significant errors when calculating oxygen densities since even at 70 km it is only about 1×10^{-3} (h(o) ~ 90 km). However its inclusion does allow the maximum height and thus the whole height scale to be determined with high accuracy when the radar tracking is incomplete.

5.5 Analysis of the Aspect Data

Part of the telemetry film record containing the signals from one Lyman-α detector and the pair of aspect sensors (§4.4.2) pointing in the same direction is shown in Figure 49. Between the main peaks in the signals from the aspect sensors, which are due to direct light from the sun, there are smaller peaks due to the earthshine (see §4.4.1(a)). The amplitude of these peaks and their phase relative to the main peaks varied throughout the flight. The presence of the signal due to the earthshine made it difficult to determine the level from which the heights of the main peaks were to be measured, since the level of the earthshine signal directly under the main peaks had to be estimated. This was done by representing the earthshine signal by a sine function whose amplitude and phase relative to the solar signal varied with time. (The form of the earthshine signal at those times during the flight when the rocket aspect angle was 90° was very close to a sine function).

When the heights of the peaks due to direct light were plotted against time it was found that at times when the ratio of the signals from sensors 1 and 2 (see §4.4.2) had a particular value the signals from sensor 1 also had a particular value, for all heights above 40 km. This meant that the signal from sensor 1 was a function of aspect angle only and that absorption of the radiation to which it

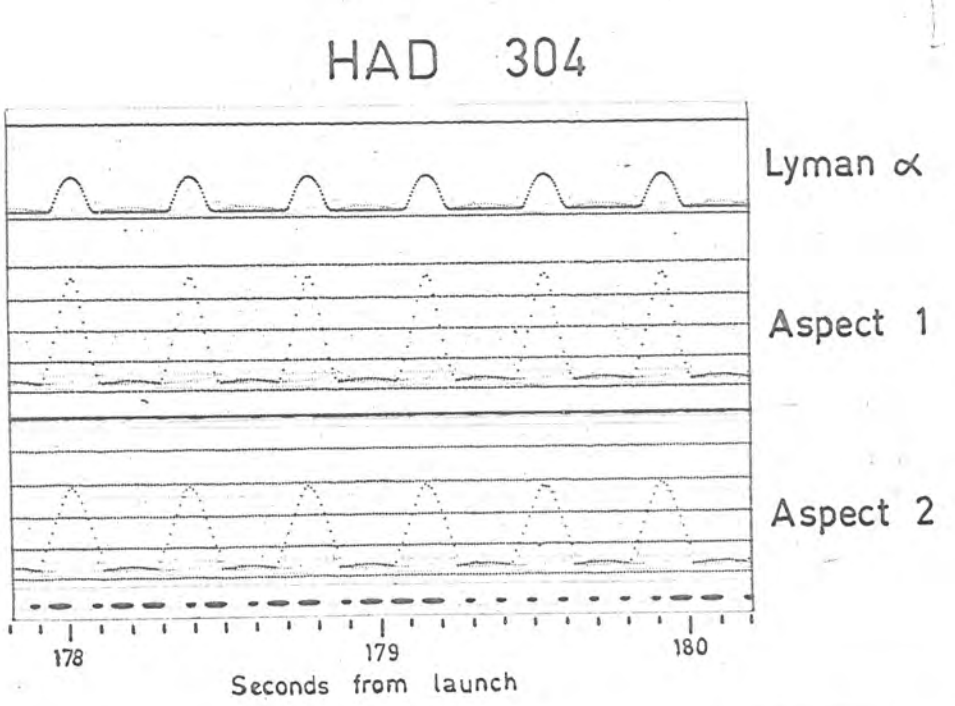

Figure 49. Portion of the telemetry record from HAD 304 showing the signal from one Lyman-α detector and the pair of aspect sensors pointing in the same direction.

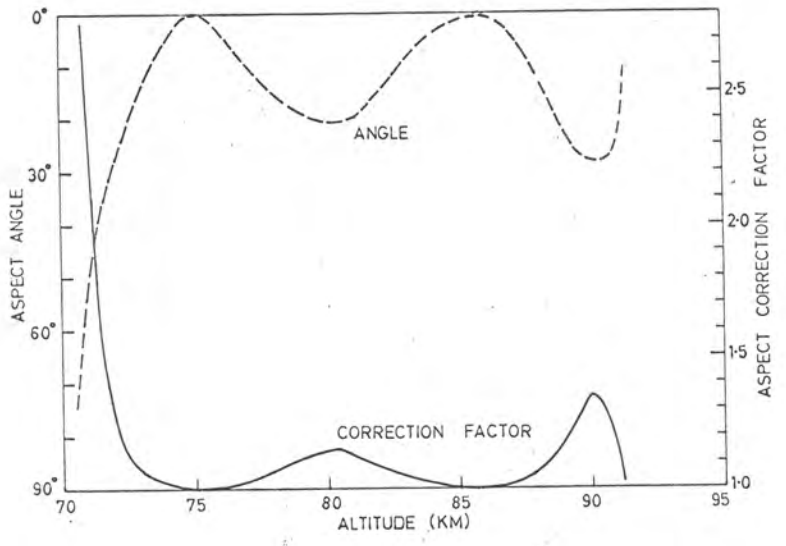

Figure 50. Rocket aspect angle and aspect correction factor plotted against altitude for the downward portion of the flight of HAD 304.

was responding was not significant above 40 km. Thus the signal from sensor 1 alone was used to determine the rocket aspect angle.

The angular response of sensor 1 was known from the calibration made before the flight, but it was necessary to determine the rocket aspect angle at one particular time using the ratio of the signals from the two sensors. The time chosen was one of the three times while the rocket was above 70 km at which the ratio of the signals indicated that the rocket aspect angle was 0°. As well as using the magnitude of the signal from sensor 1 at this time to determine the level of the laboratory calibration, it was also possible to use the signal obtained during one roll of the rocket (after correction for the signal due to the earthshine) to check the angular calibration of the sensor. The two angular response curves agreed very closely. Using the calibration obtained during the flight the rocket aspect angle was determined for the period during which the height of the rocket was between 91.17 and 70 km. This is shown in Figure 50. The angular response of the Lyman-α detector was also determined from the signal obtained during one roll of the rocket when the rocket aspect angle was 0°, and was found to agree well with the calibration made before the flight (see Figure 28). The calibration obtained during the flight was used to derive the correction factor (shown in Figure 50) by which the peak height of the signal from

the Lyman-α detector had to be multiplied to convert it to zero aspect angle. For most of the time during which the height was between 91.17 and 70 km. the correction factor was less than 1.35, but near 70 km the rocket aspect angle rapidly increased to 90° and the correction factor became large.

5.6 The Lyman-α Flux Data

The individual Lyman-α flux measurements, obtained from the peaks in the signals from the Lyman-α detectors, are shown in Figure 51. It can be seen that they form a smooth curve similar in shape to the one shown in Figure 12(b), except for the two lowest measurements where the accuracy was low because of the small peak height and large aspect correction factor.

To obtain the flux values the readings taken from the telemetry film were corrected to zero aspect angle as described in §5.5 and then converted to currents using the calibrations carried out during the flight (§4.3). The currents were then converted to Lyman-α fluxes using the effective area of the detector (1.27 cm^2, see §3.8.2) and the quantum efficiency at Lyman-α as determined before the flight (§3.6.3). It was assumed that the chambers were responding exclusively to Lyman-α radiation. The reasons for this assumption have been discussed in §2.3.3 and are clearly illustrated by Table 9 which shows the contributions

TABLE 9 : Contributions to the signal obtained from a lithium fluoride-nitric oxide ion chamber due to lines other than Lyman-α

Origin of line	Wavelength (Å)	Solar flux ϕ_o (10^9 ph.cm^{-2} sec^{-1}) (1)	Oxygen Absorption cross-section σ (10^{-18} cm^2) (2)	Ion chamber quantum efficiency Y (3)	$e^{-\sigma N(90)}$ (4)	Flux at 90km $\phi=\phi_o e^{-\sigma N(90)}$ (10^9 ph.cm^{-2} sec^{-1})	Relative ion chamber response at 90 km ϕY
C II	1335	6.7	2.7	0.2	~0	-	-
O I	1302-6	3.8	0.46	0.3	0.032	0.12	0.036
SiIII	1261-5	1.9	0.33	0.6	0.084	0.16	0.096
H I	1216	310	0.010	1	0.928	288	288
SiIII	1207	1.8	10.2	1	~0	-	-
C III	1176	0.59	0.72	1	0.0045	0.0027	0.0027

(1) Detwiler et al. (1961b).

(2) Blake et al. (1966).

(3) From Figure 25. Quantum efficiencies are relative to that at Lyman-α.

(4) The value $N(90) = 7.51 \times 10^{18}$ cm^{-2} has been used for the number of oxygen molecules above 90 km (see text).

to the current recorded by a lithium fluoride-nitric oxide chamber at 90 km due to Lyman-α and the other strong lines in the range of the ion chamber. A value of 7.51×10^{18} cm^{-2} has been used for the number of oxygen molecules above 90 km. This value was obtained by integration of the oxygen density profile taken from the U.S. Standard Atmosphere 1962, as shown in Figure 13. From the last column it can be seen that the contribution to the signal recorded at 90 km (and at altitudes less than 90 km) from radiation other than Lyman-α is negligible.

The Lyman-α flux observed at 90 km was 4.2 erg cm^{-2} sec^{-1} which, when multiplied by the factor $\exp(\sigma N(90)\sec z)$, where $\sigma = 1.00 \times 10^{-20} cm^2$, $N(90) = 7.51 \times 10^{18}$ cm^{-2} and $z = 53^\circ$, gives a flux above the atmosphere of 4.7 erg cm^{-2} sec^{-1}. Since one of the ion chambers with which this measurement was obtained was recovered undamaged after the flight the calibration could be checked, and it was found that the quantum efficiency was unchanged. This also provides confirmation of the conclusion reached in §3.11 that the sensitivity of a nitric oxide filled chamber is not altered by exposure to solar radiation for the period of a rocket flight.

5.7 Oxygen Densities

In principle the molecular oxygen density is proportional to the slope of the Lyman-α flux curve shown in

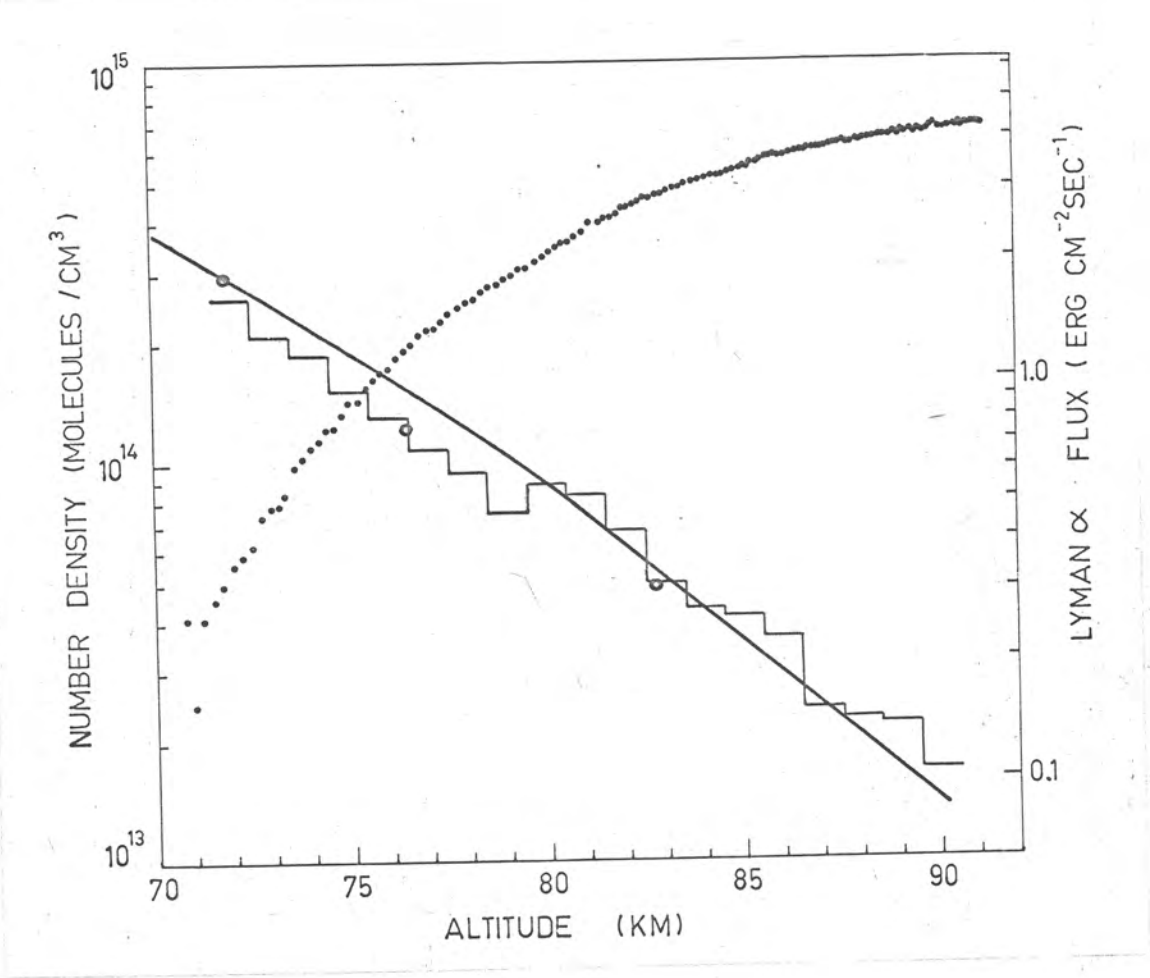

Figure 51. Lyman-α fluxes (solid circles ●) and derived oxygen densities (histogram) from HAD 304. Also shown are the densities from HAD 301 (open circles o) and from the U.S. Standard Atmosphere 1962 (full line).

Figure 51 (equation (7), p.29), but in practice the analysis is best carried out by determining the average densities in a series of equal height intervals. The Lyman-α flux measurements shown in Figure 51 were first averaged over 1 km intervals, to give the values shown in Table 10. These were then used to derive the average oxygen densities over 1 km intervals using equation (1), p.107, and the average density was set equal to the density at the mid-point of the interval, a very good approximation in this case (see footnote p.109). The densities in Table 10 have been plotted in Figure 51 together with the densities obtained from HAD 301 and the densities from the U.S. Standard Atmosphere 1962. The total number densities from the Standard Atmosphere have been multiplied by 0.209 to obtain the molecular oxygen number densities (see Table 2, p.23).

The main source of error in the densities lies in the aspect correction factor, but the uncertainty is much less than in the case of the densities from HAD 301. The rise in density at 80 km is probably due to error in the aspect correction factor at this altitude (see Figure 50) resulting in a slight depression of the Lyman-α flux values near 80 km.

5.8 Absorption of Lyman-α by Gases other than Oxygen.

When deriving the oxygen densities given in §5.2 and §5.7 it was assumed that the solar Lyman-α radiation was absorbed by molecular oxygen only. In this section the

TABLE 10 : Oxygen Densities from HAD 304

Height h (km)	Lyman-α flux $\phi(h)_{L_2}$ (erg cm^{-2} sec^{-1})	Height h' (km)	O_2 number density n(h') (cm^{-3})
71.5	0.2505	72	2.58×10^{14}
72.5	0.3872	73	2.04
73.5	0.5458	74	1.85
74.5	0.745	75	1.51
75.5	0.958	76	1.28
76.5	1.188	77	1.05
77.5	1.415	78	9.33×10^{13}
78.5	1.651	79	7.40
79.5	1.870	80	8.72
80.5	2.161	81	8.24
81.5	2.481	82	6.70
82.5	2.779	83	4.92
83.5	3.012	84	4.26
84.5	3.235	85	4.08
85.5	3.460	86	3.59
86.5	3.678	87	2.38
87.5	3.826	88	2.22
88.5	3.970	89	2.19
89.5	4.115	90	1.63
90.5	4.226		

TABLE 11 : Absorption of Solar Lyman-α by various Atmospheric Constituents

Constituent	Cross-section σ/σ_{O_2} (1)	Number density n/n_{O_2} (2)	Absorption relative to oxygen $\sigma n/\sigma_{O_2} n_{O_2}$
O_2	1	1	1
N_2	$<6\times10^{-3}$	3.73	<0.022
CO_2	7.4	0.0015	0.011
O_3	2.3×10^{3}	2.9×10^{-6} - 5.5×10^{-6}	0.0067 - 0.0126
H_2O	1.4×10^{3}	2.7×10^{-5} - 7.6×10^{-7}	0.038 - 0.0010
NO	2.7×10^{2}	1.6×10^{-7} - 4.3×10^{-6}	4.3×10^{-5} - 0.0012

(1) Cross-sections at Lyman-α are relative to that of oxygen, taken as 1.00×10^{-20} cm^2. The values are those quoted in §2.1.

(2) Densities are relative to that of oxygen. The values for N_2 and CO_2 are taken from Table 2 (p.23). For the others the values are taken from the sources quoted in the text and are relative to the oxygen densities in the U.S. Standard Atmosphere, the first value being that at 70 km and the second that at 90 km.

magnitude of the absorption due to other atmospheric constituents will be considered. Since all the other constituents except nitrogen have higher absorption cross-sections at Lyman-α than oxygen (see Table 11) even small concentrations of these constituents may make some contribution to the absorption of Lyman-α. The absorption

due to each constituent, σn, will be expressed as a fraction of the absorption due to oxygen, $\sigma_{O_2} n_{O_2}$. The results of the calculations are presented in Table 11.

(a) Nitrogen

The lowest upper limit to the cross-section of molecular nitrogen at Lyman-α is 6×10^{-23} cm^2 (§2.1) and using this the absorption due to nitrogen is less than 2% of that due to oxygen (Table 11).

(b) Carbon dioxide.

No experimental evidence is available concerning the concentration of carbon dioxide in the 70 to 90 km region, but Bates and Witherspoon (1952) have concluded that the rate of photo-dissociation of carbon dioxide is appreciable only above 100 km so it seems likely that the fraction of carbon dioxide in the air is constant up to 90 km. In this case the absorption due to carbon dioxide is 1.1% of that due to oxygen (Table 11).

(c) Ozone.

Two experimental determinations of ozone profiles up to 70 km have been made using rockets (Johnson et al. 1952, L'vova et al. 1964), and one determination of the profile up to 90 km has been made using a satellite (Rawcliffe et al. 1963). These profiles are shown in Figure 52, together with theoretical profiles due to Johnson et al. (1952), Barth (1961) and Hunt (1965). There is reasonable agreement at

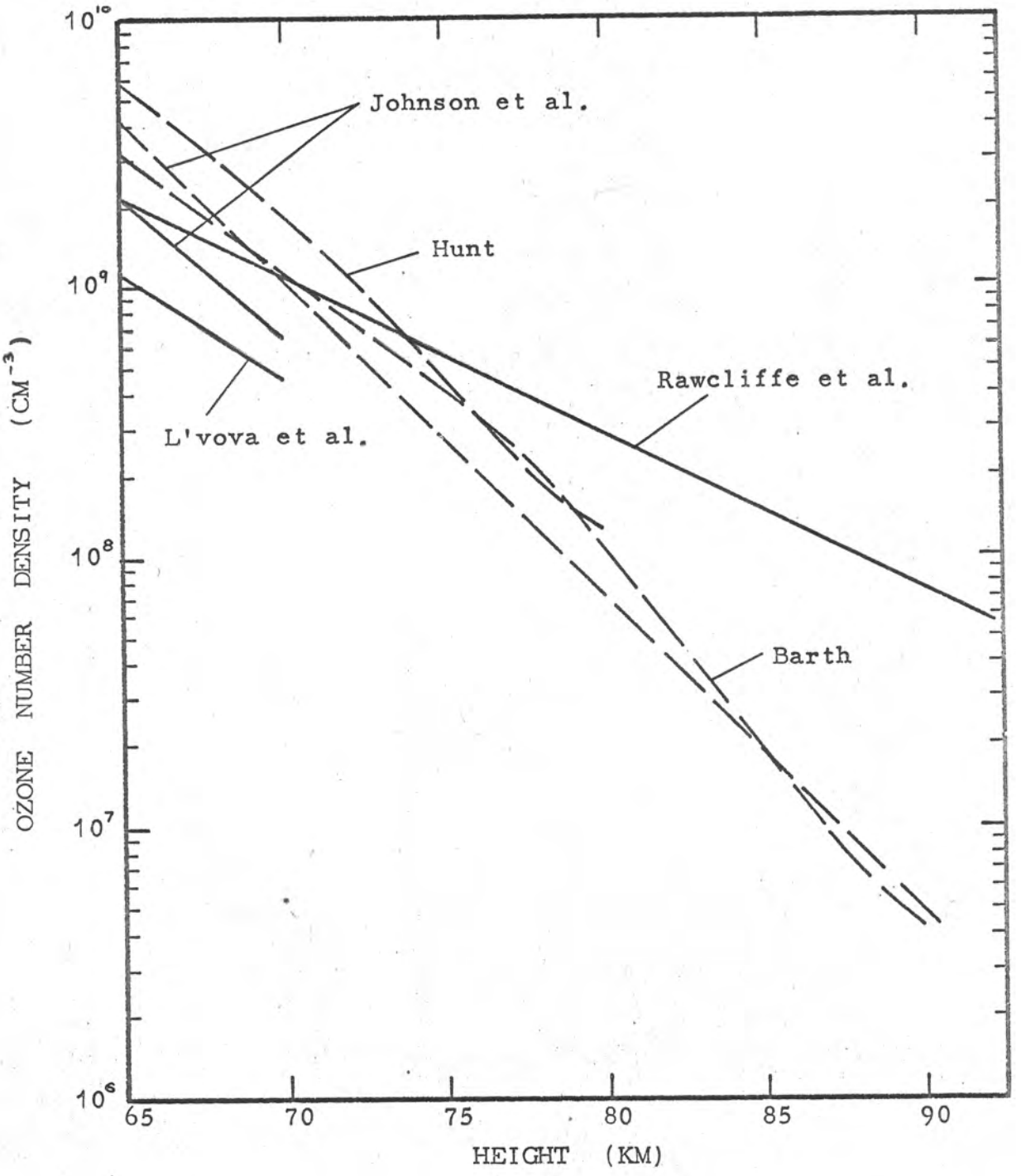

Figure 52. Experimental ozone profiles (full lines) due to Johnson et al. (1952), L'vova et al. (1964) and Rawcliffe et al. (1963) and theoretical profiles (dashed lines) due to Johnson et al. (1952), Barth (1961) and Hunt (1965).

70 km although the theoretical profiles all lie above the experimental ones, but above 70 km the experimental profile gives considerably higher concentrations than the theoretical ones. Taking the profile of Rawcliffe et al., which probably represents an upper limit, the absorption due to ozone varies from 0.67% (at 70 km) to 1.26% (at 90 km) of that due to oxygen (Table 11).

(d) Water Vapour.

As in the case of carbon dioxide there have been no experimental determinations of water vapour concentrations above 30 km, but Bates and Nicolet (1950) have derived a theoretical profile from an analysis of the photochemistry of a hydrogen-oxygen atmosphere.

It has been suggested that the presence of noctilucent clouds may have some bearing on the concentration of water vapour in the mesosphere. The clouds occur at heights near 80 km, mainly in the summer at latitudes above 45°, and it has been established (Hemenway et al. 1964) that they consist of dust particles of extra-terrestial origin, many of which are coated with a layer of ice. The presence of the ice on the cloud particles cannot, however, be taken to mean that the air is always saturated in the 80 km region. To produce a frost point equal to the minimum temperature at the mesopause at high latitudes in summer a mixing ratio for the water vapour of 0.5 gm/kgm would be required (Hesstvedt

1962, Newell 1963) and water vapour in this concentration would produce five times the observed absorption of Lyman-α. Chapman and Kendall (1965) have made an analysis of the conditions which lead to the formation of noctilucent clouds, and they conclude that the water vapour is carried to the 80 km region by convection at night and there condenses on the descending dust particles. It must be assumed that such an occurrence is rare in order to account for the infrequent appearance of the noctilucent clouds.

Obviously there is still much uncertainty concerning the concentration of water vapour in the 70 to 90 km region, but for the present it seems best to assume that during the day, at low latitudes, the water vapour concentration is as given by Bates and Nicolet, even though they would not rely on the quantitative accuracy of their distribution, and the time for photochemical equilibrium is several days. On this basis the absorption due to water vapour, relative to that due to oxygen, is 3.8% at 70 km, 0.57% at 80 km and 0.10% at 90 km (Table 11).

(e) Nitric Oxide.

Barth (1965) has recently determined experimentally the concentration of nitric oxide in the 70 to 90 km region and found it to be about 6×10^7 mols cm^{-3}. This is considerably higher than previous theoretical estimates, but, from Table 11, it can be seen that even at this

concentration nitric oxide produces negligible absorption of the Lyman-α radiation.

From the figures given in Table 11 it must be concluded that the contribution to the absorption of Lyman-α due to constituents other than oxygen is not more than several percent, the exact contribution being uncertain owing to uncertainty concerning the concentrations of the minor constituents, particularly water vapour. In the present work no corrections have been made for absorption due to constituents other than oxygen. It may be noted that as suggested by Chubb et al. (1958) the absorption of Lyman-α could be used to determine the water profile in the 70 to 90 km region if the oxygen profile were sufficiently accurately known, but the Lyman-α absorption measurements would have to be accurate to about 1% since the fraction of the absorption due to water vapour is much less than supposed by Chubb et al. (see p.43).

5.9 Temperature Profile

The oxygen densities given in Table 10 were used to derive temperature profiles for the region 70 to 90 km, making the assumption that mixing prevailed in this region, and using equation (6), p.40. The integration was carried out at intervals of 1 km. Two values for the temperature at 90 km were assumed: (1) 181°K, as given by the U.S. Standard Atmosphere 1962, and (2) 155°K as given by falling

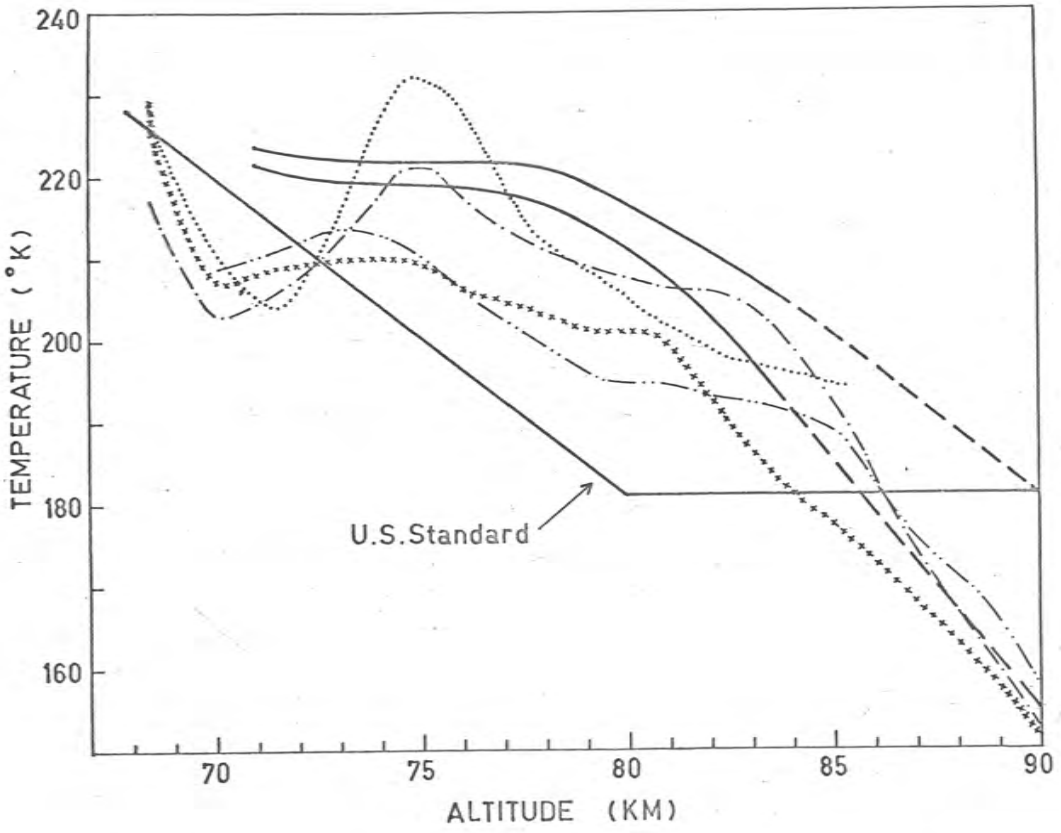

Figure 53. Temperature profiles derived from the HAD 304 oxygen densities for assumed temperatures at 90 km of (1) 181°K (U.S. Standard Atmosphere 1962) and (2) 155°K (Woomera falling sphere data). Also shown are temperature profiles obtained from falling sphere measurements at Woomera (Rofe 1965 unpublished) at the following times: November 1964 (—·—·—), December 1964 (·····) and March 1965 (××××××× and —··—··—). The temperature profile from the U.S. Standard Atmosphere 1962 is shown for comparison.

sphere measurements at Woomera (Rofe 1965 unpublished). The resulting temperature profiles are shown in Figure 53, together with four derived from the falling sphere measurements, and that of the U.S. Standard Atmosphere 1962. Errors in the density values are magnified when the densities are used to calculate a temperature profile, so the density values were smoothed before calculating the temperatures. The probable error was estimated to be 5°K.

5.10 Discussion

5.10.1 Oxygen Densities.

The oxygen densities obtained from the present work are displayed in Figure 13 together with the results of other workers. There is good agreement between the two sets of results obtained in the present work, which is to be expected since the measurements were both made in summer, and at nearly the same time of day.

Seasonal variations of the atmospheric temperature and density in the height range 30 to 80 km have been studied by Kantor and Cole (1965). The results analysed were obtained using various methods of measuring temperature, total pressure and total density. Figure 54 shows the model they obtained. The densities are plotted as percentage deviations from the U.S. Standard Atmosphere 1962. At all latitudes the density is highest in summer and lowest in winter, the magnitude of the variation increasing as the latitude increases. Figure 55 shows the oxygen

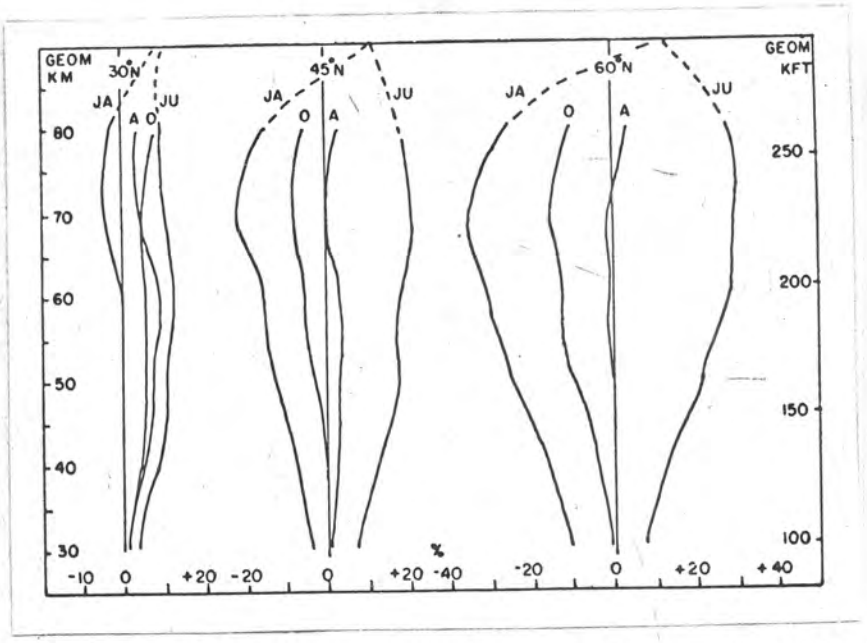

Figure 54. Model for seasonal variation of atmospheric density obtained by Kantor and Cole (1965). Densities are plotted as percentage deviations from the U.S. Standard for winter (JA), spring (A), summer (JU) and autumn (O).

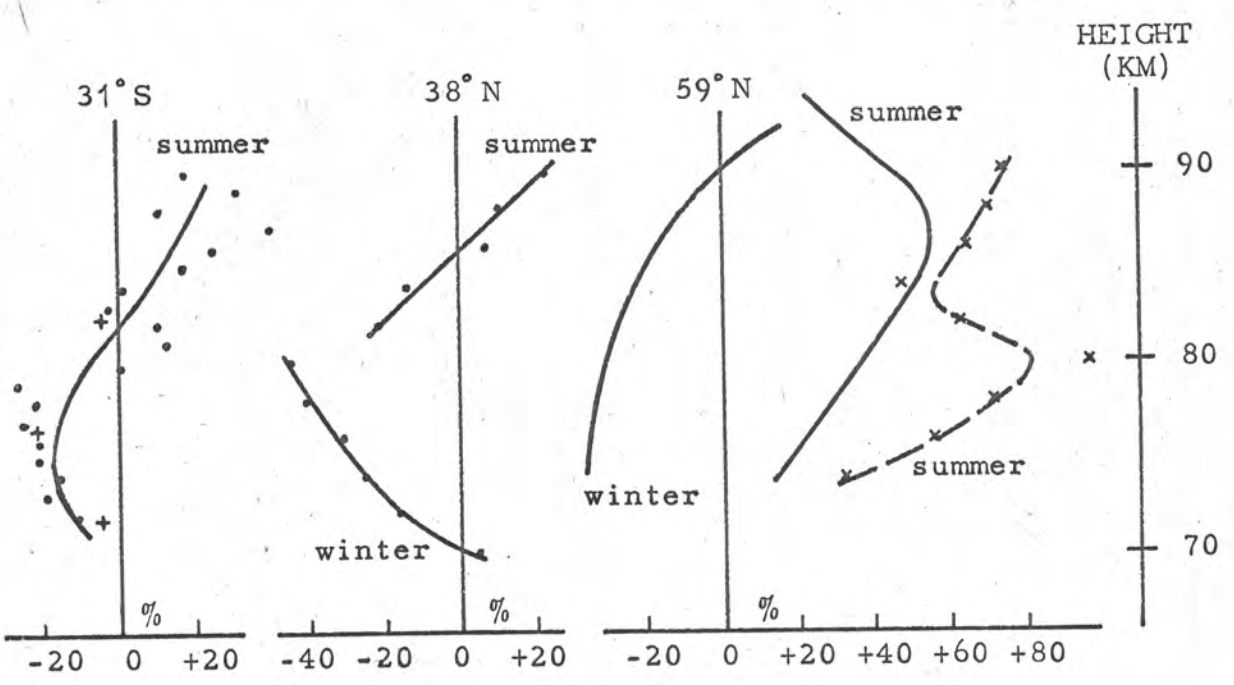

Figure 55. Oxygen densities of Kupperian et al. (1952) (59°N, full lines), Smith and Weeks (1965) (38°N, and 59°N, crosses ×) and the present work (31°S, HAD 301 +, HAD 304 •) plotted as percentage deviations from the U.S. Standard.

densities of Kupperian et al. (1959)*, Smith and Weeks (1965), and the present work plotted in the same way. Since there is mixing in the atmosphere at heights up to about 90 km the oxygen density will be proportional to the total density. The results of Kupperian et al. agree well with the model in the magnitude of the variation, but they suggest that the mean annual density is less than the Standard at heights below about 80 km, whereas the model shows it to be equal to the Standard. The results of the present work also imply that the mean density is less than the Standard below about 80 km if it is assumed that the density in summer is about 10% higher than the mean density, as concluded by Kantor and Cole. The results of Smith and Weeks at 59°N show wide variations in their departure from the Standard which are difficult to accept as real variations in density because of the very rapid changes of temperature with height which they imply. Their results at 38°N do not cover the same height range so it is difficult to derive any conclusion concerning the seasonal variation at this latitude. From Figure 55 the probable error in the densities obtained from the present work is estimated to be about 7%.

---

*The densities of Kupperian et al. have been adjusted to an absorption cross-section for molecular oxygen at Lyman-α of 1.00×10^{-20} cm^2 (see footnote p.44).

5.10.2 Temperatures.

Temperatures derived from the present work (Figure 53) are higher than those of the Standard Atmosphere as would be expected from the greater scale height indicated in Figure 55 for these results. There is quite close agreement with the two summer temperature profiles obtained at Woomera by Rofe (unpublished) using the falling sphere method (Figure 53). The Standard Atmosphere is based mainly on Northern Hemisphere results so the results obtained at Woomera may indicate a significant difference between the Northern and Southern Hemisphere temperatures.

5.10.3 Lyman-α Intensities.

Table 12 shows the results of the measurements of the intensity of the solar Lyman-α line which were described in §1.1. All the measurements were made using ion chambers except those of Hinteregger et al., where a photoelectric monochromator was used. The errors given for the present work represent the estimated uncertainties in the calibration and in the rocket data. Smith et al. used chambers filled with carbon disulphide so this may account for the fact that their value is lower than any other (see §3.12) in spite of the relatively small error they have given. It is of interest to examine the Lyman-α results for any evidence of variation related to the 11 year solar cycle. The last sunspot maximum was in 1958

TABLE 12 : Lyman-α intensity measurements

Lyman-α flux (erg cm^{-2} sec^{-1})	Time of measurement	Reference
5.5 - 6.0	1959-61	Kreplin et al. (1962)
$3.0 \begin{smallmatrix} + 2.6 \\ - 1.6 \end{smallmatrix}$	-	Willmore (1961)
4.4 ± 1.5	1961-63	Hinteregger et al. (1965)
2.4 ± 0.24	1963	Smith et al. (1965)
5.4 ± 0.8	1963	Present work, HAD 301
4.7 ± 0.2	1965	Present work, HAD 304

and the last minimum in 1964. A variation from about 5.7 erg cm^{-2} sec^{-1} at solar maximum to about 4.7 erg cm^{-2} sec^{-1} at solar minimum would be consistent with all the data in Table 12 except that of Smith et al. This suggests that the solar Lyman-α intensity does not vary more than about ±10% over the solar cycle, a variation considerably less than the ±33% suggested by Smith et al.

Chapter 6. Statistics of Electron Multiplication in Proportional Counters.

6.1 Introduction

If the voltage applied to a cylindrical ion chamber is increased sufficiently electron multiplication takes place by secondary ionization near the wire (§3.10). The process is the same as that occurring in the proportional counter used for detecting x-rays and nuclear radiations. Each primary electron released in the gas gives rise to an avalanche of secondary electrons which are collected at the wire and under suitable conditions may be detected as an electric pulse. In the case of the ultra-violet ion chamber these pulses enable the arrival of single photons in the chamber to be detected, thus providing a very sensitive detector. However, the number of electrons in the avalanche is subject to very large statistical fluctuations, a problem which can be overcome by operating the detector as a Geiger counter (Chubb and Friedman 1955). The Geiger counter has disadvantages compared with the proportional counter, however, such as the need to quench the discharge, the long dead time, and the rapid destruction of the filling.

When the proportional counter is used for the detection of nuclear radiations the fluctuations in the size of the individual avalanches are less serious since

a number of primaries are released simultaneously, and under these conditions the relative fluctuation in the total number of secondary electrons is reduced (e.g. West 1953). However when the number of primaries becomes smaller, as in the detection of soft x-rays, the fluctuations in the multiplication process make an increasing contribution to fluctuations in the total number of secondaries and cause a reduction in the energy resolution of the counter. (Fluctuations in the number of primaries produced by x-rays of a given energy also become more serious as the energy of the x-rays decreases). Curran and Wilson (1965) have stressed the need for greater knowledge of the fluctuations in avalanche size and the factors which control them.

6.2 Notation

The following notation will be used throughout this chapter.

V = voltage applied to counter.

E = electric field strength.

r = radial distance from axis of counter

W = ionization potential of a molecule.

α = Townsend ionization coefficient (average value for electrons in equilibrium with the field).

a = effective ionization coefficient.

n = number of electrons in an avalanche.

x = pulse size (x is proportional to n).

$\bar{x}$ = mean pulse size.

$z = x/\bar{x}$ = reduced pulse size.

y = frequency distribution function. (y is proportional to the probability distribution function ϕ, defined so that the probability of the pulse height lying in the range x to x + dx is $\phi(x)dx$).

$D = -\frac{d}{dx}(\ln y) = -\frac{1}{y}\frac{dy}{dx}$ = negative logarithmic derivative.

6.3 Previous Investigations of Avalanche Statistics.

Several authors have made theoretical and experimental investigations of the form of the frequency distribution y under various conditions.

The simplest way of treating the problem theoretically is to assume that the probability, per unit distance travelled, of an electron making an ionizing collision, a, is the same for all electrons at a particular distance from the wire and is equal to $\alpha = f(r)$. Then it can be shown (Wijsman 1949, Legler 1955, Frisch 1959, Franzen and Cochran 1962) that the distribution has the form

$$P(n, \bar{n}) = \frac{1}{\bar{n}}\left(1 - \frac{1}{\bar{n}}\right)^{n-1} \qquad n = 1,2,3,\ldots$$

where $P(n,\bar{n})$ is the probability of an avalanche containing n electrons at the point where the average number of electrons in an avalanche is $\bar{n}$. This is known as the Furry distribution. In practice the avalanche size is measured as a pulse height x and owing to noise in the amplifier used

to amplify the pulses the minimum values of x which can be measured correspond to values of n of several thousand. Under these conditions ($\bar{n}$, n large) we have*

$$y = \exp(-\frac{x}{\bar{x}}) = \exp(-z)$$

where y is the frequency distribution function and x the pulse height.

Curran et al. (1949) analysed the pulse spectrum obtained when single photoelectrons were ejected from the wall of a proportional counter filled with a mixture of argon and methane (each to a pressure of 250 torr). The spectrum departed from the exponential distribution at small values of n, and y showed a maximum at $x \sim \frac{1}{3}\bar{x}$. Curran et al. found that the distribution had approximately the form

$$y = z^{\frac{1}{2}} \exp(-\frac{3z}{2}).$$

Schlumbohm (1958) has recorded spectra for fillings of methane, methane and argon mixed in equal parts, and methylal, at various pressures and with various wire diameters. He found both exponential distributions and distributions which deviated from the exponential at low values of x in a manner similar to those of Curran et al.

---

* Un-normalized frequency distributions rather than probability distributions will be used throughout this section since the normalizing constant has no physical significance.

Following a suggestion of Legler (1955) Schlumbohm was able to relate the deviation from the exponential distribution to the value of $\frac{E}{\alpha}$ at the commencement of the multiplication. Legler pointed out that the assumption that the effective ionization coefficient a is the same for all electrons at a particular point ignores the fact that either one or both the electrons coming from an ionizing collision may not have sufficient energy to ionize. However the assumption will be a good approximation when the distance $\frac{W}{E}$ which an electron has to travel in the direction of the field in order to gain sufficient energy to ionize is small compared with $\frac{1}{\alpha}$, the average distance between ionizing collisions i.e. $\frac{1}{\alpha} >> \frac{W}{E}$ or $\frac{E}{\alpha} >> W$. As $\frac{E}{\alpha}$ decreases the distribution may be expected to deviate increasingly from the exponential. In the proportional counter $\frac{E}{\alpha}$ is a function of position since it depends on $\frac{E}{p}$ (Legler 1955), but Schlumbohm has pointed out that it is the value of $\frac{E}{\alpha}$ at the commencement of the multiplication which is relevant since the form of the distribution is determined by the distribution at the point where $\bar{n} \approx 100$, and further multiplication merely amplifies all avalanches by the same factor, just as in the case where the avalanche is initiated by a number of primaries.* Using experimental

*This statement is not strictly correct since the avalanches which are small at the point where $\bar{n} \approx 100$ will still be subject to the statistical fluctuations. This point will be discussed further below (p. 149).

determinations of $\frac{E}{\alpha}$ for the fillings he was using Schlumbohm showed that the deviation from the exponential distribution increased as the value of $\frac{E}{\alpha W}$ at the commencement of the multiplication decreased.

Legler (1961) has analysed the situation where $\frac{W}{E}$ is comparable with $\frac{1}{\alpha}$ by considering a model gas in which the effective ionization coefficient $a(\xi)$ is a function of the distance ξ which the electron has travelled since its last ionizing collision. In the model $a = o$ for $o \leqslant \xi < x_o$ and $a = \text{const.}$ for $n_o \leqslant \xi$. The parameter x_o is to be identified with $\frac{W}{E}$. The resulting equation for the distribution function could not be solved exactly but it was integrated numerically for various values of αx_o in the range 0 to 0.25 giving the distributions shown in Figure 60(b). Legler showed that these distributions fitted quite well experimental distributions obtained with a uniform electric field when x_o was set equal to the value of $\frac{W}{E}$.

Byrne (1962) has also modified the simple theory which leads to an exponential distribution. He assumed that a was a function both of r and n having the form

$$a = f(r)(1 + \frac{k}{n})$$

where k was a parameter lying in the range $o < k$. (Since $a = f(r)(1 + k)$ for $n = 1$ and $a = f(r)$ for very large n the fraction of the electrons which can ionize when n is large is $\frac{1}{1+k}$). The decrease of a with increasing n, when

n is small, is associated with the fact that after an ionizing collision (which increases n) the two electrons coming from the collision will have an average energy less than that of the ionizing electron, so a will be reduced. This effect will be important when the average energy gained between ionizing collisions $\frac{E}{a}$ is not too large compared with W, so Byrne's assumption will apply under the same conditions as were considered by Legler. With the form for a given above the number of secondary electrons is distributed according to a Polya distribution, which for large $\bar{n}$ tends towards the Pearson III form

$$y = z^k \exp[-(k + 1)z]$$

This function has been plotted in Figure 60(a) for several values of k and it can be seen that it is strikingly similar to the form obtained by Legler using a more detailed analysis of the variation of a. Thus Byrne's convenient analytic representation of the distribution may be taken as representing both theories.

Schlumbohm (1958) also observed distributions in which y deviated above the exponential form at large values of n. This was ascribed to the effect of "successors" or avalanches initiated by electrons ejected from the cathode by photons produced in the first avalanche. If the time interval between the two avalanches is shorter than the integrating time of the amplifier used to amplify the

pulses the two avalanches will be observed as a single pulse. Legler (1964) has analysed the statistics of series of avalanches formed in this way, making the assumptions that the distribution for a single avalanche is exponential and that the probability y that a single electron in an avalanche will give rise to a successor is very small. Then the distribution for the total size of the avalanche chain is

$$y = \frac{I_1(bz)}{bz} \exp(-cz)$$

where $b = \frac{2\sqrt{\mu}}{1-\mu}$, $c = \frac{1+\mu}{1-\mu}$, μ is the average number of successors initiated by one avalanche and I_1 is the modified Bessel function of order 1. Figure 60(c) shows this function plotted for several values of μ.

Since the investigations of Curran et al. and Schlumbohm had been made with only a few fillings it seemed useful to extend the measurements to other filling gases. At the same time the availability of a multi-channel analyser made it possible to cover a wide range of frequencies in each distribution since with a capacity of 10^3 counts per channel a frequency range of about 3 decades can be covered. None of Schlumbohm's distributions extended for more than about $1\frac{1}{2}$ decades.

6.4 Apparatus

The counter used is shown in Figure 56. It was constructed from 25 mm diam copper tubing with a glass-to-

Figure 56. Photograph of the proportional counter.

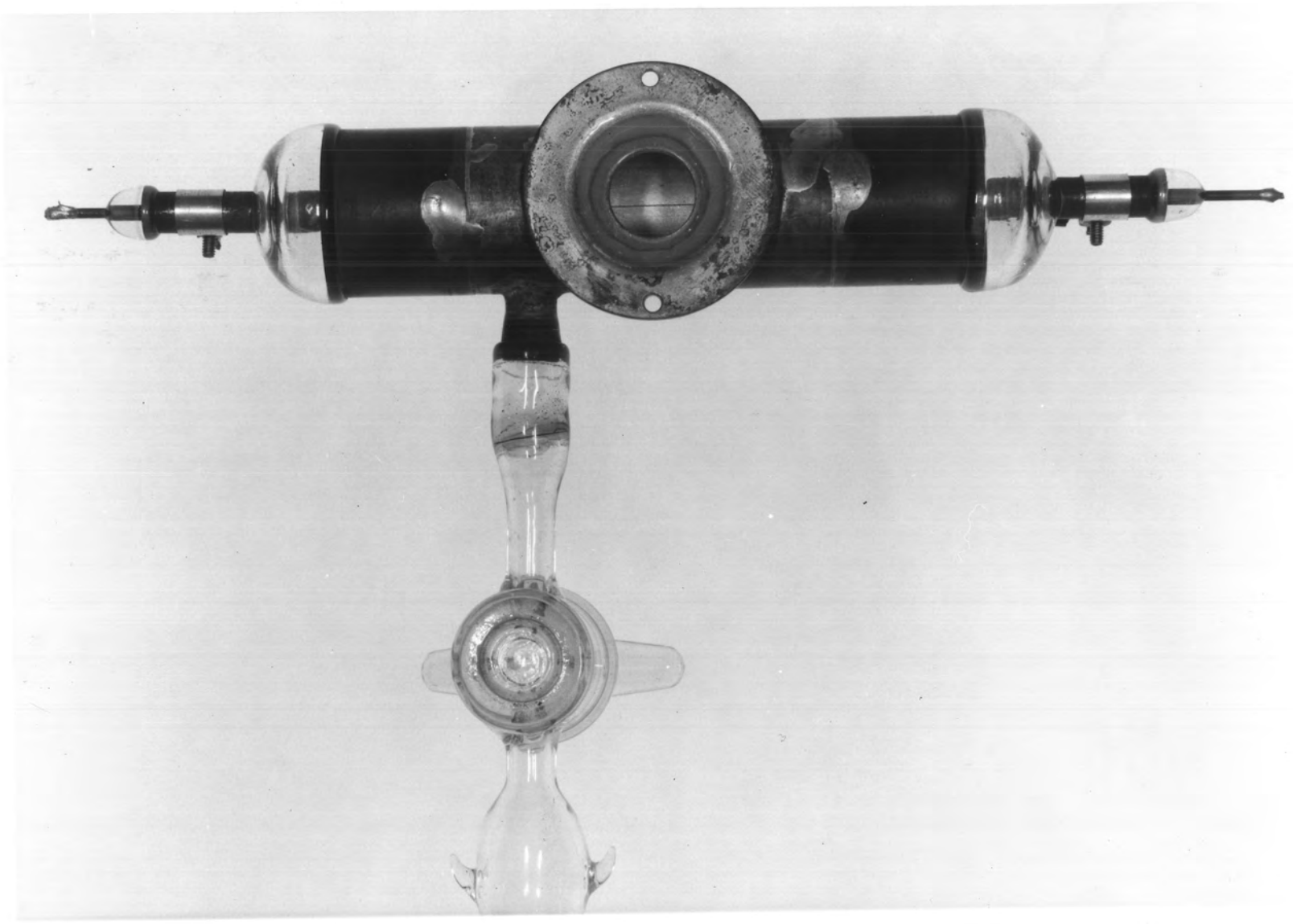

metal seal containing a guard ring soldered to each end. The wire was 0.1 mm diam tungsten. A lithium fluoride crystal of the same kind as those used on the ion chambers was used for the window. So that the chamber could be easily refilled a glass tap and socket were attached.

When recording spectra the counter was placed in an earthed aluminium box to prevent stray radiation from increasing the noise level of the amplifier. A negative voltage was applied to the case of the counter and the wire was connected directly to the input of the amplifier as shown in Figure 57. Because of the nature of the pulse spectrum there will always be present some very large pulses so it is desirable to use a pulse amplifier with rapid recovery after overloading pulses. A double delay-line amplifier (Franklin 358) with a 1μ sec clipping time was used in the present work. The input circuit of the preamplifier was modified as shown in Figure 57. A 10 MΩ resistor was inserted to maintain the D.C. level of the counter wire at earth potential, and a condenser C was inserted so that the charge sensitivity of the amplifier could be determined. This calibration (Gillespie 1953) was carried out by passing a pulse of known size V into the input of the preamplifier through the condensor C, the capacity of which (0.85 pF) had previously been measured. Provided that C is small compared with the total input

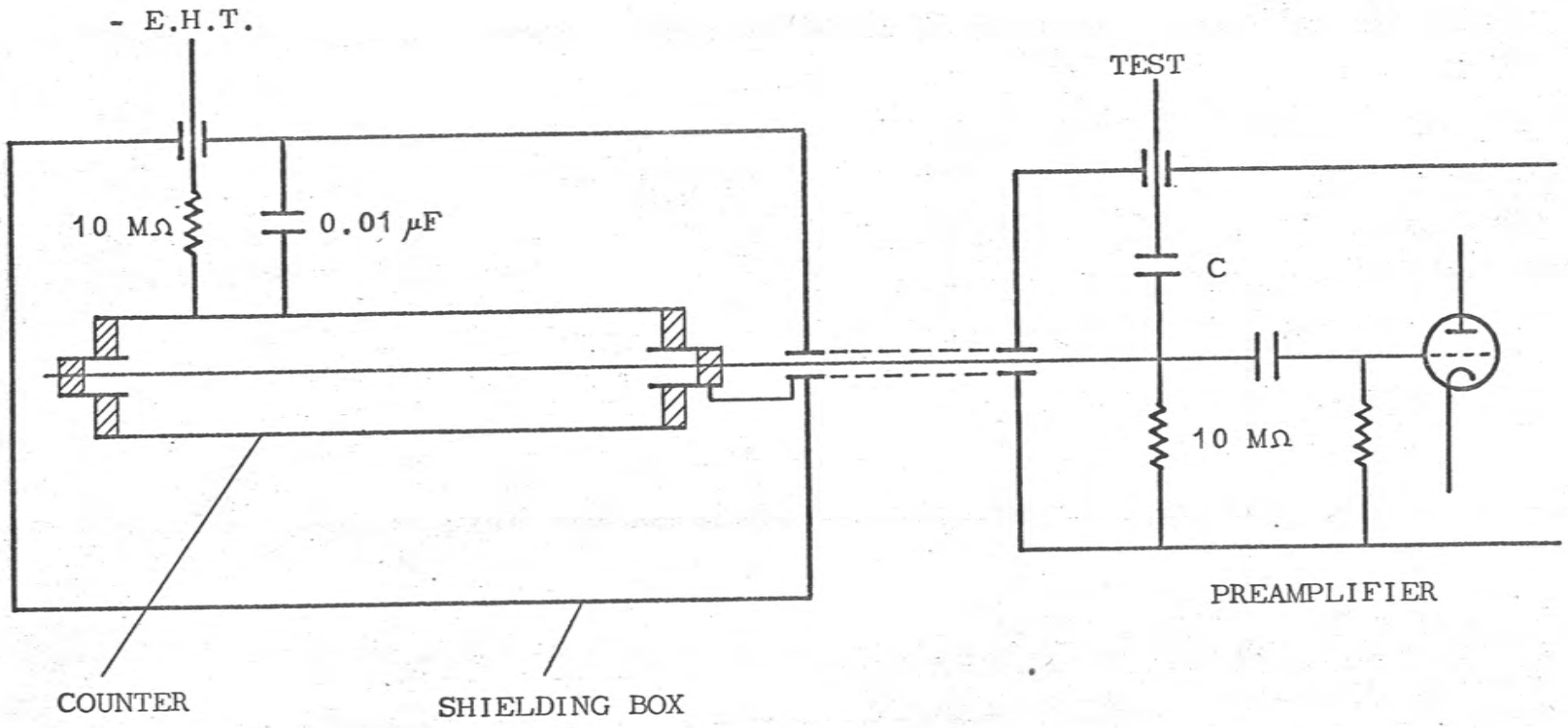

Figure 57. Diagram of the proportional counter and the input circuit of the preamplifier.

capacity of the preamplifier (50 pF in this case) the charge delivered to the preamplifier is Q = CV. The test pulses were obtained from a mercury relay pulse generator.

The output pulses from the amplifier were analysed in a 400 channel pulse analyser (RIDL 34-12B). The linearity and zero of the amplifier and analyser were determined by applying pulses of various amplitudes from the pulse generator to the input of the preamplifier and recording the channel in which they were stored. There were no deviations from linearity greater than 0.3%. The portable hydrogen lamp described in §3.5 was used as a source of ultra-violet light with which to release the primary electrons within the counter. It was attached to the side of the shielding box by a mounting which could be flushed with nitrogen in order to admit the vacuum ultra-violet radiation to the counter. In this way it was possible to eject photoelectrons from the filling gas as well as from the cathode. However it was found by placing a quartz window between the lamp and the counter that the shape of the spectrum did not depend on the source of the electrons.

The counter was evacuated and filled on the vacuum system described in §3.3.1, the filling pressures being measured with the mercury barometer. Mixtures of carbon dioxide in argon and methane in argon were obtained as mixtures, the composition having been determined by an

analysis carried out by the manufacturer. The mixtures of acetone in argon and alcohol in argon were prepared in the vacuum system using spectroscopically pure argon.

6.5 The Measurements.

The fillings used and the range of voltages over which spectra were recorded are shown in Table 13. In addition fillings of nitric oxide (57 torr) and 3.1% carbon dioxide in argon (257 torr) were used, but the pulses obtained with these fillings were very irregular in shape when observed with an oscilloscope and showed clearly the effects of successors occurring 0.1 to 0.5 μ sec after the main pulse. Because of the irregularity in pulse shape no spectra were recorded with these fillings.

TABLE 13. Proportional Counter Fillings and Voltages

Filling	Pressure (torr)	Voltage range
acetone	11	1175-1287
alcohol	10	1000-1125
alcohol	35	1250-1450
methylal	21	1000-1300
acetone 15% + argon 85%	97	1400-1450
alcohol 3.7% + argon 96.3%	187	1300-1400
methane 9.5% + argon 90.5%	500	2300-2550

All the spectra were recorded with the same amplifier gain and analyser sensitivity so the overall sensitivity was the same for all spectra, and was found using the

calibration procedure described in §6.4 to be 6.5×10^3 electrons per channel. The intensity of the radiation from the lamp was adjusted so that the dead time of the analyser was always less than 8%. Spectra were usually recorded until the count numbers in the lower channels (excluding those occupied by noise) reached about 10^5 counts, the capacity of the analyser. Times used for recording the spectra varied from about 10 min to 3 hr depending on the shape of the spectrum. Noise occupied channels up to number 3 (which corresponded to 2×10^4 electrons) so the spectra were analysed only for channels 4 and above.

For each filling, spectra were recorded at a number of voltages ranging from the voltage where the pulses first appeared above the noise to the voltage where either the counter began to act as a Geiger counter (in the case of the acetone, alcohol 35 torr, acetone-argon and alcohol-argon fillings) or intermittant breakdown began to occur (in the case of the other fillings).

The spectra are shown in Figure 58 where y, expressed in counts per channel, has been plotted against x, expressed in electrons, on a logarithmic scale. The smoothed values of y, obtained as described in the next section, have been plotted. Against each curve is written the mean value of x which is also marked by an arrow.

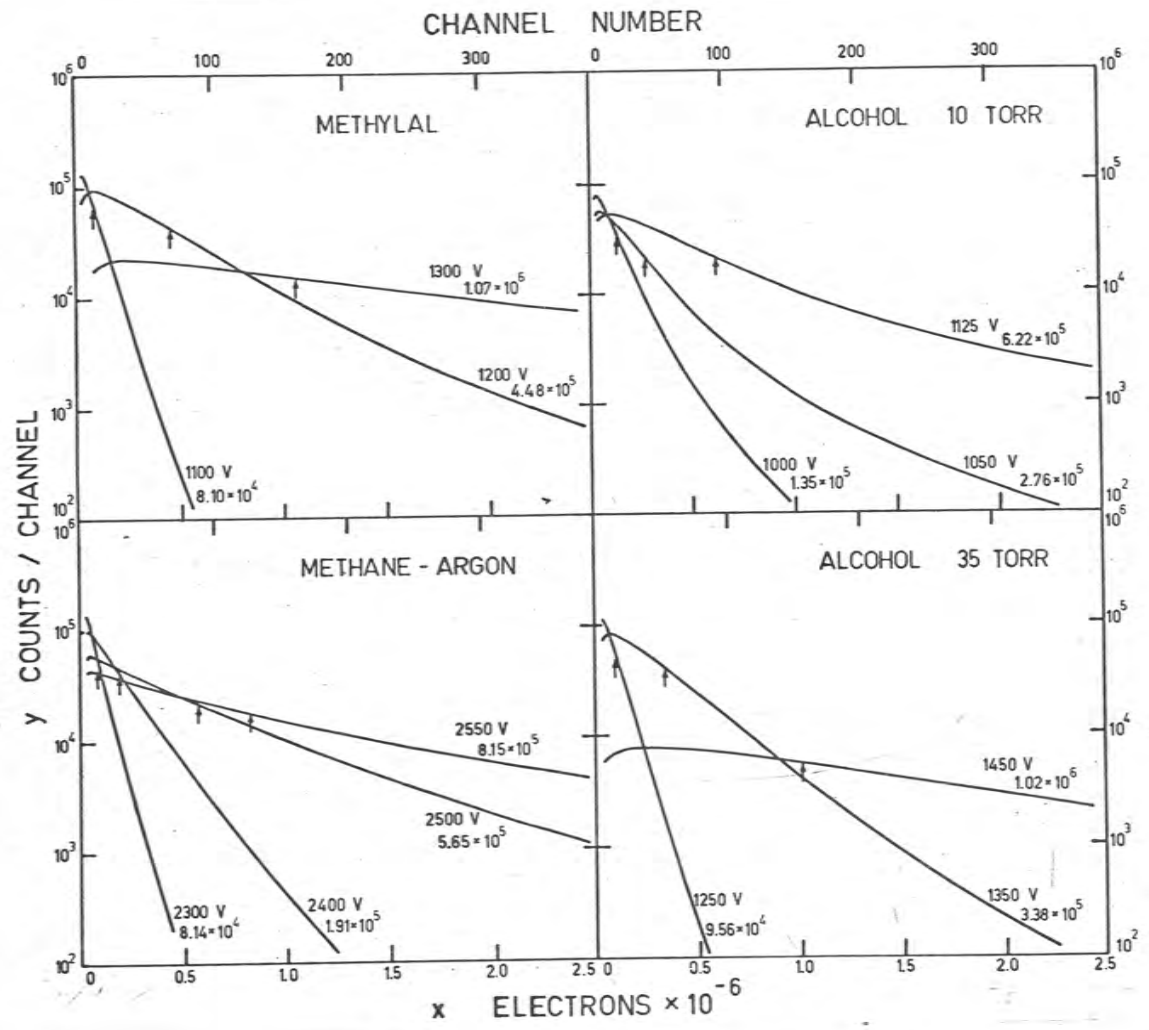

Figure 58. Experimental pulse spectra for pulses initiated by a single primary electron in a proportional counter. The frequency distribution function y expressed in counts per channel is plotted against the pulse size x expressed in electrons. The channel number is given along the top of each graph. Against each spectrum is the counter voltage and the mean value of x, which is also indicated by an arrow.

(continued next page)

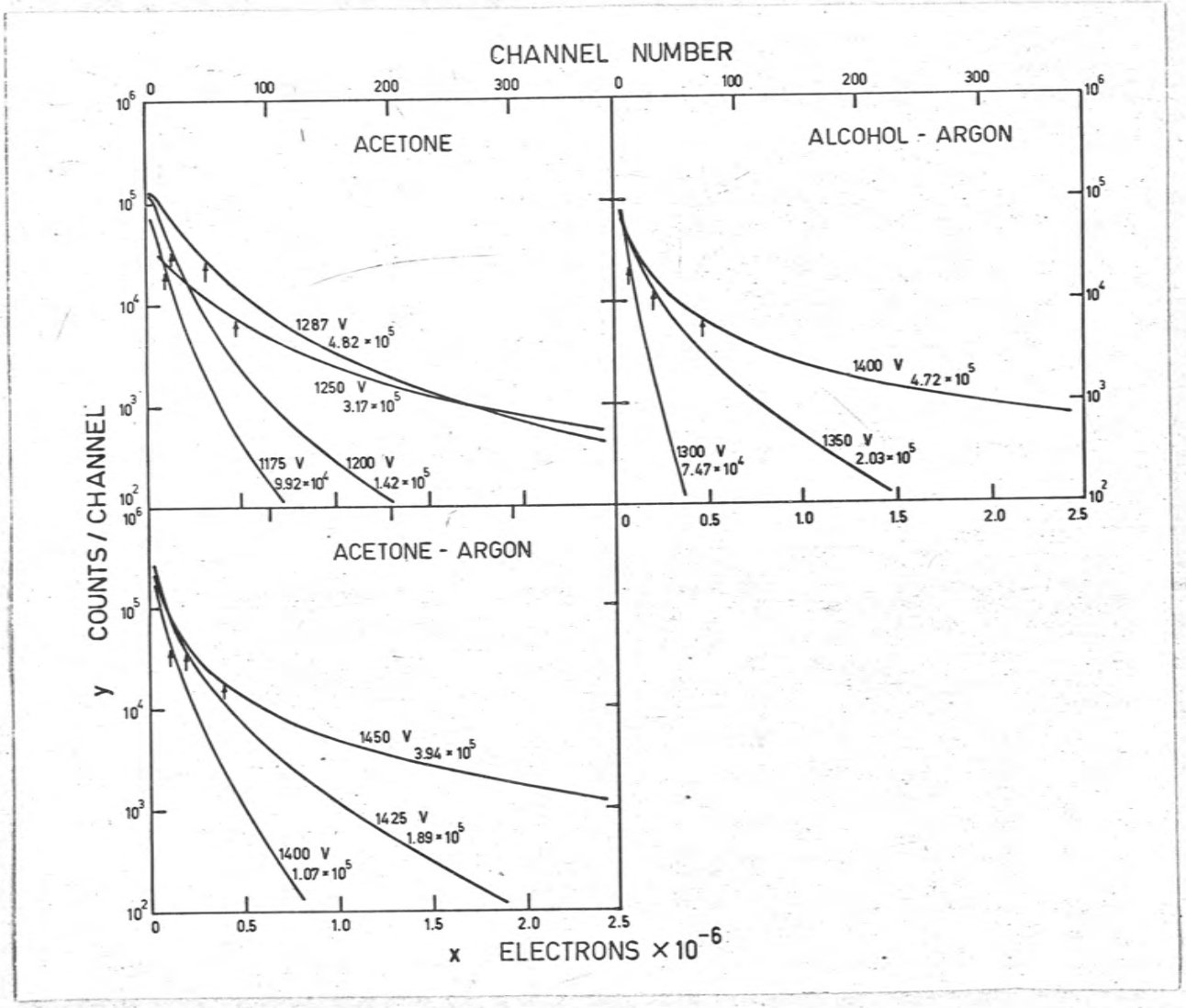

Figure 58. (continued)

6.6 Analysis of the Spectra

6.6.1 Introduction

It is difficult to compare directly the experimental distributions shown in Figure 58 with the theoretical ones shown in Figure 60 since this involves plotting the theoretical distributions for various values of the parameters and determining whether any one fits the observed distributions. A more sensitive test of the agreement between experimental and theoretical distributions is to compare their derivatives with respect to x. The distributions are always close to an exponential form so the derivative of ln y is more appropriate than the derivative of y. Thus we define the negative logarithmic derivative

$$D = -\frac{d}{dx}(\ln y) = -\frac{1}{y}\frac{dy}{dx} = -\frac{1}{\bar{x}y}\frac{dy}{dz}$$

It can be seen that D is the same for any multiple of y and is thus independent of the actual count numbers in the pulse spectrum. The logarithmic derivatives of the theoretical distributions are given in Table 14. In Figure 60 $\bar{x}D$ has been plotted against $\frac{\bar{x}}{x}$ $(= \frac{1}{z})$ for each of the theoretical distributions and for several values of the parameters*. It is more appropriate to plot D against $\frac{1}{x}$ than x since the

---

* Since the distributions of Legler (1961) were obtained by numerical integration and were available only as published curves the logarithmic derivative was found by graphical differentiation of these curves using the method given by Hartree (1958).

shape of the curve is then independent of the units used to measure x as well as y. It must be remembered however that this emphasizes the region of the distribution where x is small and compresses the region where x is large.

6.6.2 Mathematical Method.

Statistical fluctuations in the count numbers make it essential to smooth the experimental spectrum before calculating the derivative. The smoothing and differentiation were performed on a digital computer (CDC 3600, C.S.I.R.O., Canberra) using a specially written program in which the spectrum was smoothed, the logarithmic derivative formed and the mean value of x calculated.

The pulse spectra obtained from the analyser were transferred to punch cards and used as the data for the computer program. Certain parameters connected with the smoothing process were selected for each spectrum and included with the spectrum when it was analysed.

The first step in the computation was the calculation of the logarithm of the count number in each channel. Smoothing was then carried out by the method of fitting a least squares polynomial to a number n of successive points (Guest 1961). This method possesses the advantage over some others that it can be used at the ends of the range of values. A cubic polynomial was used for the first part of the spectrum where the values of x were small and the

curvature greatest. The value of n was either 7 or 13. Above a selected channel a linear polynomial was used, the value of n usually lying in the range 20 to 30.

Differentiation of the smoothed logarithms was carried out by using finite difference formulae correct to third differences. This is the equivalent to fitting a cubic through four points and taking the derivative of the cubic to be the derivative of the distribution. Newton's formula was used for the two points at the beginning of the range and Stirling's formula for the others (Whittaker and Robinson 1926). These give, correct to third differences,

$$(\delta x)\, f_0' = \frac{1}{6}\,(-11 f_0 + 18 f_1 - 9 f_2 + 2 f_3)$$

$$(\delta x)\, f_1' = \frac{1}{6}\,(-2 f_0 - 3 f_1 + 6 f_2 - f_3) \qquad \text{Newton}$$

$$(\delta x)\, f_0' = \frac{1}{12}\,(f_{-2} - 8 f_{-1} + 8 f_1 - f_2) \qquad \text{Stirling}$$

The differentiation was performed at one channel intervals for low values of x where the count numbers were high and the statistical fluctuations low, and at a large interval (selected beforehand) for large values of x where the count numbers were low.

The mean pulse height was computed by averaging over the observed spectrum. This involves some error due to the loss of the very small pulses (obscured by amplifier

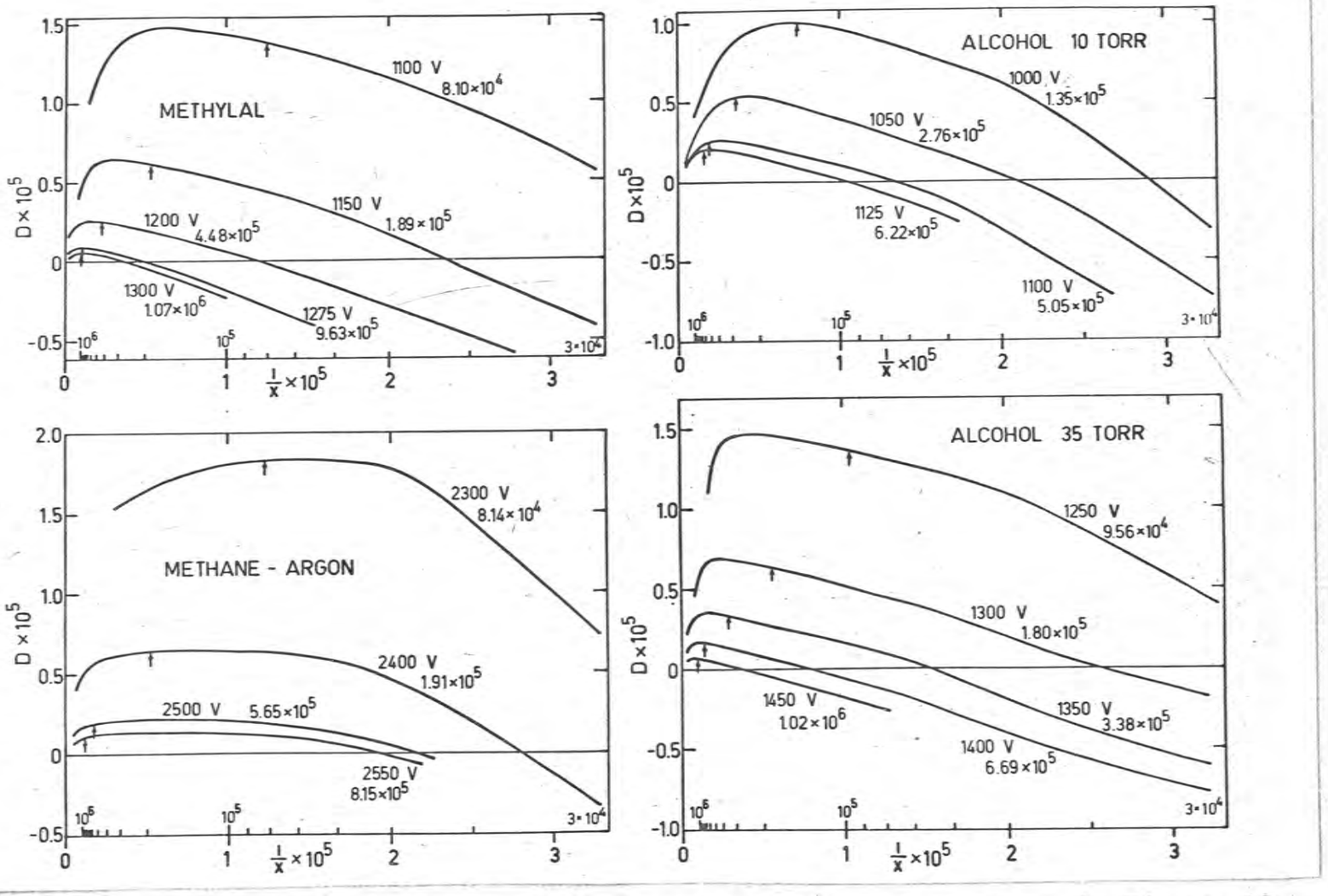

Figure 59. Logarithmic derivatives of the experimental spectra shown in Figure 58. The negative logarithmic derivative D=-1/y.dy/dx has been plotted against the reciprocal of the pulse size 1/x, where x is expressed in electrons. Above each 1/x scale there is a scale giving the corresponding number of electrons. Against each spectrum is the counter voltage and the mean value of x, which is also indicated by an arrow.

(continued next page)

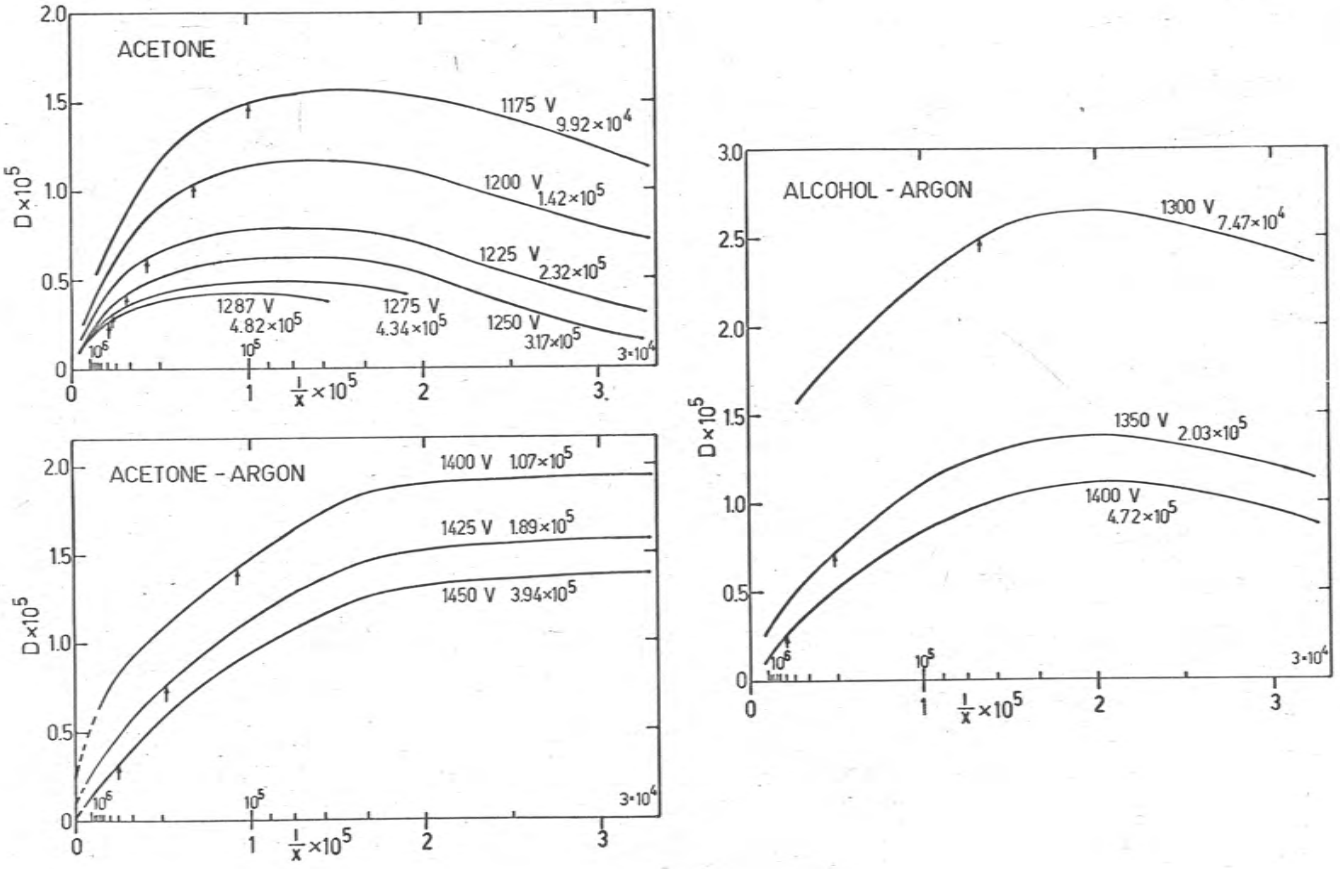

Figure 59. (continued).

noise) and the very large pulses (above the range of the analyser), but the errors will be small for most spectra and will to some extent compensate.

6.6.3 The Logarithmic Derivatives.

The results of the computation are shown in Figure 59, where D has been plotted against $\frac{1}{x}$. The pulse size x has been expressed in terms of the number of electrons in the avalanche using the conversion factor given on p.143. Thus the values of $\bar{x}$ marked on the curves represent the gas gains as defined in §3.10. The same scale has been used for D and $\frac{1}{x}$ as in the theoretical curves shown in Figure 60 so the shapes may be compared directly with those of the theoretical curves.

6.7 Discussion

The four theoretical distributions discussed in §6.3 are listed in Table 14 with the parameters upon which they depend and the conditions under which they are valid. The distributions and their logarithmic derivatives are plotted in Figure 60.

The simplest distribution is the exponential one which is to be expected when $\frac{E}{\alpha W}$ is large at the commencement of the multiplication (see p.136). As $\frac{E}{\alpha W}$ decreases the distribution will tend towards the form given by Legler (1961) which is very similar to the Pearson III distribution of Byrne (1962) (see Figure 60). The

TABLE 14. Theoretical Distributions for Pulses Initiated by a Single Electron

Distribution	Form	Parameter	Conditions	Logarithmic Derivative
Exponential	$y=e^{-z}$	-	$a=\alpha=f(r)$	$\bar{x}D=1$
High Field (Legler 1961)	not explicit (see Figure 60)	αx_0 $\quad 0<\alpha x_0<0.7$ x_0=distance an electron has to travel to gain enough energy to ionize.	$a=0 \quad 0\leq\xi<x_0$ $=$ const. $\quad x_0\leq\xi$ ξ=distance the electron has travelled since the last ionizing collision.	see Figure 60
Pearson III (Byrne 1962)	$y=z^k e^{-(k+1)z}$	$k \quad 0<k$ $1/(1+k)$=fraction of electrons which can ionize at large n.	$a=f(r)\ (1+\frac{k}{n})$	$\bar{x}D=k+1-\frac{k}{z}$
Avalanche Chain (Legler 1964)	$y=\frac{I_1(bz)}{bz}e^{-cz}$	$\mu \quad 0<\mu<1$ μ=average number of successors initiated by an avalanche. $b=\frac{2\sqrt{\mu}}{1-\mu} \qquad c=\frac{1+\mu}{1-\mu}$	Single avalanches have an exponential distribution. Small probability of one electron in an avalanche initiating a successor.	$\bar{x}D=c+\frac{2}{z}-b\frac{I_0(bz)}{I_1(bz)}$

(a)

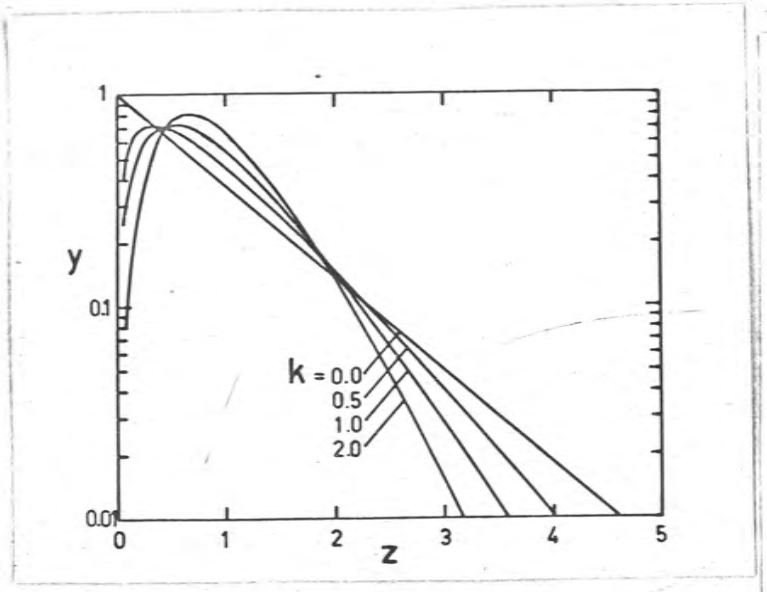

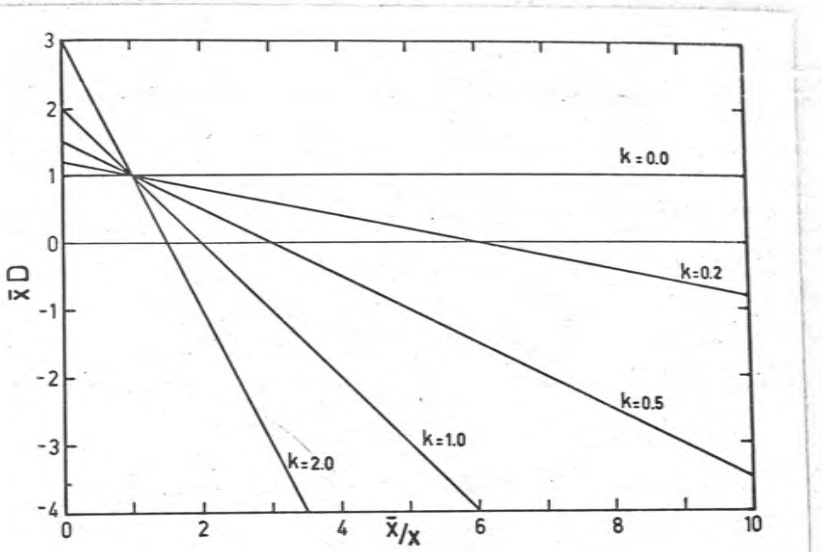

(b)

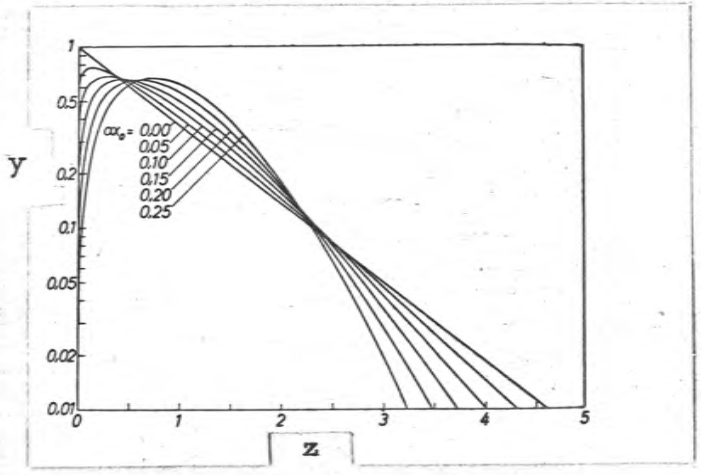

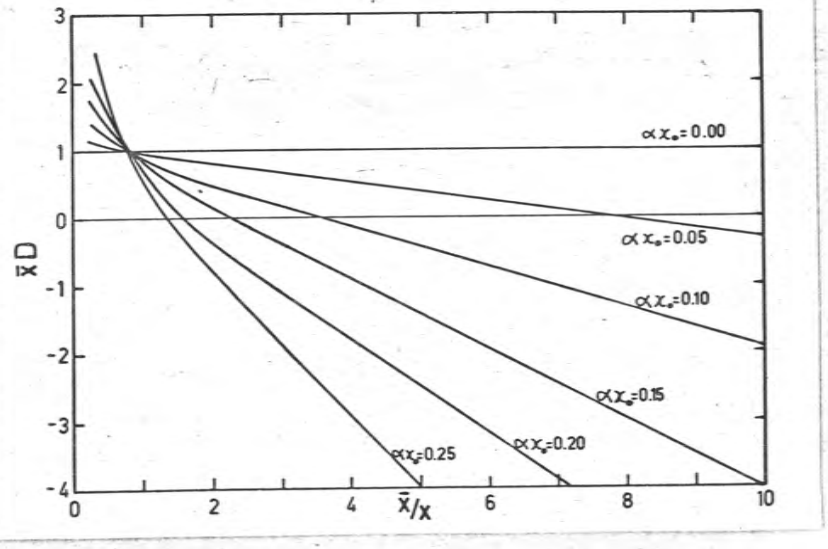

Figure 60. (a),(b). (continued next page)

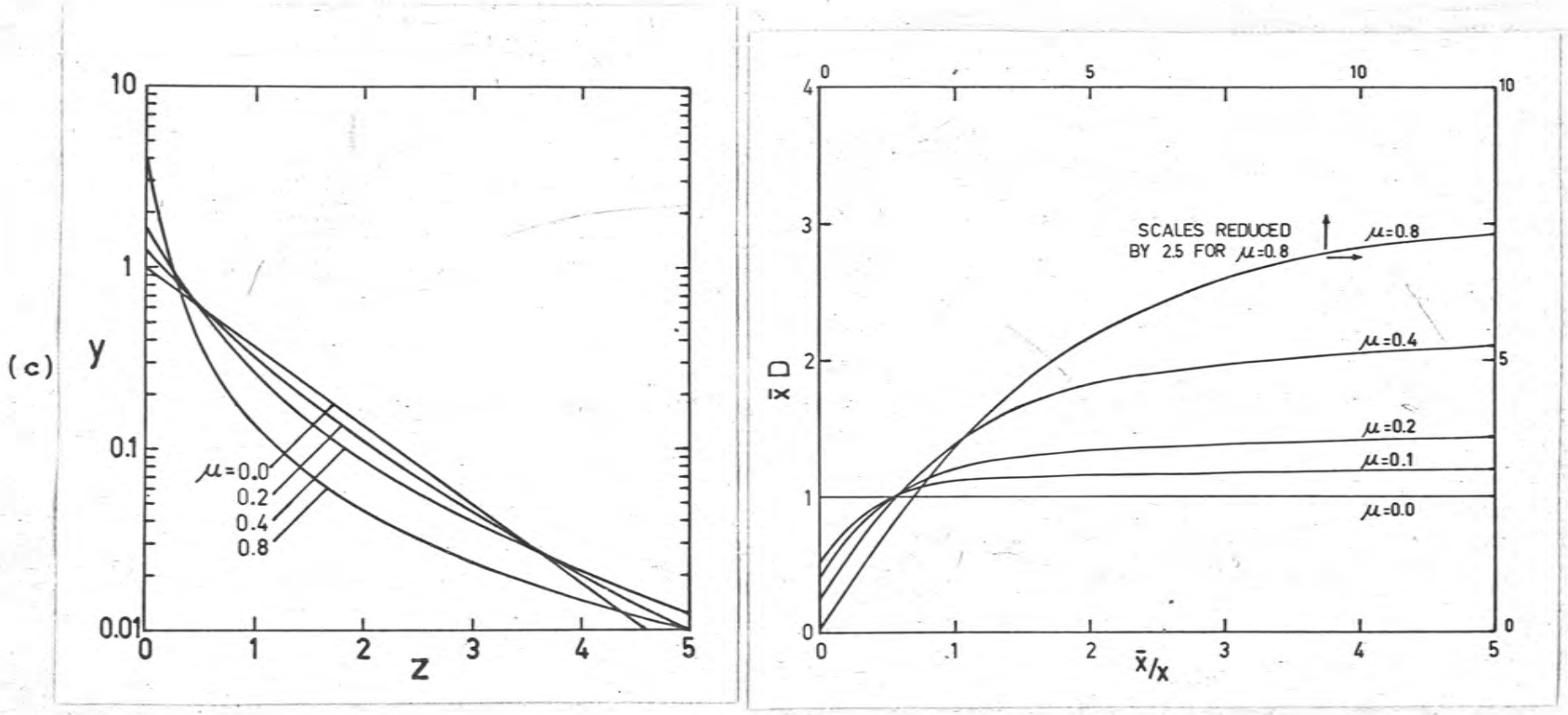

Figure 60.(c). Theoretical distributions for pulses initiated by a single electron in a proportional counter. The distributions are due to (a)Byrne (1962),(b)Legler (1961) and (c)Legler (1964) (see Table 14). In each case the frequency distribution function y has been plotted against the reduced pulse size $z=x/\bar{x}$, the distributions having been normalized so that $\int_0^\infty y\,dz=1$. To the right of the distributions are the corresponding logarithmic derivatives $D=-1/y.dy/dx$, $\bar{x}D$ having been plotted against $1/z=\bar{x}/x$.

(negative) slope of the D versus $\frac{1}{x}$ curve increases as $\frac{E}{\alpha W}$ decreases, or as E increases, since for a particular gas at a constant pressure $\frac{E}{\alpha}$ decreases as E increases provided E is not too large (Legler 1955). Legler's theory applies to a homogeneous field, however, whereas the field in the proportional counter increases as r decreases. Schlumbohm (1958) has pointed out that the field near the commencement of the multiplication is the important factor (see p.136), but he considered only the point where a pulse of the mean height commenced. Actually the point where the multiplication commences will vary considerably and large pulses, taken as a group, will commence further from the wire, i.e. in a region of lower E, than small pulses. Thus we may expect the slope of the D versus $\frac{1}{x}$ curve to decrease as x increases so that for small values of x the distribution has the form given by Legler while at higher values of x it is exponential, as seen in the curve for the methane-argon mixture (Figure 59). At large values of x the value of μ, the average number of successors initiated by an avalanche, will increase and the curve of D against $\frac{1}{x}$ will show the form given in Figure 60 (c).

The curves for methylal, methane-argon, alcohol (10 torr) and alcohol (35 torr) all display the above features except that the exponential section of the distribution

(D constant) is missing from all except the methane-argon one. The distributions for small x (before the effect of successors influences the distribution) could be represented quite well by Byrne's formula in the cases of the methylal and alcohol spectra, with a value for k of about 0.3. In fact the uniformity of the slope of the D versus $\frac{1}{x}$ curves at small values of x for these spectra is surprising. Legler's theory suggests that since with increasing V avalanches of a given size will commence nearer the wire, and thus in a region where E is higher, the slope of the D versus $\frac{1}{x}$ curve at a given value of x will increase as V increases. This theory would appear to require modification for the case of an inhomogeneous field such as occurs in the proportional counter.

The effect of successors appears on all the distributions at sufficiently large values of x, but is predominant in the acetone-argon, alcohol-argon and acetone fillings. It is interesting to note that with these three fillings the counter acted as a Geiger counter (all pulses the same size) when the voltage V was raised sufficiently. The successors in the present case do not seem to have been due to electrons liberated from the cathode as in the case of Schlumbohm's spectra since the delay for this process is about 10^{-7} to 10^{-6} sec (Wilkinson 1950) and the successors would have been observed on the oscilloscope as

they were by Schlumbohm. Successors with this delay were observed for fillings of nitric oxide and carbon dioxide-argon (§6.5) but spectra were not recorded for these fillings. However photoelectrons ejected from the filling gas by photons originating in the first avalanche could be formed quite near the wire (particularly if the filling had a high absorption coefficient for the photons) and the delay would be about 10^{-8} to 10^{-7} sec (Wilkinson 1950). This is the most probable cause of the successors in the present case since the pulses (about 1 μ sec long) appeared quite smooth on the oscilloscope.

The logarithmic derivative curves for the acetone-argon filling (Figure 59) are quite similar in shape to those for Legler's distribution (Figure 60 (c)) and the value of μ may be determined as follows. For Legler's distribution $\bar{x}\ D \to c$ as $x \to o$ (see Table 14, $I_o(x) \to 1$ and $I_1(x) \to \frac{x}{2}$ as $x \to o$) so the value of c may be found from the experimental curves by multiplying the value of D at small values of x by $\bar{x}$. From $c(= \frac{1+\mu}{1-\mu})$ the value of μ can be calculated. The values of μ were 0.35 at 1400V, 0.50 at 1425V and 0.69 at 1450V. These values increase as V increases, as expected since μ is the average number of successors initiated by a single avalanche and the size of the avalanches increases as V increases. However the value of y, the average number of successors initiated by

a single electron in an avalanche, should be almost constant. The value of y may be obtained by noting that $\mu = \gamma\bar{\nu}$ and $\bar{\nu} = \bar{x}(1-\mu)$ where $\bar{\nu}$ is the average number of electrons in a single avalanche* (Legler 1964), so that $\gamma = \frac{\mu}{(1-\mu)\bar{x}}$. The values of y obtained in this way were 5.0×10^{-6}, 5.3×10^{-6} and 5.6×10^{-6} at 1400V, 1425V and 1450V respectively. The small change in y is in good agreement with Legler's theory. As $x \to \infty$, $\bar{x}D \to c-b$ ($\frac{I_0(x)}{I_1(x)} \to 1$ as $x \to \infty$) and so since c can be calculated from μ the value of D at very large x can be calculated. In Figure 59 the curves for the acetone-argon filling have been extended by dashed lines to the calculated values of $\frac{c-b}{\bar{x}}$ and it can be seen that the theoretically predicted value of D at large x is close to that which would be deduced from the experimental curves.

6.8 Conclusion

The present results are not directly comparable with those of Curran et al. (1949) or Schlumbohm (1958) because of the different fillings used, except in the case of the spectra obtained with a methylal filling by Schlumbohm. In this case there is close agreement, both results indicating that the spectra are quite well described by the theory of Legler (1961). The effect of successors on the distribution was not observed by Schlumbohm but this was

---

*Not a single observed avalanche chain.

possibly due to the fact that his measurements did not cover as wide a range of values of y as the present ones.

The presence of successors tends to increase the relative variance of the distribution (relative variance = variance/(mean)^2). The relative variance is 1 for the exponential distribution, $\frac{1}{k+1}$ for the Pearson III distribution and $\frac{1+\mu}{1-\mu}$ for Legler's (1964) distribution. When the counter is to be used for counting ultra-violet photons or as a proportional counter for soft x-rays the relative variance should be as small as possible. From the present results it is concluded that the relative variance is approximately 1 for the alcohol, methylal and methane-argon fillings, while for the acetone, acetone-argon and alcohol-argon fillings it is greater than 1, becoming as large as 5.5 for the acetone-argon filling at 1450V. The addition of argon to the filling appears to increase the relative variance, at least for the conditions under which the present results were obtained (thin wire and relatively low filling pressures).

Chapter 7. Absorption Coefficients of some Filling Gases

7.1 Introduction

In order to make the efficiency of an ion chamber as high as possible a large fraction of the radiation which passes through the window must be absorbed in the filling gas. The fraction of the radiation absorbed in the gas is given by

$$1 - \exp(-\frac{p}{760} l\, a)$$

where p is the pressure in torr, l the path length through the gas in cm and a is the absorption coefficient of the gas at S.T.P. in cm^{-1}; so this quantity must be as large as possible. Except in the case of nitric oxide (see §2.1) absorption coefficients had not previously been measured in the vacuum ultra-violet region for the filling gases used in the present work. Therefore it was decided to measure the absorption coefficients of these gases over the wavelength region extending from the photoionization threshold to the transmission limit of the window of the ion chamber in which they were used. The gases investigated were acetone, carbon disulphide, benzene, toluene, xylene, ethyl chloride, ethyl bromide and ethyl iodide.

7.2 Method

An absorption cell with a path length of 1.3 mm was used. The end of the cell through which the beam entered was formed by a lithium fluoride window identical to the

ones used on the ion chambers. The other end was formed by a glass plate coated with a layer of sodium salicylate so that radiation passing through the cell struck the salicylate and caused to to fluoresce. The length of the cell, which was adjustable, was fixed by a circular spacer between the lithium fluoride window and the glass plate. The beam from the monochromator passed through a grid coated with salicylate before entering the cell, the fluorescent radiation being detected by a photomultiplier as described in §3.6.2. A second photomultiplier behind the glass plate measured the intensity of the fluorescent radiation from the salicylate on the plate. The ratio of the signals from the photomultipliers was formed using the same system as was used when recording the spectral responses of the ion chambers (§3.6.2), and recorded on paper chart. The cell was evacuated using a portable vacuum system and the liquids admitted from the same phial as was used when filling the ion chambers. Pressures were measured with an oil monometer.

To measure the absorption coefficient the cell was first evacuated and the ratio of the photomultiplier signals recorded as the wavelength was scanned over the region of interest. The source was the hydrogen spectrum (see Figure 17(a)) and the spectral bandwidth 2Å. Gas was then admitted into the cell at a pressure sufficient to reduce

the intensity of the transmitted beam to about one half of its original intensity. The pressures were in the range 1 to 20 torr. The ratio of the two photomultiplier signals was then recorded again, the chart having been rewound so that the wavelength scales for the two traces were the same. The ratio of the two ratios was then equal to the attenuation of the beam in passing through the gas, which was $\exp(-\frac{p}{760} l a)$, where the symbols have the meanings given above. This expression was used to calculate the value of a. The advantages of recording the ratio of the two photomultiplier signals rather than just that due to the transmitted beam are, firstly, that errors due to changes in the intensity of the lamp while the cell is being filled are eliminated, and secondly that the form of the absorption spectrum is more easily recognized since the positions of maxima and minima in the absorption coefficient are immediately obvious from the second trace whereas they would not be so if superimposed on the hydrogen spectrum.

7.3 Results

No attempt was made to search for fine structure in the absorption spectra since it was the magnitude of the absorption which was required. Most of the spectra showed almost no structure and the value of a was calculated at 5Å intervals to give the spectra shown in Figure 61. For

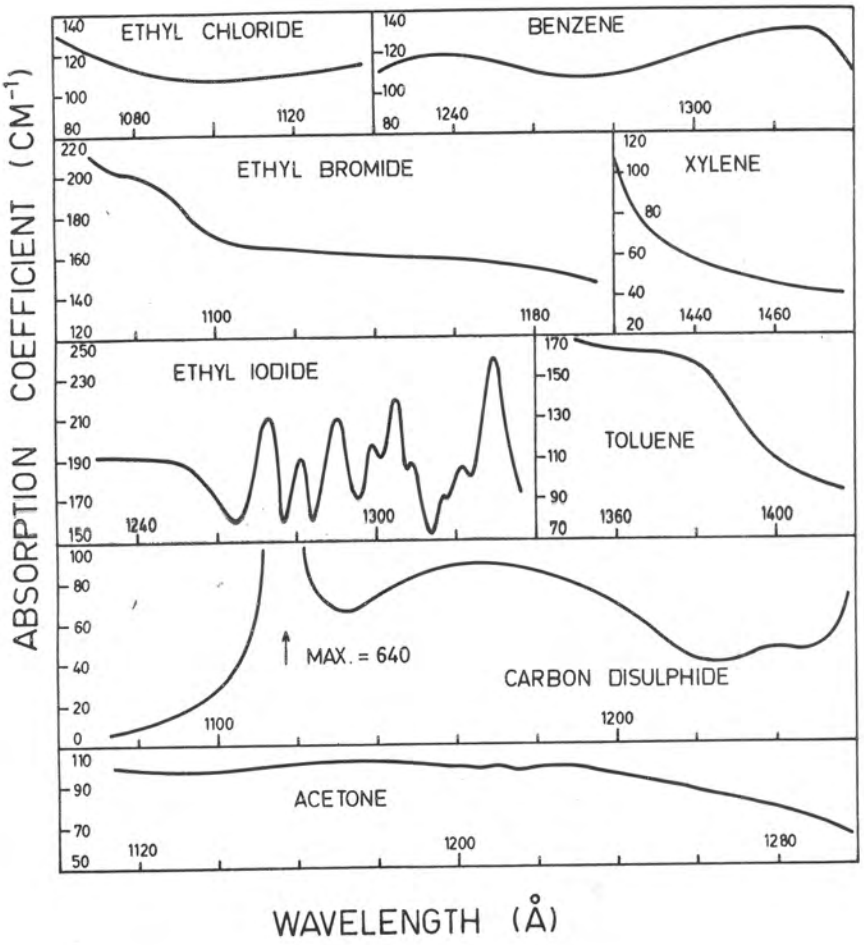

Figure 61. Absorption coefficients of various filling gases. All wavelength scales are marked in 20 Å divisions. The zero has been suppressed on most of the absorption coefficient scales.

ethyl iodide and carbon disulphide a was calculated at the positions where it was a maximum or minimum.

7.4 Discussion

The main feature of interest in the spectra is the extremely strong absorption band of carbon disulphide at 1117Å. This band was observed photographically by Tanaka et al. (1960) as the most prominent member of a Rydberg series converging on the second ionization threshold at 857Å. From the quantum efficiency curve for a carbon disulphide filled chamber shown in Figure 25 it appears that the photoionization efficiency drops to about 50% at this band, suggesting that it is approximately 50% preionized.

The absorption coefficients are all greater than about 50 cm^{-1} so that a high proportion of the radiation entering the ion chambers will be absorbed in the filling gas even at the lowest filling pressures used (about 3 mm, for xylene) and when the radiation strikes the window at a large angle of incidence so that the path length through the gas is only about 1 cm.

Chapter 8. Conclusion

The work described in this thesis has been directed towards carrying out determinations of molecular oxygen densities in the upper atmosphere by the measurement of the absorption of solar ultra-violet radiation. Investigations have also been made with the aim of improving the techniques used in these measurements.

It is apparent from the discussion of the various techniques in §2.5 that the use of ion chambers to measure the absorption of ultra-violet radiation provides the simplest and most accurate method of determining molecular oxygen densities in the range 70 to 170 km. The ion chambers constructed for use in the present work have proved well suited to use in rockets such as the HAD where the experimental conditions (e.g. acceleration, vibration and aerodynamic heating) are severe. The effects on the chambers of changes in temperature have been measured. There is some change in the limits of the spectral response, particularly the lower one, and a large change in the gas gain characteristic of chambers filled to a pressure near the saturated vapour pressure of the filling gas. It has been shown that with the exception of chambers having a filling of carbon disulphide all the

chambers investigated in the present work are unaffected by exposure to ultra-violet radiation of solar intensity for the period of a rocket flight.

The present results appear to be the most accurate low latitude oxygen densities which have been obtained, and in fact they are the only such measurements which have been reported for the Southern Hemisphere. It would be desirable not only to carry out the measurements using Lyman-α detectors at various seasons of the year so as to determine the extent of seasonal variations, but also to extend the measurements to higher altitudes using the sapphire-xylene and quartz-triethyl amine chambers carried in a rocket which reached an altitude of about 150 km (see pp. 89,90). In this way the oxygen density could be determined over the dissociation region (100 to 130 km) where, as illustrated in Figure 13, there is still disagreement by as much as an order of magnitude between different experimental results.

A Long Tom* rocket was instrumented to carry out these measurements and fired, but owing to a fault in the telemetry sender the signals from the rocket were lost so that no ultra-violet measurements were obtained. A photograph of the head for the Long Tom is shown in Figure 62. Nine

---

*The Long Tom is a two-stage solid fuel rocket developed by the Flight Projects Group, Weapons Research Establishment. It is 9 in. in diam and reaches an altitude of 150 km.

Figure 62. Photograph of the head for the Long Tom rocket.

of the ion chambers listed in Table 6 including the lithium fluoride-nitric oxide, sapphire-xylene and quartz-triethyl amine ones were mounted in the rocket. With these detectors it would be possible not only to determine oxygen densities in the range 70 to 150 km but also to measure the absolute solar fluxes in a number of wavelength bands between 1000 and 1700Å. Some of the ion chambers can be seen at the base of the head in Figure 62. The casing has been removed from the section above the detector ring to expose the ion chamber amplifiers and calibration circuits. Above the aerial compartment is the telemetry section.

The investigation of single-electron pulse spectra in a proportional counter has indicated that for the filling gases and pressures used, the relative variance of the distribution was not less than 0.77 and in some cases was considerably more owing to the effects of secondary avalanches which appeared to some extent on all the spectra. These values are somewhat greater than the value of 0.67 which has previously been suggested (Curran et al. 1949).

APPENDIX

Publications.

The following papers have been written on the work described in this thesis.

J.H. Carver, P. Mitchell, E.L. Murray and B.G. Hunt, 1964, "Molecular Oxygen Density and Lyman-α Absorption in the Upper Atmosphere", J. Geophys. Res., 69, 3755.

J.H. Carver and P. Mitchell, 1964, "Ionization Chambers for the Vacuum Ultra-Violet", J. Scient. Instrum., 41, 555.

J.H. Carver, P. Mitchell, E.L. Murray and B. Rofe, "Molecular Oxygen Density and Ultra-Violet Absorption in the Southern Hemisphere", to be published 1966, Space Research 6.

REFERENCES

Aboud, A., Behring, W.E., and Rense, W.A., 1959, Astrophys. J., 130, 381.

Allen, C.W., 1963, Astrophysical Quantities (London: Athlone Press) p.172.

Allen, C.W., 1965, Space Sci. Rev., 4, 91.

Allison, R., Burns, J., and Tuzzolino, A.J., 1964a, J. Opt. Soc. Am., 54, 747.

Allison, R., Burns, J., and Tuzzolino, A.J., 1964b, J. Opt. Soc. Am., 54, 1381.

Barth, C.A., 1961, Chemical Reactions in the Lower and Upper Atmosphere (New York: Interscience) p.303.

Barth, C.A., 1965, Space Research 5.

Bates, D.R., and Nicolet, M., 1950, J. Geophys. Res., 55, 301.

Bates, D.R., and Witherspoon, A.E., 1952, Mon. Not. R. Astr. Soc., 112, 101.

Baum, W.A., Johnson, F.S., Oberly, J.J., Rockwood, C.C., Strain, C.V., and Tousey, R., 1946, Phys. Rev. 70, 781.

Black, W.S., Booker, D., Burton, W.M., Jones, B.B., Shenton, D.B., and Wilson, R., 1965, Nature, Lond., 206, 654.

Blake, A.J., Carver, J.H., and Haddad, G.N., to be published 1966, J. Quant. Spectrosc. Radiat. Transfer.

Burton, W.M., and Wilson, R., 1965, Nature, Lond., 207, 61.

Byram, E.T., Chubb, T., Friedmam, H., and Gailar, N., 1953, Phys. Rev., 91, 1278

Byram, E.T., Chubb, T.A., and Friedman, H., 1955, Phys. Rev., 98, 1594.

Byram, E.T., Chubb, T.A., Friedman, H., and Kupperian, J.E., 1956, Astrophys. J., 124, 480.

Byram, E.T., Chubb, T.A., Friedman, H., Kupperian, J.E., and Kreplin, R.W., 1958, Astrophys. J., 128, 738.

Byrne, J., 1962, Proc. R. Soc. Edinb., A, 66, 33.

Chapman, S., and Kendall, P.C., 1965, Q. Jl. R. Met. Soc., 91, 115.

Chubb, T.A. and Friedman, H., 1955, Rev. Scient. Instrum., 26, 493.

Chubb, T.A., Friedman, H., Kreplin, R.W., and Kupperian, J.E., 1957, J. Geophys. Res., 62, 389.

Chubb, T.A., Byram, E.T., Friedman, H., and Kupperian, J.E., 1958, Annls. Geophys., 14, 109.

Cook, G.R., and Ching, B.K., 1965, Absorption, photoionization and fluorescence of some gases of importance in the study of the upper atmosphere. Rep. No. TDR-469(9260-01)-4 (Aerospace Corporation).

Curran, S.C., and Wilson, H.W., 1965, Alpha-,Beta- and Gamma-Ray Spectroscopy, Ed. K. Siegbahn (Amsterdam: North Holland) p.303.

Curran, S.C., Cockcroft, A.L., and Angus, J., 1949, Phil. Mag., 40, 929.

Danjon, A., 1954, The Earth as a Planet, Ed. G. P. Kuiper (University of Chicago Press) p.726.

de Jager, C., 1964, Research in Geophysics, Ed. H. Odishaw (Massachusetts: MIT Press) vol.1, p.1.

de Valence, L.P., 1955, Br. J. Appl. Phys., 6, 311.

Detwiler, C.R., Purcell, J.D., and Tousey, R., 1961a, Mem. Soc. R. Sci. Liege, ser. 5, 4, 253.

Detwiler, C.R., Garrett, D.L., Purcell, J.D., and Tousey, R., 1961b, Annls. Geophys., 17, 9.

Ditchburn, R.W., 1962, J. Quant. Spectrosc. Radiat. Transfer, 2, 361.

Ditchburn, R.W., Bradley, J.E.S., Cannon, C.G., and Munday, G., 1954, Rocket Exploration of the Upper Atmosphere, Ed. R.L.F. Boyd and M.J. Seaton (London: Pergamon Press) p.327.

Dunkelman, L., Fowler, W.B., and Hennes, J.P., 1962, Appl. Opt., 1, 695.

Dunkelman, L., Hennes, J.P., and Fowler, W.B., 1963, Space Research 3, 1174.

Franzen, W., and Cochran, L.W., 1962, Nuclear Instruments and their Uses, Ed. A. H. Snell (New York: Wiley) vol.1, p.67.

Friedman, H., 1960, Physics of the Upper Atmosphere, Ed. J.A. Ratcliffe (New York: Academic Press) p.133.

Friedman, H., Lichtman, S.W., and Byram, E.T., 1951, Phys. Rev., 83, 1025.

Friedman, H., Chubb, T.A., Kupperian, J.E., and Lindsay, J.C., 1958, Annals. of the I.G.Y., vol.6, p.316.

Friedman, H., Chubb, T.A., and Siomkajlo, J.M., 1964, Sounding Rocket Research Techniques, Instruction Manual No.9, I.Q.S.Y. Secretariat, London.

Frisch, O.R., 1959, Fluctuations in Chain Processes, AECL Rep. No.748, Chalk River.

Gillespie, A.B., 1953, Signal, Noise and Resolution in Nuclear Counter Amplifiers (London: Pergamon Press) p.82.

Gross, M.J., and Heddle, D.W.O., 1964, Proc. R. Soc., A, 279, 523.

Guest, P.G., 1961, Numerical Methods of Curve Fitting (Cambridge University Press) p.349.

Hall, L.A., Damon, K.A., and Hinteregger, H.E., 1963a, Space Research 3, 745.

Hall, L.A., Schweizer, W., and Hinteregger, H.E., 1963b, J. Geophys. Res., 68, 6413.

Hall, L.A., Schweizer, W., and Hinteregger, H.E., 1965, J. Geophys. Res., 70, 105.

Hammann, J.F., 1958, Z. Angew. Phys., 10, 187.

Hartree, D.R., 1958, Numerical Analysis (Oxford: Clarendon Press) p.129.

Hemenway, C.L., Soberman, R.K., and Witt, G., 1964, Tellus, 16, 84.

Hesstvedt, E., 1962, Tellus, 14, 290.

Hintereggor, H.E., 1961a, Space Astrophysics, Ed. W. Liller (New York: McGraw-Hill) p.34.

Hintereggor, H.E., 1961b, Mem. Soc. R. Sci. Liege, ser.5, 4, 111.

Hintereggor, H.E., 1961c, J. Geophys. Res., 66, 2367.

Hintereggor, H.E., 1962, J. Atmos. Sci., 19, 351.

Hintereggor, H.E., and Watanabe, K., J. Opt. Soc. Am., 1953, 43, 604.

Hintereggor, H.E., and Watanabe, K., 1962, J. Geophys. Res., 67, 3373.

Hintereggor, H.E., Hall, L.A., and Schmidtke, G., 1965, Space Research 5, 1175.

Hopfield, J.J., and Clearman, H.E., 1948, Phys. Rev., 73, 877.

Hughes, E.E., 1961, J. Chem. Phys., 35, 1531.

Hunt, B.G., to be published 1965, J. Atmos. Sci.

Johnson, F.S., Purcell, J.D., Watanabe, K., and Tousey, R., 1952, J. Geophys. Res., 57, 157.

Johnson, F.S., Purcell, J.D., and Tousey, R., 1954, Phys. Rev., 95, 621.

Johnson, F.S., Malitson, H.H., Purcell, J.D., and Tousey, R., 1958, Astrophys. J., 127, 80.

Jursa, A.S., Tanaka, Y., and LeBlanc, F., 1959, Planet. Space Sci., 1, 161.

Jursa, A.S., Nakamura, M., and Tanaka, Y., 1963, J. Geophys. Res., 68, 6145.

Jursa, A.S., Nakamura, M., and Tanaka, Y., 1965, J. Geophys. Res., 70, 2699.

Inn, E.C.Y., Watanabe, K., and Zelikoff, M., 1953, J. Chem. Phys., 21, 1648.

Kallmann-Bijl, H.K., and Sibley, W.L., 1963, Planet. Space Sci., 11, 1379.

Kantor, A.J., and Cole, E.C., 1965, J. Appl. Met., 4, 228.

Knapp, R.A., and Smith, A.M., 1964, Appl. Opt., 3, 637.

Knudson, A.R., and Kupperian, J.E., 1957, J. Opt. Soc. Am., 47, 440.

Kreplin, R.W., Chubb, T.A., and Friedman, H., 1962, J. Geophys. Res., 67, 2231.

Kupperian, J.E., and Kreplin, R.W., 1957, Rev. Scient. Instrum., 28, 14.

Kupperian, J.E., Byram, E.T., and Friedman, H., 1959, J. Atmos. Terr. Phys., 16, 174.

Laufer, A.H., Pirog, J.A., and McNesby, J.R. 1965, J. Opt. Soc. Am., 55, 64.

Lee, P., 1955, J. Opt. Soc. Am., 45, 703.

Legler, W., 1955, Z. Phys., 140, 221.

Legler, W., 1961, Z. Naturf., A, 16, 253.

Legler, W., 1964, Z. Naturf., A, 19, 481.

L'vova, A.A., Mikirov, A.Ye., and Poloskov, S.M., 1964, Geomagnetism and Aeronomy, 4, 839.

McKinnon, P.J., and Smith, L.G., 1964, Geophysics Corporation of America, Tech. Rep. 64-12-N.

Marmo, F.F., 1953, J. Opt. Soc. Am., 43, 1186.

Metzger, P.H., and Cook, G.R., 1964, J. Quant. Spectrosc. Radiat. Transfer, 4, 107.

Metzger, P.H., and Cook, G.R., 1965, J. Opt. Soc. Am., 55, 516.

Newell, R.E., 1963, Q. Jl. R. Met. Soc., 89, 167.

Nicolet, M., 1960, Physics of the Upper Atmosphere, Ed. J.A. Ratcliffe (New York: Academic Press) p.17.

Nier, A.O., Hoffman, J.H., Johnson, C.Y., and Holmes, J.C., 1964, J. Geophys. Res., 69, 979.

Nygaard, K.J., 1964, Br. J. Appl. Phys., 15, 597.

Packer, D.M., and Lock, C., 1951, J. Opt. Soc. Am., 41, 699.

Pagel, B.E.J., 1963, Planet. Space Sci., 11, 333.

Pearson, P.H.O., to be published 1966, J. Atmos. Terr. Phys.

Pottasch, S.R., 1964, Space Sci. Rev., 3, 816.

Preston, W.M., 1940, Phys. Rev., 57, 887.

Purcell, J.D., and Tousey, R., 1960, J. Geophys. Res., 65, 370.

Purcell, J.D., Packer, D.M., and Tousey, R., 1960, Space Research 1, 581.

Rawcliffe, R.D., Meloy, G.E., Friedman, R.M., and Rogers, E.H., 1963, J. Geophys. Res., 68, 6425.

Rense, W.A., 1953, Phys. Rev., 91, 299.

Rense, W.A., 1961, Space Astrophysics, Ed. W. Liller (New York: McGraw-Hill) p.17.

Sampson, J.A.R., 1964, J. Opt. Soc. Am., 54, 6.

Schlumbohm, H., 1958, Z. Phys., 152, 49.

Smith, L.G., and Weeks, L., 1965, Geophysics Corporation of America, Tech. Rep. 65-10-N.

Smith, L.G., Accardo, C.A., Weeks, L.H., and McKinnon, P.J., 1965, J. Atmos. Terr. Phys., 27, 803.

Smyth, H.D., and Blewett, J.P., 1934, Phys. Rev., 46, 276.

Stober, A.K., Scolnik, R., and Hennes, J.P., 1963, Appl. Opt., 2, 735.

Tanaka, Y., 1955, J. Opt. Soc. Am., 45, 663.

Tanaka, Y., Inn, E.C.Y., and Watanabe, K., 1953, J. Chem. Phys., 21, 1651.

Tanaka, Y., Jursa, A.S., and LeBlanc, F., 1960, J. Chem. Phys., 32, 1205.

Taylor, R.G., Chubb, T.A., and Kreplin, R.W., 1965, J. Opt. Soc. Am., 55, 1078.

Tousey, R., 1963, Space Sci. Rev., 2, 3.

Tousey, R., Watanabe, K., and Purcell, J.D., 1951, Phys. Rev., 83, 792.

Tousey, R., Purcell, J.D., Austin, W.E., Garrett, D.L., and Widing, K.G., 1964, Space Research 4, p.703.

U.S. Standard Atmosphere, 1962 (Washington, D.C.: U.S. Govt. Printing Office).

Violett, T., and Rense, W.A., 1959, Astrophys. J., 130, 954.

Watanabe, K., 1954, J. Chem. Phys., 22, 1564.

Watanabe, K., and Inn, E.C.Y., 1953, J. Opt. Soc. Am., 43, 32.

Watanabe, K., and Matsunaga, F.M., 1961, Hawaii Inst. Geophys., Contrib. 27, Honolulu.

Watanabe, K., and Zelikoff, M., 1953, J. Opt. Soc. Am., 43, 753.

Watanabe, K., Inn, E.C.Y., and Zelikoff, M., 1953a, J. Chem. Phys., 21, 1026.

Watanabe, K., Marmo, F.F., and Inn, E.C.Y., 1953b, Phys. Rev., 90, 155.

Watanabe, K., Nakayama, T., and Mottl, J., 1962, J. Quant. Spectrosc. Radiat. Transfer, 2, 369.

Weissler, G.L., Lee, P., and Mohr, E.J., 1952, J. Opt. Soc. Am., 42, 84.

West, D., 1953, Prog. Nucl. Phys., 3, 18.

Whittaker, E.T., and Robinson, G., 1926, The Calculus of Observations (London: Blackie) p.62.

Wijsman, R.A., 1949, Phys. Rev., 75, 833.

Wilkinson, D.H., 1950, Ionization Chambers and Counters (Cambridge University Press) p.149.

Willmore, P., 1961, Mem. Soc. R. Sci. Liege, ser.5, 4, 103.